



Høgskulen på Vestlandet

ING5002 - Master Thesis

ING5002-MOPPG-2023-HØST-FLOWassign

Predefinert informasjon

Startdato:	01-12-2023 12:00 CET	Termin:	2023 HØST
Sluttdato:	20-12-2023 14:00 CET	Vurderingsform:	Norsk 6-trinns skala (A-F)
Eksamensform:	Masteroppgave		
Flowkode:	203 ING5002 1 MOPPG 2023 HØST		
Intern sensor:	(Anonymisert)		

Deltaker

Kandidatnr.:	101
---------------------	-----

Informasjon fra deltaker

Antall ord *:	40172
----------------------	-------

Egenerklæring *: Ja

Jeg bekrefter at jeg har Ja registrert oppgavetittelen på norsk og engelsk i StudentWeb og vet at denne vil stå på vitnemålet mitt *:

Jeg godkjenner avtalen om publisering av masteroppgaven min *

Ja

Er masteroppgaven skrevet som del av et større forskningsprosjekt ved HVL? *

Nei

Er masteroppgaven skrevet ved bedrift/uirksomhet i næringsliv eller offentlig sektor? *

Nei



MASTEROPPGAVE

Eksperimentell studie og Computational Fluid Dynamics (CFD) simulering av hvordan utenpåmonterte fotovoltaiske installasjoner påvirker brannodynamikken på en realistisk norsk 30° skrå takkonstruksjon

Experimental Study and Computational Fluid Dynamics (CFD) Modelling of how Building-Applied Photovoltaic (BAPV) Installations Affect the Fire Dynamics on a Realistic Norwegian 30° Sloping Roof Construction

Joacim Skogseide

Master i Brannsikkerhet

Fakultet for ingeniør- og naturvitenskap, institutt for sikkerhet, kjemi- og bioingeniørfag

Veiledere: Jan Torgil Josefsen, Høgskulen på Vestlandet

Sanjay Kumar Khattri, Høgskulen på Vestlandet

Reidar Stølen, RISE Fire Research AS

18. desember 2023

Jeg bekrefter at arbeidet er selvstendig utarbeidet, og at referanser/kildehenvisninger til alle kilder som er brukt i arbeidet er oppgitt, jf. Forskrift om studium og eksamen ved Høgskulen på Vestlandet, § 12-1.

**Experimental Study and Computational Fluid Dynamics (CFD)
Modelling of how Building-Applied Photovoltaic (BAPV) Installations
Affect the Fire Dynamics on a Realistic Norwegian 30° Sloping Roof
Construction**



Joacim Skogseide

WESTERN NORWAY UNIVERSITY OF APPLIED SCIENCES

Master Thesis in Fire Safety Engineering

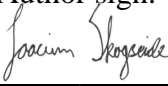
Haugesund
December 2023



Western Norway
University of
Applied Sciences

Experimental Study and Computational Fluid Dynamics (CFD)
Modelling of How Building-Applied Photovoltaic (BAPV)
Installations Affect the Fire Dynamics on a Realistic
Norwegian 30° Sloping Roof Construction

Master thesis in Fire Safety Engineering

Author: Joacim Skogseide	Author sign. 
Thesis submitted: Autumn 2023	Open thesis
Tutor: Jan Torgil Josefsen, Western Norway University of Applied Sciences Sanjay Kumar Khattri, Western Norway University of Applied Sciences External tutor: Reidar Stølen, RISE Fire Research AS	
Keywords: BAPV, PV modules, photovoltaic, roof construction, roofing membrane, bitumen, experimental research, flame spread, fire propagation, fire dynamics, cone calorimeter, TGA, CFD, FDS, pyrolysis model, numerical modelling, fire simulation	Number of pages: 102 + Appendix: 42 Haugesund 18.12.2023
This thesis is a part of the master's program in Fire Safety engineering at Western Norway University of Applied Sciences. The author(s) is responsible for the methods used, the results that are presented, the conclusion and the assessments done in the thesis.	

Preface

This Master thesis was prepared in the Department of Safety, Chemical and Bioengineering at the Western Norway University of Applied Sciences, Haugesund in fulfilment of the requirements for acquiring a M.Sc. degree. The thesis was supervised by:

Jan Torgil Josefsen, Assistant Professor at the Department of Safety, Chemical and Bioengineering.

Sanjay Kumar Khattri, Professor at the Department of Safety, Chemical and Bioengineering.

Reidar Stølen, Scientist at RISE Fire Research AS, Trondheim, Norway.

Acknowledgements

I would like to thank my three supervisors for their valuable insights, academic discussions, constructive feedback, and presence. A special thanks to Reidar Stølen and Rise Fire Research for including me in the research project on PV modules and roof constructions. Reidar has been a very important supporter both in the execution, but also in the pre- and post-work of the experiments, and in the work with this thesis.

In the work with this thesis, I have acquired knowledge about both Computational Fluid Dynamic (CFD) Modelling of fires and research-based work with fire experiments. Furthermore, my wish for this new knowledge is to integrate it into my work as a fire safety engineer within the construction industry.

Finally, I would like to thank my family and friends for the emotional support I have received during this period. I have had to make many selfish choices and limited social interactions over long periods. You have shown complete understanding for this and have been very patient. Thank you very much.

Abstract

In combination with increased population growth, and that the global community has had a global overconsumption of the Earth's resources over a long period, humanity must act differently to reverse the negative trend when it comes to global warming. As part of a new pattern of action, photovoltaic (PV) installations, which are expected to increase by 13% each year from 2020 to 2030 [1], are one of several important measures when it comes to supplying the increased population with renewable energy. In this context, there is relatively little, but increasing research in the field of PV installations and fire safety [2].

In collaboration with RISE Fire Research [3], this thesis has conducted 6 medium and 2 full-scale fire experiments on a 30° sloped roof construction with externally mounted PV modules (BAPV). The roof construction was carried out in accordance with the classification $B_{\text{Roof}}(t_2)$ [4], which is a pre-accepted solution in the Norwegian Building codes (VTEK17) [5]. The roof was constructed from the bottom up; OSB, chipboard, and a bitumen-based roofing membrane. With a distance of 12cm, BAPVs made of stainless steel were mounted parallel to the roof surface. The experiments were conducted outdoors at the RISE Fire Research facility in Trondheim in the autumn of 2021. The project was funded by the Norwegian Directorate for Civil Protection (DSB) and Norwegian Building Authority (DiBK).

The motivation behind the medium-scale experiments was to research the size of a standardized initial fire, which could mirror a realistic brand fire, and which entailed fire development and propagation on the roof surface. The medium-scale experiments were carried out with different sizes of initial fire with both the presence and absence of a PV module. The results from the experiments showed an increase in damage extent and heat transfer inward in the roof construction when using an BAPV compared to experiments without a PV module, especially when UL B-wood crib [6] was used as the initial fire. For this reason, UL B-crib was also used as the initial fire in both full-scale experiments.

Both full-scale experiments gave approximate results with fire propagation in the cavity to the BAPVs, all the way up and past the ridge. Both temperature measurements and damage extent showed that the fire had the greatest propagation in the middle of the roof construction, and with a tendency to propagate towards the right side of the construction. Most likely this had something to do with wind direction. Temperature measurements under the chipboard were relatively low, an indication that there is no immediate danger of fire spread inward in the roof construction.

To recreate the experiments described above, Fire Dynamics Simulator (FDS) was used to simulate a specific small-scale experiment (test setup T4) previously conducted separately by RISE Fire Research [3]. The roof construction in the small-scale experiment had a similar construction and PV module as for the medium and full-scale experiments, but the distance between the PV module and the roof surface was 6 cm, the initial fire was an EN-wood crib [4], and a fan supplied constant 2m/s wind at the roof eaves. It required less computing power to simulate a complete test setup in this scale compared to the medium and full-scale experiments. Lack of data on the material properties of the roofing membrane and the effect of the initial fire necessitated experiments in the lab at Western Norway University of Applied Sciences (HVL), where, among other things, cone calorimeter and thermogravimetric analysis were used. The results of the FDS simulation failed in a satisfactory manner to recreate data from the small-scale experiment. Further work with the FDS model, especially with the pyrolysis model of the roofing membrane, is necessary to approach the results in the RISE Fire Research experiment.

Sammendrag

I kombinasjon med økt befolkningsvekst, og at verdenssamfunnet over en lengre periode har hatt et globalt overforbruk av jordens ressurser, gjør at menneskeheten må handle annerledes for å snu den negative trenden når det kommer til global oppvarming. Som et ledd i et nytt handlingsmønster er solcelleinstallasjoner, som er forventet å øke 13% hvert år fra 2020 til 2030 [1], et av flere viktige tiltak når det kommer til å forsyne den økte befolkningsmassen med fornybar energi. I denne sammenheng er det relativt lite, men økende forskning på fagområdet solcelleinstallasjoner og brannsikkerhet [2].

I samarbeid med RISE Fire Research [3] har det i denne oppgaven blitt gjennomført 6 medium- og 2 fullskala brannforsøk på en 30° takkonstruksjon med utenpåmonterte solcellemoduler. Oppbyggingen av takkonstruksjonen ble utført iht. klassifiseringen $B_{Roof}(t2)$ [4], som er en preakseptert ytelse i Byggteknisk forskrift med veiledning (VTEK17) [5]. Taket ble konstruert fra bunnen og opp; OSB, sponplate og et bitumenbasert takbelegg. Med en avstand på 12cm ble utenpåmonterte solcellemoduler konstruert av rustfritt stål montert parallelt med takflaten. Forsøkene ble gjennomført utendørs ved RISE Fire Research sitt forskningsanlegg i Trondheim høsten 2021. Prosjektet ble finansiert av Direktoratet for samfunnssikkerhet og beredskap (DSB) og Direktoratet for byggkvalitet (DiBK).

Motivasjonen bak mediumskalaforsøkene var å forske på størrelsen til en standardisert startbrann, som kunne speile en realistisk flyvebrann, og som medførte brannutvikling og spredning på takoverflaten. Mediumskalaforsøkene ble gjennomført med ulik størrelse på startbrannen i tillegg til med og uten solcellemodul. Resultatet fra forsøkene viste økning av skadeomfang og varmeoverføring innover i takkonstruksjonen når det ble benyttet utenpåmontert solcellemodul sammenlignet med forsøk uten solcellemodul, særskilt når UL B-trekrybbe [6] ble brukt som startbrann. Av den grunn ble UL B-trekrybbe også brukt som startbrann i begge fullskalaforsøkene.

Begge fullskalaforsøkene ga tilnærmede resultater med brannspredning i hulrommet til solcellemodulene, helt opp og forbi mønet. Både temperaturmålinger og skadeomfang viste at brannen hadde størst spredning i midten av takkonstruksjonen, og med en tendens til å spre seg mot høyre side av konstruksjonen. Mest sannsynlig hadde dette noe med vindretning å gjøre. Temperaturmålinger under sponplaten var relativt lav, en indikasjon på at det er ingen umiddelbar fare for brannspredning innover i takkonstruksjonen.

For å gjenskape forsøkene beskrevet ovenfor ble Fire Dynamics Simulator (FDS) brukt til å simulere et spesifikt småskalaforsøk (testoppsett T4) tidligere utført separat av RISE Fire Research [3]. Takkonstruksjonen i småskalaforsøket hadde tilsvarende oppbygning og solcellemodul som for medium- og fullskalaforsøkene, men avstanden mellom solcellemodulen og takflaten var 6 cm, startbrannen var en EN-trekrybbe [4] og en vifte tilførte konstant 2m/s vind ved takskjegget. Det krevdes mindre datakraft å simulere et komplett testoppsett i denne størrelsesordenen sammenlignet med medium- og fullskalaforsøkene. Manglende data på materialegenskapene til takbelegget og effekten til startbrannen medførte forsøk i brannlabben til Høgskulen på Vestlandet (HVL), der blant annet konekalorimeter og termogravimetrisk analyse-apparat ble brukt. Resultatene fra simuleringen klarte ikke på en tilfredsstillende måte å gjenskape småskalaforsøket. Ytterligere arbeid med FDS-modellen, særlig med pyrolysemodellen til takbelegget, er nødvendig for å nærme seg resultatene i forsøket til RISE Fire Research.

Table of contents

Preface.....	I
Acknowledgements.....	III
Abstract.....	V
Sammendrag.....	VI
Table of contents.....	VII
Table of figures.....	X
Table of tables.....	XIV
Table of abbreviations.....	XV
1. Introduction.....	1
1.1 Background.....	1
1.2 The world energy situation.....	2
1.3 General technical understanding and information of photovoltaic panels.....	3
1.3.1 How does a photovoltaic cell work?.....	3
1.3.2 The Structure of a PV module.....	4
1.3.3 PV system connections.....	5
1.3.4 Flammability of PV modules.....	5
1.4 Aim and objectives.....	8
1.5 Limitations.....	8
2. Theory.....	9
2.1 Flame spread theory.....	9
2.2 Thermogravimetric analysis.....	17
2.3 Cone calorimetry.....	19
2.4 Computational Fluid Dynamics Modelling.....	20
2.4.1 Combustion model.....	22
2.4.2 Pyrolysis model.....	22
2.4.3 Conductive heat transfer.....	25
2.4.4 Mesh resolution.....	26
2.4.5 Orientation.....	27
2.5 Literature review.....	28
2.5.1 2016: Photovoltaic installations on warehouse buildings – an experimental study of the propagation on fire.....	28
2.5.2 2017: Fire-induced re-radiation underneath photovoltaic arrays on flat roofs.....	28

2.5.3	2018: Experimental Study of the Fire Behaviour on Flat Roof Constructions with Multiple Photovoltaic (PV) Panels.....	28
2.5.4	2021: Experimental study of flame spread underneath photovoltaic (PV) modules.....	29
2.5.5	2022: Experimental Study of the Fire Dynamics in a Semi-enclosure Formed by Photovoltaic (PV) Installations on Flat Roof Constructions.....	29
2.5.6	2022: EBOB - Solar cell installations on buildings. Experimental study of fire spread in cavity behind solar cell modules on pitched roof surfaces.	30
3.	Methodology	37
3.1	Experiments conducted in collaboration with RISE Fire Research.....	38
3.1.1	Material, equipment and experimental set-up	39
3.1.2	Medium-scale experiments	40
3.1.3	Full-scale experiments.....	43
3.2	Wood crib burning experiments	47
3.2.1	Cone calorimeter	47
3.2.2	Free burning	49
3.3	Thermogravimetric analysis	51
3.4	Computational Fluid Dynamics Modelling	52
3.4.1	Pyrolysis model.....	53
3.4.2	Model geometry	55
3.4.3	Material properties	57
3.4.4	Reactions	58
3.4.5	Initial fire	59
3.4.6	Device configuration.....	60
3.4.7	Mesh.....	60
4.	Results	61
4.1	Experiments conducted in collaboration with RISE Fire Research.....	61
4.1.1	Medium-scale experiments.....	61
4.1.2	Full-scale experiment	65
4.2	Wood crib burning experiments	72
4.2.1	Cone calorimeter	72
4.2.2	Free burning	73
4.3	Thermogravimetric analysis	75
4.4	Computational Fluid Dynamics Modelling	76
4.4.1	Mesh sensitivity analysis	76

4.4.2	Comparison between FDS and small-scale experiment	79
4.4.3	Parameter sensitivity analysis	84
5.	Discussion	88
5.1	Experiments conducted in collaboration with RISE Fire Research.....	88
5.1.1	Medium-scale experiments.....	88
5.1.2	Full-scale experiments.....	89
5.2	Wood burning experiments	90
5.2.1	Cone calorimeter	90
5.2.2	Free burning	90
5.3	Thermogravimetric analysis	91
5.4	Computational Fluid Dynamics Modelling	92
6.	Conclusion	95
7.	Further work.....	96
8.	References.....	97
9.	Appendix.....	A
	Appendix A – FDS mesh calculations.....	A
	Appendix B – FDS script.....	A

Table of figures

Figure 1: Cumulative installed solar PV capacity worldwide from 2000 to 2022 [14]	2
Figure 2: Inside a photovoltaic cell [19]	4
Figure 3: Schematic view of a PV module [21]	5
Figure 4: A schematic representation of heat transfer mechanisms involved in flame spread of a freely burning flame on a horizontal solid surface. X_h illustrates the pre-heating zone in front of the pyrolysis zone X_p . a) heat transfer mechanics without influence of a PV panel. b) heat transfer mechanics with influence of a PV panel	11
Figure 5: Illustration of change of the mode of surface flame spread according to the slope angle. a) shows counter-current flame spread, b) shows concurrent flame spread.	13
Figure 6: Impact of flame height and the flame's angular orientation of a) open burning, b) $L_f < H$ and c) $L_f > H$. Scenario b) and c) is under influence of a PV panel with different gap height.....	15
Figure 7: Illustration of factors determining rate of burning.	16
Figure 8: A TG curve of asphalt [48], p. 50.	18
Figure 9: Cone calorimeter. The image is sourced from Marc Janssens in SFPE Handbook [52], p. 926....	19
Figure 10: Results from the TGA experiment conducted on Icopal Topsafe at HVL. The mass fraction W/W_0 of Icopal Topsafe is represented by the blue curve, undergoing heating at 10 K/min. The reaction rate is represented by the orange curve dY_s/dt . The ordinary differential equation that describes the transformation is shown at right. Note that the parameters T_p , r_p , and V_s represent the reference temperature, reaction rate, and residue yield of the single reaction. From these parameters, values of A and E can be estimated using the Eq. 11.....	25
Figure 11: Illustration of the experimental setup used for the small-scale experiments with the PV panel positioned 12cm above the roof surface and with a wind speed of 2m/s. The image is sourced from Stølen et al.[3], p. 10.	31
Figure 12: Picture of the mock-up PV module used in the small-scale experimental setup. The mounting brackets and thermocouples are attached on top of the plate. The image is sourced from Stølen et al.[3], p. 11.....	31
Figure 13: Illustration of the construction of an EN-crib.....	32
Figure 14: A schematic illustration of the instrumentation and test setup for the small-scale experiments. The figure is a modified reconstruction of an illustration made Stølen et al.[3], p. 11	32
Figure 15: Length of the damaged area of the roof covering after the experiments for different distances between the roof covering and PV panel at two different wind speeds. The black dashed line shows the requirement for classification for $B_{ROOF}(t_2)$, which is $\leq 55,0\text{cm}$ for the average [58]. The image is sourced from Stølen et al.[3], p. 19, where the text is translated to English.	34
Figure 16: Temperature increase measured below the particleboard for one experiment conducted without a PV panel (dashed lines) and two experiments with a PV panel mounted 6cm above the roof surface (solid lines). The temperatures shown with PV panel is an average of two experiments. The image is sourced from Stølen et al.[3], p. 20, where the text is translated to English.	35
Figure 17: Temperature in the PV panel that was mounted 6 cm above the roof surface. The temperatures are an average of two experiments with 2 m/s wind. The image is sourced from Stølen et al.[3], p. 21, where the text is translated to English.	36
Figure 18: Flowchart illustrating the work process used to answer the aim and objectives of this thesis	37
Figure 19: Illustration of how the PV module was constructed, and the placement of the two spot-welded thermocouples	40

Figure 20: Illustration of the four different sizes of initial fire tested in the medium-scale experiments. I) 1 x EN-crib, II) 2 x EN-cribs stacked on top of each other, III) 3 x EN-cribs stacked on top of each other and IV) 1 x UL B-crib.	41
Figure 21: A schematic illustration of the instrumentation and test setup for the medium-scale experiments. The figure is a modified reconstruction of an illustration made by Stølen et al.[3], p. 15 ...	42
Figure 22: Illustration of the test setup used in the medium-scale experiments; I) test M3 without a PV panel and II) test M4 with a PV panel.	43
Figure 23: Illustration of the dimensioned test setup for the full-scale experiment.	44
Figure 24: Illustration showing the instrumentation for the test setup in the full-scale experiment. In the middle column of PV modules, where the initial fire is located, temperatures were measured in three layers of the roof construction as well as on the top of the stainless-steel mock-up PV panel. The codes UC, OC, R, and PV indicate which layer of the roof construction the thermocouple was placed: UC – under chipboard, OC – over chipboard, R – roofing membrane, PV – on top of the PV module. For the two outermost columns of PV modules, temperatures were measured on top of the roofing membrane, as well as on the top of the PV panel.	45
Figure 25: Section view of the center of the roof construction where the initial fire is located. The figure is a schematic illustration of the instrumentation and test setup for the full-scale experiment.	46
Figure 26: Illustration showing the changes from the test setup in experiment F1 to experiment F2; a steel gutter was installed at the eaves to collect melted roofing membrane, and the middle part of the roof construction was extended by 1 m in length and 1,3 m in width.	47
Figure 27: Illustration of the test setup used for the burning of EN-cribs in the cone calorimeter; I) Illustration of how the wooden crib was placed directly in the sample pan without a retainer frame. II) Picture showing a burning EN-crib in the cone calorimeter.	48
Figure 28: Illustration of the test setup for free burning of UL B-cribs; I) test setup for experiments 1-3 with cribs placed on a solid surface II) test setup for experiment 4 with crib placed on a metal grate with a 5 cm gap height to a solid surface.	50
Figure 29: The apparatus used to perform the TGA was of the type Netzsch STA 499 F3 Jupiter. The figure is sourced from a brochure on Netzsch's website [65].	51
Figure 30: Illustration of the TGA test setup.	52
Figure 31: Representation of spruce and Icopal Topsafe's single reaction scheme.	53
Figure 32: Results from the TGA experiment conducted on Icopal Topsafe at HVL. The mass fraction W/W_0 of Icopal Topsafe is represented by the blue curve, undergoing heating at 10 K/min. The reaction rate is represented by the orange curve dY_s/dt . The reference temperature, reaction rate, and residue yield represent the parameters of the multiple reactions.	53
Figure 33: Schematic figure of the modelling of wood cribs.	56
Figure 34: Snippets of model geometry.	56
Figure 35: A series of three EN-cribs were tested using the cone calorimeter to acquire data for the initial fire used in the model. The experimental data for the heat release rate is illustrated in the figure above.	59
Figure 36: Illustration of the positioning of the solid-phase devices measuring temperatures in FDS.	60
Figure 37: An illustration of the experiment with test setup M4; UL B-crib and PV module.	62
Figure 38: Overview showing measured temperatures in two positions in the different layers of the construction, as well as on top of the PV module for the setups M3-M6. The M3 experiment was carried out without a PV module. The M1 and M2 experiments were not instrumented for temperature	

measurements. The Y-axis shows temperatures (Celsius) that are common for all figures in the same row. The X-axis shows time (minutes) which is individual per figure. The blue curve shows the measured temperature 900mm from the eaves/in the centre of the wooden crib/30cm from the lower end of the PV module. The orange curves show the measured temperature 2000mm from the eaves/30cm from the upper end of the PV module. The figure shows 4 columns, each column corresponding to the described test setup at the top of the figure. 63

Figure 39: Overview showing the extent of damage to the roofing membrane in the medium-scale experiments. a)-c) show the extent of damage from experiments without PV module. d)-f) show the extent of damage from experiments with PV module. Red squares illustrate the approximately placement and size of the wooden cribs..... 64

Figure 40: Overview images from experiment F1 65

Figure 41: Illustration showing the melted roofing membrane at the eaves in both experiments. In experiment F1 a) the roofing membrane was collected on the ground, while in experiment F2 b) the roofing membrane was collected in a gutter. Only in experiment F1 did the fire spread downwards in the roof construction..... 66

Figure 42: An overview of the temperatures measured on top of the PV modules and on the roofing membrane for experiments F1 and F2. Temperature measurements were made in the centreline of the three columns of PV modules in both experiments. The Y-axis shows temperatures (Celsius) that are common for all figures in the same row. The X-axis shows time (minutes) which is individual per figure.68

Figure 43: An overview of the temperatures measured above and below the chipboard in the centreline of the middle PV modules in both experiments. The Y-axis shows temperatures (Celsius) that are common for all figures in the same row. The X-axis shows time (minutes) which is individual per figure.69

Figure 44: An overview of the extent of damage for experiments F1 and F2. Red squares illustrate the placement of PV modules, and a yellow square illustrates the placement of the wooden crib. 70

Figure 45: Marks from burn-through at the joint of the chipboards in experiment F1. The burn mark did not increase further after experiment F2 71

Figure 46: Depth of charring in the chipboards shown by cross-section in the same positions as the temperature measurements were made 72

Figure 47: A series of three EN-cribs were tested using the cone calorimeter to acquire data for the initial fire used in the FDS model. The mean experimental data for the heat release rate is illustrated in the figure above..... 72

Figure 48: Mass loss rate for experiment a) CC1 and b) CC2. Corrupted/damaged data file for CC3 could not be used..... 73

Figure 49: Overview of; a) mass fraction of the UL B-cribs and b) mass loss rate of the UL B-cribs. The measurements started after 4 minutes of ignition with a propane burner..... 74

Figure 50: Results from the TGA experiment conducted on Icopal Topsafe. The mass fraction W/W_0 of Icopal Topsafe is represented by the blue curve, undergoing heating at 10 K/min. The reaction rate is represented by the orange curve dY_s/dt . The ordinary differential equation that describes the transformation is shown at right. Note that the parameters T_p , r_p , and V_s represent the reference temperature, reaction rate, and residue yield of the multiple reactions. 75

Figure 51: Comparison between the variable mesh resolution δx parameter (5mm, 10mm and 20mm) and small-scale experiments; temperature measurements on top of the roofing membrane at a position of 300mm from the eaves. 77

Figure 52: Comparison between the variable mesh resolution δx parameter (5 mm, 10 mm and 20 mm) and cone calorimeter experiments set against total heat release rate. 78

Figure 53: Comparison between FDS and small-scale experiments; a) temperature measurements on top of the PV module and b) temperature measurements on the roofing membrane. Temperature measurements made in the experiment are shown with solid lines, while dashed lines represent measurements made in FDS..... 80

Figure 54: Comparison between FDS and small-scale experiments; a) temperature measurements on top of the chipboard and b) temperature measurements below the chipboard. Temperature measurements made in the experiment are shown with solid lines, while dashed lines represent measurements made in FDS..... 81

Figure 55: Comparison of HRR for EN-crib measured in FDS and cone calorimeter tests. 82

Figure 56: Temperature slices in the middle of the model presented at different times; a) 5 sec, b) 20 sec, c) 90 sec, d) 120 sec, e) 150 sec and f) 200 sec 83

Figure 57: Small-scale experiment T4 with 2 m/s wind and 6 cm gap height between the PV module and roofing membrane, here shown; a) after 120 sec, b) 150 sec, c) 200 sec, and d) 480 sec 84

Figure 58: Temperature measurements made in the experiment are shown with solid lines, while dashed lines represent measurements made in FDS. The exception is measurements of HRR where the orange line is data from the cone calorimeter test and the black line is data from FDS. The x-axis shows time (min) and the y-axis shows temperature (°C)/HRR (kW). Both x-axis and y-axis are common for all figures in the same column. 86

Figure 59: Comparison between the “main model” with mesh cell size 0,005 m and ref. temp 450 °C shown on the right side, and the sensitivity analysis with mesh cell size 0,01 m and ref. temp 300 °C shown on the left side. The remaining parameters and temperature scale is the same for both simulations. Temperature slices in the middle of the model presented at different times; a) 5 sec, b) 20 sec, c) 90 sec, d) 120 sec, e) 150 sec and f) 200 sec. 87

Figure 60: Amount of scraped-off waste from burned roofing membrane after one of the full-scale experiments. Additionally, there was melted roofing membrane on the ground that is not included in this waste 92

Table of tables

Table 1: Overview of studies on the flammability of photovoltaic modules	6
Table 2: Factors affecting rate of flame spread over combustible solids. The table is sourced from Friedman [33]	12
Table 3: A summary displaying the quantity of individual trails in the various types of setups [3]	33
Table 4: Overview of the test setup for the six medium-scale experiments	42
Table 5: Overview of the test setup for the cone calorimeter experiments.....	49
Table 6: Overview of the test setup for the free burning wood crib experiments	50
Table 7: Overview showing the setup of the parameter sensitivity analysis in FDS for the parameters reference temperature and pyrolysis range. The cell size of 0,01m remained the same in all analyses. The starting point for the parameters was a reference temperature of 450°C and a pyrolysis range of 200°C	54
Table 8: Overview of adjustments between small-scale experiment [3] and FDS model geometry	55
Table 9: Material properties used in the setup of the FDS model.	57
Table 10: A representation of the mesh resolution used for sensitivity analysis. For calculations, see Appendix A – FDS mesh calculations.....	61
Table 11: Summary of measured damage extent on the roofing membrane in the medium-scale experiments. The length of the damaged area was measured from the centre of the wooden crib upwards along the roof surface, while the width was measured at the point where the damage area was widest.	64
Table 12: Observation log from the two large-scale experiments F1 and F2. The log is sourced from Stølen et al. [3] p. 27.	66
Table 13: Depth of charring in the OSB (oriented strand board) beneath the roofing material along the centreline of the roof for the two large-scale experiments F1 and F2. The table is sourced from Stølen et al. [3] p. 32.....	71
Table 14: Experimental overview for the cone calorimetry test.....	73
Table 15: Overview of weight loss across all experiments where UL B-cribs were burned in a well-ventilated indoor test lab	74
Table 16: Mesh sensitivity analysis. Average and peak temperature in the timeframe between 0 sec to 240 sec.....	77
Table 17: Mesh sensitivity analysis. Average and peak total HRR for each mesh resolution in the timeframe between 0 sec to 120 sec.	79
Table 18: Overview showing the setup of the parameter sensitivity analysis in FDS for the parameters reference temperature and pyrolysis range. The cell size of 0,01m remained the same in all analyses. The starting point for the parameters was a reference temperature of 450°C and a pyrolysis range of 200°C	85

Table of abbreviations

Abbreviation	Definition/description
A	Pre-exponential factor (constant) in the Arrhenius equation
ASTM	American Society for Testing and Materials
BAPV	Building-applied photovoltaic
BIPV	Building-integrated photovoltaic
CEN	The European Committee for Standardization
CFD	Computational Fluid Dynamics
Copper plate IMO	Thermocouple brazed to a copper disk standardized accordance to International Maritime Organization
DiBK	Norwegian Building Authority/Direktoratet for byggkvalitet (Norwegian)
DIN	Deutsches Institut Fur Normung E.V. (German National Standard)
DNS	Direct Numerical Simulations
DSB	The Norwegian Directorate for Civil Protection/Direktoratet for samfunnsikkerhet og beredskap (Norwegian)
E	Activation energy of a reaction
EN	European standard
EN-crib	Wooden crib standardized accordance test method 2 in CEN/TS 1187
EPS	Expanded Polystyrene
EVA	Ethylene-vinyl acetate
FDS	Fire Dynamics Simulator
FVM	Finite Volume Method
HRR	Heat Release Rate
HVL	Western Norway University of Applied Sciences/Høgskulen på Vestlandet (Norwegian)
IPCC	Intergovernmental Panel on Climate Change
ISO	International Organization for Standardization
LES	Large Eddy Simulation
MLR	Mass Loss Rate
MPI	Message Passing Interface

NBS	National Bureau of Standards
NFPA	National Fire Protection Association
OSB	Oriented Strand Board
PET	Polyethylene terephthalate
PIR	Polyisocyanurate
PV	Photovoltaic
PV panel/module	Photovoltaic panel/module
PVF	Polyvinyl fluoride
RANS	Reynolds-averaged Navier-Stokes
TGA	Thermogravimetric analysis
THR	Total Heat Release
TPT	Tedlar Polyester Tedlar
UL	Underwriter Laboratories
UL B-crib	Wooden crib standardized accordance Underwriter Laboratories UL790
VTEK	Pre-accepted solution in the Norwegian Building codes/Veiledning til Byggt teknisk forskrift (Norwegian)

1. Introduction

This thesis includes results and conclusions based on: I) six medium-scale and two full-scale experiments investigating fire dynamics in the cavity between an inclined roof construction and mock-up BAPVs, II) three cone calorimetry experiments on wooden cribs used in the experiments, III) four experiments on free-burning of wooden cribs in a well-ventilated lab, IV) one TGA experiment on the roofing membrane used in the experiments and V) a series of CFD simulations aiming to recreate test setup (T4) of a small-scale experiment separately conducted by Stølen et al [3].

1.1 Background

As the number of people on earth increases, so does the need for renewable energy as global warming has become an increasingly pressing problem since the mid-19th century. Solar PV is set to expand by an average of 13% per year from 2020 to 2030, which is predicted to be the largest growth of any renewable energy source [1]. Statistics in Europe and the rest of the world show that PV-related fires have increased in line with the number of installed PV modules. A qualitative fault tree analysis identified seven major events as potential ignition sources for PV-related fires, with arcing being the primary contributor. The average annual frequency of such fires was calculated to be 0,0289 per MW of installed capacity using a weighted mean. Focusing on mitigating consequences in case of ignition could effectively reduce overall fire-related risks in building-applied PV installations. Improved understanding of fire dynamics, design, and installation practices could significantly reduce risks [7]. There are variations in regulations, standards, and guidelines across different countries and regions. An example from Europe is that within the standardization organization CEN, there is disagreement over whether PV modules should be treated as electrical installations, building components, or a combination of these. The current test methods in the standards for external fire exposure, which consider PV modules and roofs separately, may pose a risk that the synergistic effect of the combination of BAPV and roofs is overlooked. In 2017, the European Committee for Electrotechnical Standardization (CENELEC) published a technical report CLC/TR 50670 "*External fire exposure to roofs in combination with photovoltaic (PV) arrays - Test method(s)*" [8], which addresses test methods for assessing the external fire exposure to both tilted and flat roofs in combination with Building-applied photovoltaic (BAPV) arrays. This report characterizes the potential impacts of BAPV arrays on the existing fire rating of roofs from an external fire exposure. "*A Technical Report (TR) is a European document containing informative descriptions that are not suitable for publication as a European Standard or Technical Specification (TS)*" [9]. CEN is now engaged in ongoing work to find a comprehensive approach to PV installations [10], [2].

In the fall of 2022, a series of six medium-scale experiments and two full-scale experiments were conducted to investigate the impact of building-applied photovoltaic (BAPV) panels on the propagation of fire along a 30° sloped roof construction. The tests were conducted outdoors at the RISE Fire Research facility in Trondheim. The roof covering used in the tests was Icopal Topsafe [11], a single-layer asphalt roof covering that according to testing method CEN/TS 1187 test 2 [4] is classified as B_{ROOF} (t2) on a wood substrate. FDS modelling were used to recreate the test setup T4 used in the small-scale experiments by Reidar Stølen et al. [3]. A properly set up FDS model can provide good indications and be a tool to further research new issues. The FDS model could be a time- and cost-saving way to conduct new research compared to full-scale tests.

The medium- and full-scale experiments described in this thesis were conducted in collaboration with RISE Fire Research in a project funded by The Norwegian Directorate for Civil Protection (DSB) and Norwegian Building Authority (DiBK).

1.2 The world energy situation

The IPCC's Sixth Assessment Report on Climate Change [12] asserts that the average global surface temperature is likely to continue rising, potentially exceeding 1,5-2°C (compared to pre-industrial global temperatures in the mid-19th century) during the 21st century, unless substantial reductions in CO₂ and other greenhouse gas emissions transpire in the forthcoming decades. The United Nations projects that the global population will grow from the current 7,7 billion to 9,7 billion by 2050 [13]. This population increase will inevitably lead to a heightened demand for energy.

To accommodate future energy needs while safeguarding the planet, the emphasis must be placed on renewable energy sources. Global electricity demand is anticipated to rise from approximately 24'500 TWh to 29'000 TWh between 2019 and 2030, constituting an increase of 4'500 TWh (approximately a 20% increase). To put this into perspective, 4'500 TWh exceeds the present electricity demand in the United States. Innovation, ongoing technological advancements, and abundant resources are predicted to contribute to a decline in the cost of renewable electricity production technologies, such as solar photovoltaic (PV) panels. Since 2010, the average generation costs for solar PV have decreased by 80%, with a further 40% reduction expected by 2040.

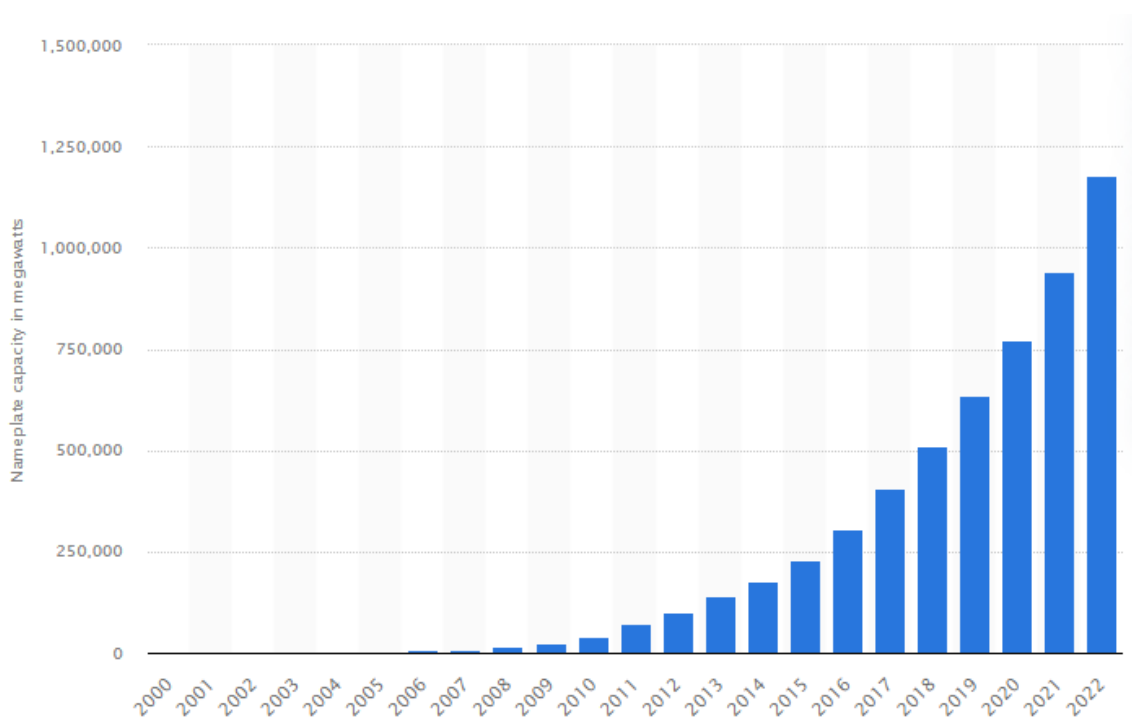


Figure 1: Cumulative installed solar PV capacity worldwide from 2000 to 2022 [14]

Solar photovoltaic (PV) technology is projected to experience an average annual growth rate of 13% from 2020 to 2030, representing the most substantial expansion among all renewable energy sources [1]. The motivations for installing PV panels extend beyond making positive local and global contributions towards reducing greenhouse gas emissions, encompassing various benefits for both individuals and corporations:

- Incentives such as governmental funding, subsidies and tax credits.
- Potential reduction in energy costs.
- Generation of revenue through the sale of surplus energy production.
- Utilization of PV panels as a means to convey an environmentally conscious image, signalling a commitment to responsibility, future-readiness, and environmental stewardship – a message that resonates strongly in contemporary society.

1.3 General technical understanding and information of photovoltaic panels

Photovoltaic cells, a term originating from the Greek word "phos" (meaning "light") and "volt" (the unit of electromotive force, named in honour of Italian physicist Alessandro Volta), convert photons into electricity [15]. Approximately 95 % of contemporary photovoltaic cells are composed of silicon, one of the most abundant elements on Earth [16], [17].

1.3.1 How does a photovoltaic cell work?

Rossing et. al. [18] elucidate that silicon atoms are interconnected in a crystal lattice, wherein adjacent atoms share outer shell electrons, resulting in the fulfilment of the octet rule. However, a crystal lattice is an inferior conductor. To enhance the silicon's electrical conductivity, trace amounts of boron and phosphorus are introduced, creating impurities in the silicon structure (doped silicon). As boron and phosphorus possess three and five outer shell electrons, respectively, they generate a deficit (p-type) and a surplus (n-type) of electrons. At the junction (pn-junction) where p-type and n-type silicon meet, an electron exchange occurs, leading to a voltage difference that inhibits further electron flow [15].

Upon exposure to photons, electrons in the pn-junction are energized, enabling them to overcome the voltage difference and be captured by a negatively charged metal grid on the photovoltaic cell's surface. This capture creates vacant positions (holes) that migrate towards the cell's metal-coated (positively charged) backside. When the front and back are connected, an electric field emerges between them. Consequently, as photons interact with the photovoltaic cell, electricity is generated [15].

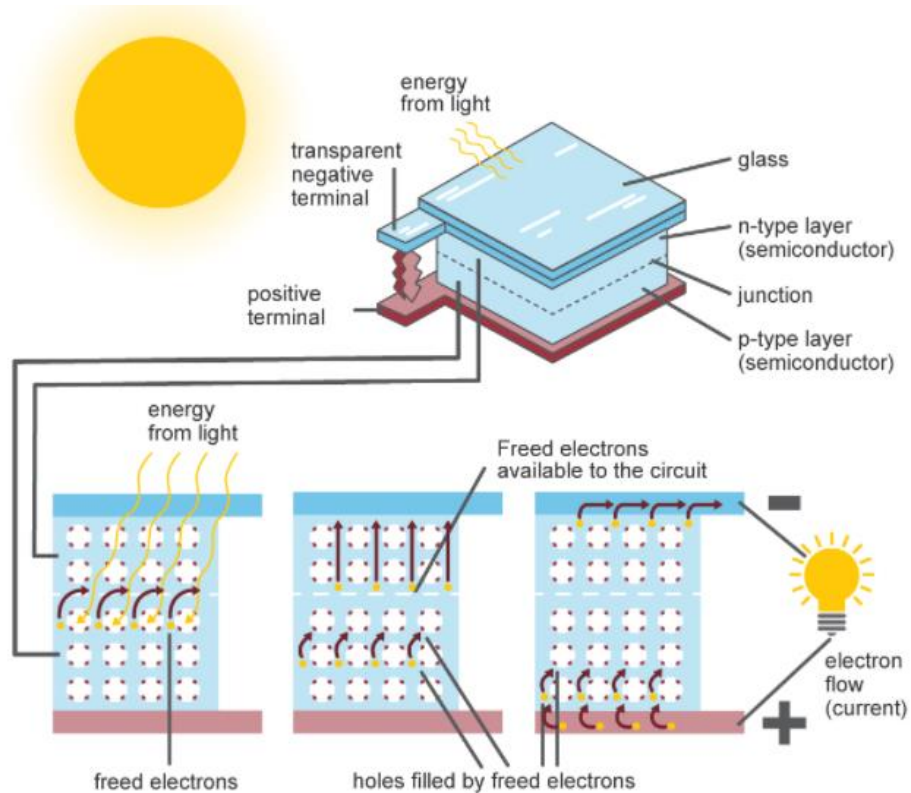


Figure 2: Inside a photovoltaic cell [19]

1.3.2 The Structure of a PV module

A conventional PV module features a five-layer structure, arranged in the following order from top to bottom [20]:

- A low-iron content tempered glass layer characterized by high transmittance, which imparts mechanical strength, safeguards the PV module from physical damage, and permits light transmission to the solar cells.
- An ethylene-vinyl acetate (EVA) encapsulating film, representing the primary combustible component.
- Solar cells responsible for converting solar radiation into electricity.
- A secondary layer of EVA film.
- A terminal back-sheet layer designed to protect the PV module from ultraviolet radiation and moisture. This flammable layer is composed of various materials, such as Tedlar Polyester Tedlar (TPT), Polyvinyl fluoride (PVF), and Polyethylene terephthalate (PET).

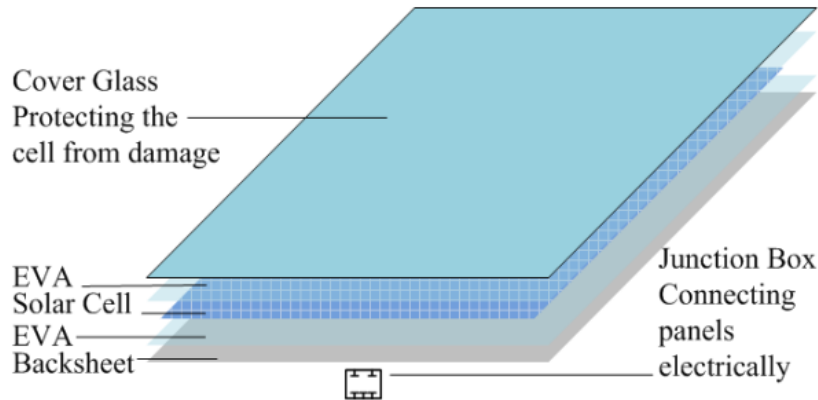


Figure 3: Schematic view of a PV module [21]

1.3.3 PV system connections

A photovoltaic module comprises multiple solar cells electrically interconnected. Depending on the technology and dimensions, photovoltaic modules typically exhibit a power output ranging from 290-500W. A PV system is constituted by one or more PV modules arranged in an array. Three distinct types of PV systems exist [17]:

- On-grid: This PV system is interconnected with the local utility grid, allowing the utility provider's system to function as a battery.
- Off-grid: An independent PV system that is not connected to the electrical grid; all energy generated is stored on site within a battery.
- Hybrid: A PV system that maintains connections to both the electrical grid and local energy storage via a battery.

1.3.4 Flammability of PV modules

Table 1 provides a summary of experimental studies examining the flammability of photovoltaic modules. The combustible components are characterized by intermediate low risk in terms of heat contribution, exhibiting a total heat release (THR) ranging from 38-80 MJ/m². Reidar Stølen along with several researchers from RISE Fire Research are the authors of the research article "Large-scale fire test of a building integrated photovoltaic (BIPV) facade system"¹, where they have researched the combustibility of BIPV among other things. Part of the conclusion the researchers reached was that modules have high peak heat release rates and low total heat release. The results suggest that the majority of components within a PV module are non-combustible, with the combined mass of

¹ The article is under peer review in Fire Safety Journal. The information was obtained from email correspondence with Reidar Stølen on 06.11.2023 [78]. Reidar has stated that a possible reason for the low results regarding combustible components in PV modules (1%) in Kristensen et al. [18] study might be that they did not account for the combustible layers (EVA and PVF) that are laminated to the glass in the PV modules. In the first modules Reidar burned in the BIPV facade experiment, the plastic that was laminated to the glass constituted 10,5% of the module's mass, the junction box 0,8%, cable insulation 0,5% and connectors 0,2%.

combustible components constituting approximately 12% of the module's total mass. This is consistent with the findings of Sander et al. [22] and van Veen et al. [23], who respectively found about 10% and 14% combustible components within a PV module. Kristensen et al. [24], however, describe that they have measured high values for heat of combustion by bomb calorimetry of two PV panels, but concluded that the amount of combustible components represents less than 1%. The minimal fuel load represented by PV modules aligns with the findings of Kristensen et al. [25], who conducted full-scale experiments on horizontal flame spread beneath PV modules, utilizing both real PV modules and mock-up PV modules (constructed with a 3 mm thick black stainless-steel plate). The study concluded that there was no significant difference in flame spread or fuel load between the PV module and mock-up PV module scenarios.

Table 1: Overview of studies on the flammability of photovoltaic modules

Report/article	Test set-up	Results and conclusions
<i>"Experimental Studies on the Flammability and Fire Hazards of Photovoltaic Modules"</i> , 2015 [21]	Five bench-scale experiments were conducted to investigate the flammability and fire hazards of polycrystalline silicon PV modules, utilizing a cone calorimeter with varying heat fluxes. The experiments employed identical specimen types and examined heat fluxes of 28, 30, 35, 40, and 45 kW/m ² .	THR: 38-57 MJ/m ² . PV modules are at intermediate low risk to heat contribution.
<i>"Experimental study on fire behaviors of flexible photovoltaic panels using a cone calorimeter"</i> , 2017 [26]	Flexible photovoltaic panels (FPV) and PET + TPT samples were subjected to a cone calorimeter test, wherein the heat flux was incrementally increased from 20 to 70 kW/m ² in steps of 10 kW/m ² . This experimental approach aimed to closely examine the total heat release (THR) related to FPV.	THR: 79 ± 0,6 MJ/m ² . PV modules are at intermediate low risk to heat contribution. The report concludes that PET is the main component responsible for degradation and burning of photovoltaic panels
<i>"Combustion Behaviors of CIGS Thin-Film Solar Modules from Cone Calorimeter Tests"</i> , 2018 [27]	The report investigates thermal properties and combustion behaviour of CIGS (copper, indium, gallium and selenium) thin-film modules. Cone calorimeter experiments was	THR: 38-78 MJ/m ² for CIGS module and 38-57 MJ/m ² for Si module. PV modules are at intermediate low risk to heat contribution.

	<p>conducted at external heat fluxes ranging from 20 to 45 kW/m², increasing in increments of 5 kW/m².</p>	
<p><i>“Fire risk assessment of solar cell array installations on large buildings. How to protect the building in case of fire”, 2015 [28]</i></p>	<p>Physical properties pertinent to fire safety were assessed for two unidentified types of PV panels to address the question, "Does the PV panel contribute to a fire?". Each of the two panels was divided into distinct sections to ascertain critical heat flux and heat of combustion, which broadly characterize a material's propensity for ignition and the potential fire load. The individual components extracted from the panels were analysed using a bomb calorimeter.</p>	<p>The study's findings revealed that the primary fire load originates from the cables responsible for transmitting current from the panels (DC cables) to the transformer. These cables exhibited an average heat of combustion of approximately 23 kJ/g. The mass of the other components was so limited that it was deemed insignificant in terms of fire load. Although each individual component displayed substantial combustion heat (ranging from 5 to 45 kJ/g), it was observed that the combined mass of combustible components constituted less than 1% of the panels' total mass (approximately 20 kg), resulting in a minimal overall fuel load.</p> <p>The critical heat flux for the cable was determined to be between 9 and 10 kW/m², while the panels themselves exhibited a range of 15 to 25 kW/m².</p>

1.4 Aim and objectives

The aim of this thesis is to investigate of what impact building-applied photovoltaic (BAPV) panels have on the propagation of fire along a 30° inclined roof construction. As part of the work with this thesis and in collaboration with RISE Fire Research in Trondheim, 6 medium-scale and 2 full-scale experiments were conducted on a roof construction with mock-up BAPVs, as part of a project funded by The Norwegian Directorate for Civil Protection (DSB) and Norwegian Building Authority (DiBK) [10], [3]. RISE Fire Research [3] has independently conducted 21 small-scale experiments with the same test setup, which this thesis aims to model with use of CFD to recreate the findings from the experiment T4 (2 m/sec wind and 6 cm gap height between the PV module and the roof construction). This process involves conducting TGA of the roofing membrane and cone calorimeter tests of wooden cribs (the fire source used in the experiments) as input for the CFD model. The results from the simulations will then be compared to the actual experimental data from the small-scale experiment to assess the model's accuracy. The primary objective is to provide insights into the effectiveness of CFD in modelling the propagation of fire along a 30° sloped roof construction with BAPVs, and to identify any limitations or areas for improvement in the modelling process.

Research Question 1: How is a typical $B_{\text{Roof}}(t_2)$ [4] roof construction affected by a realistic firebrand when the roof construction has parallel-mounted mock-up BAPVs?

- Sub-question 1-1: What size must the initial fire (realistic firebrand) be for the fire to develop and propagate in the cavity between the PV module(s) and the roof construction?
- Sub-question 1-2: What temperatures are measured in the different layers of the roof construction and on the PV modules?
- Sub-question 1-3: What is the extent of damage in the different layers of the roof construction?

Research Question 2: Can the results of Stølen et al. [3] small-scale experiment T4 be recreated using CFD?

- Sub-question 2-1: To what degree of accuracy can the initial fire used in small-scale experiments be recreated using cone calorimetry, to then use these data as one of several parameters in the CFD model?
- Sub-question 2-2: To what degree of accuracy can the pyrolysis of the roofing membrane used in small-scale experiments be recreated in the CFD model using TGA, as one of several parameters?
- Sub-question 2-3: What is the CFD model's level of accuracy to small-scale experimental data?

1.5 Limitations

This thesis is limited to a 30° roof construction (classified $B_{\text{Roof}}(t_2)$ [4]) built from the ground up; OSB, chipboard, and a bitumen-based roofing membrane (Icopal Topsisafe). This type of roof construction is built in accordance with pre-accepted solutions in the Norwegian Building codes [5]. Parallel to this roof construction, mock-up BAPVs (stainless steel) will be used, with a distance of 12 cm to the roof construction.

FDS is the software that will be used for simulation. Available hardware resources and the timeframe allocated for the completion of this thesis will be limitations for the simulations. The simulations in the thesis are based on recreating Stølen et al. [3] small-scale experiment T4.

2. Theory

This chapter will provide an overview of the theoretical background for the four main parts in this thesis: I) medium- and full-scale experiments investigating fire dynamics in the cavity between an inclined roof construction and mock-up BAPVs, II) cone calorimetry experiments on wooden cribs, III) TGA experiment on the roofing membrane and IV) CFD simulations aiming to recreate test setup T4 of a small-scale experiment conducted by Stølen et al [3]. Additionally, this chapter offers a brief literary representation of recent research within corresponding topics. The aim is to offer a comprehensive understanding of the relevant academic context in order to facilitate a thorough examination of the subject matter.

2.1 Flame spread theory

A flame fire is characterized by gas-based combustion, necessitating adequate fuel, oxygen, heat, and a chain reaction for initiation and sustenance of the combustion process. The ignition phase involves the decomposition or pyrolysis of solid matter into gaseous form, which demands the highest energy input. This transformation occurs either through sublimation or via a two-step process involving melting to liquid and subsequent evaporation to gas. The mass loss rate, referring to the quantity of gas evaporated from a solid, is contingent upon the surface area, substance type, and the influence of external radiation on the substance. Combustion of a gas mandates an appropriate mixture with oxygen, wherein the mixing ratio between the gas and oxygen must fall within the upper and lower flammability limits. Furthermore, ignition is influenced by factors such as temperature and pressure. The initial phase of the fire process, ignition, necessitates sufficient energy release from a chemical reaction to enable the reaction's continuation without external energy input. The criteria for solid material ignition are determined by the critical heat flux and are dependent on the ignition source type and the ambient air temperature. For the fire process to progress, heat production must surpass heat loss, and the combustion zone must be provided with opportunities for expansion. Lastly, the ignited material's unit state strength bears implications on the required intensity of the ignition source for successful material ignition [29]. A crucial factor influencing the propagation of a fire is the preheating of combustible materials, which results from heat transfer through conduction, convection, and radiation. Preheated materials are more susceptible to ignition compared to colder ones when exposed to the advancing flame front. In the absence of preheating, fire spread may either cease or proceed at a considerably slower pace [30]. Radiative heat transfer serves as the predominant mode of heat transport, with material properties, temperature, and visual factors contributing to the extent of energy transferred. The heat radiation exchanged between two objects is contingent upon their geometric orientation, encompassing the angle of the incoming radiation relative to the surface's normal vector, in addition to the direction vector in relation to the normal angle of the radiating surface [29].

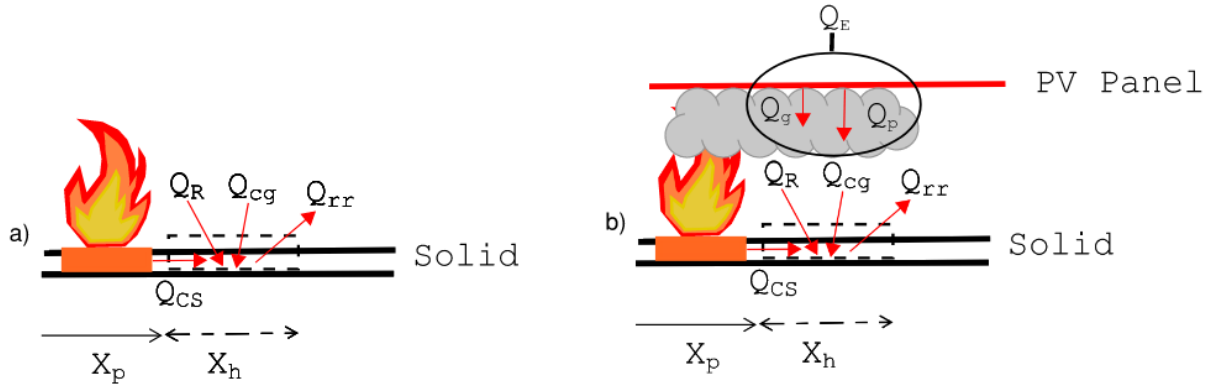
Employing the principle of energy conservation, Williams [31] formulated a relationship known as the fundamental equation of fire spread:

$$\rho V \Delta h = \dot{q} \quad \text{Eq. 1}$$

Where

\dot{q}	Rate of heat transfer across the surface	[W/m ²]
ρ	Fuel density	[kg/m ³]
V	Rate of spread	[m/s]
Δh	Change in enthalpy as unit mass of fuel is raised from its initial temperature to the temperature corresponding to the firepoint	[J/kg]

Examining the flame spread of a freely burning flame on a horizontal surface, the three primary heat transfer mechanisms are radiation from the flame, convection through the gas ahead of the flame, and conduction through the solid fuel [32]. To analyze the different mechanisms of heat transfer from the flame to the unaffected material ahead, Ray et al. [32] created the following energy balance (Eq. 2).



$$Q_{net} = Q_{cs} + Q_{cg} + Q_R - Q_{rr}$$

Where

Q_{net}	Net outward heat flow
Q_{cs}	Heat conducted through the solid
Q_{cg}	Heat conducted through the gas/convection
Q_R	Heat transferred by radiation from the flame
Q_{rr}	Heat reradiated at the fuel surface

Eq. 2

$$Q_{net} = Q_{cs} + Q_{cg} + Q_R + Q_E - Q_{rr}$$

Eq. 3

Where

Q_{net}	Net outward heat flow
Q_{cs}	Heat conducted through the solid
Q_{cg}	Heat conducted through the gas/convection
Q_R	Heat transferred by radiation from the flame
Q_E	External radiation (includes heat flux from PV panel Q_p + heat flux from accumulated gas/smoke Q_g)
Q_{rr}	Heat reradiated at the fuel surface

Figure 4: A schematic representation of heat transfer mechanisms involved in flame spread of a freely burning flame on a horizontal solid surface. X_h illustrates the pre-heating zone in front of the pyrolysis zone X_p . a) heat transfer mechanics without influence of a PV panel. b) heat transfer mechanics with influence of a PV panel.

Although various heat transfer modes contribute to a certain degree, comprehending the predominant mechanism facilitates the formulation of a streamlined characterization of the fire propagation process, in conjunction with an understanding of how diverse factors influence flame spread in the given scenario. Friedman [33] recognized a number of factors that impact the flame spread rate across combustible solid materials (listed in Table 2).

Table 2: Factors affecting rate of flame spread over combustible solids. The table is sourced from Friedman [33]

Material factors		Environmental factors
Chemical	Physical	
Composition of fuel	Initial temperature	Composition of atmosphere
Presence of retardants	Surface orientation	Pressure of atmosphere
	Direction of propagation	Temperature
	Thickness	Imposed heat flux
	Thermal capacity	Air velocity
	Thermal conductivity	
	Density	
	Geometry	
	Continuity	

In several previous experiments; Kristensen et al. [24], [25], [34], [35] studied flame spread and heat flux in flat roofs and sloped PV modules, Stølen et al. [3] studied fire propagation under BAPV modules on sloped roofs and Tang et al. [36] studied re-radiation below sloped PV panels, it has been shown that the presence of the PV panel caused a significant increase in radiative heat flux due to re-radiation from the PV panel compared to identical experiments without PV panels. The same studies also demonstrated that the size of the air gap, the distance between the PV panel and the roof construction, can influence the spread of the fire. In this study, medium and full-scale experiments have been conducted with a fixed distance between the PV module and the roof construction. The roof construction was inclined 30° with PV panels mounted parallel on the exterior surface. Efforts have been made to replicate these experiments through Computational Fluid Dynamic (CFD) Modelling, utilizing thermogravimetric analysis of the specific roofing and cone calorimetry of wood cribs to ensure that the input (and consequently the output) of the model closely approximates the experimental results as possible.

The schematic representation of heat transfer mechanisms involved in flame spread of a freely burning flame on a horizontal solid surface (Figure 4 a) was modified to include the re-radiation from a PV panel as shown in Figure 4 b). The introduction of the PV panel results in re-radiation Q_E from the panel itself, in addition to the flame and accumulated smoke- and combustion gases being forced downward towards the substrate. Here, a distinction is made between the radiation from the hot gas layer underneath the PV module and convection if the layer of hot gas reaches down to the roof surface. As long as there is a layer of cold air/ambient air near the roof surface, convection has no or little effect, but as soon as the distance between the PV module and the roof surface becomes short enough that the hot gas reaches all the way down to the roof, the rate of flame spread will increase. This, in turn, leads to a greater extent of pre-heating of the virgin fuel ahead of the flame front, causing an increase in the rate of flame spread.

Counter-current flame spread, spread opposing the induced flow of air, is typical for horizontal flame spread because the flame induces unheated air along the surface in the direction against the spread of flame. When a flame is spreading upwards on an inclined surface the angle between the flame and the surface is reduced with an increase of the angle of inclination where the natural buoyancy of the flame generates concurrent spread (flame spread in the direction of the mean flow due to wind or buoyancy). The difference between counter-current and concurrent flame spread is shown in Figure 5 a) and b). The change between counter-current and concurrent flame spread occurs generally at an inclination of 15–30°, depending on the width, side confinements, PV modules and other conditions; inclination of roofs are generally within the range where concurrent flame spread is anticipated [37].

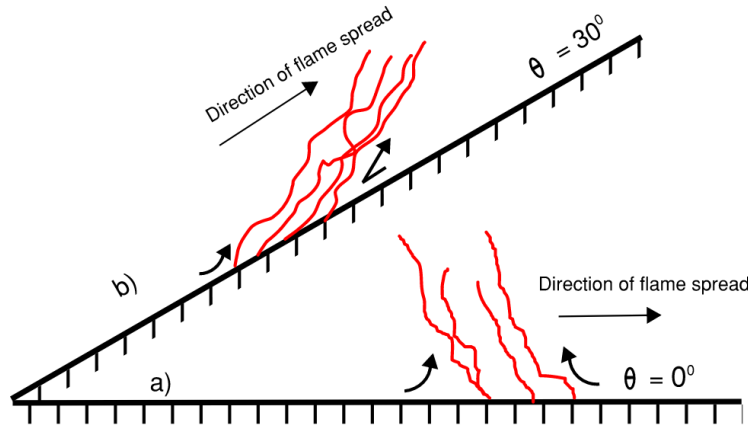


Figure 5: Illustration of change of the mode of surface flame spread according to the slope angle. a) shows counter-current flame spread, b) shows concurrent flame spread.

Research on wildfires has shown that the topography of the land has a profound effect on the spread of a wildfire, as the fire spreads more rapidly uphill than if the spread occurs horizontally. Morandini et al. [38] have conducted experiments showing that the rate of spread up a slope of 10° was about 25% greater than on the horizontal. Studies by Woodburn and Drysdale [39] using CFD also identified a critical angle of 10°. The inclination greatly enhanced rates of flame spread as the flame and hot gases rise in the same direction, filling the boundary layer and creating high rates of heat transfer (the radiation from the flame could ultimately account for more than 75% of the total heat transfer ahead of the pyrolysis front [40]) ahead of the burning zone. The length of the flame becomes a critical factor as it defines the length of the heating zone [41].

With Eq. 4, Williams [31] proposed a rough characterization of radiative heat transfer in horizontal flame spread:

$$q_f = \epsilon_f \sigma_b T_f^4 L_f \sin \theta_f / \delta \quad \text{Eq. 4}$$

Where

q_f	Radiation heat transfer in horizontal flame spread	[W/m ²]
ϵ_f	Emissivity	[-]
σ_b	Stefen-Boltzmann constant	[W/(m ² K ⁴)]
T_f	Flame temperature	[°C]
L_f	Flame height	[m]
θ_f	Average angle with respect to fuel surface	[-]
δ	Thickness of the fuel	[m]

Williams [31] equation (Eq. 4) infares that both flame height and the flame's angular orientation has a significant influence on radiative heat transfer in an open burning scenario (Figure 6 a)). Additional imposition of heat transfer mechanisms on the fuel can be observed by introducing a PV panel. The effect can be seen depending on the gap height, H, in relation to the flame height, as shown in Figure 6 b) and c).

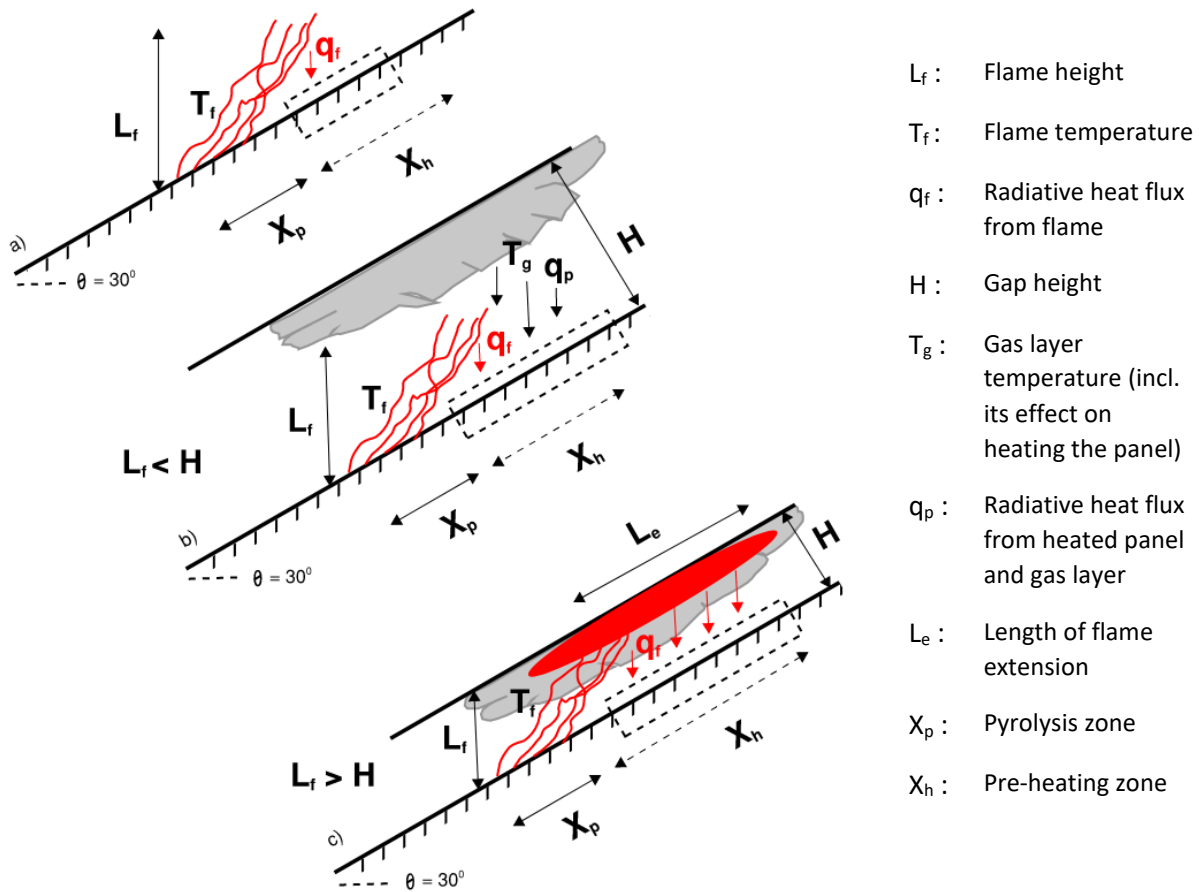


Figure 6: Impact of flame height and the flame's angular orientation of a) open burning, b) $L_f < H$ and c) $L_f > H$. Scenario b) and c) is under influence of a PV panel with different gap height.

In scenario b) where $L_f < H$, the flame spread will be influenced by the amount of re-radiation from the PV panel itself and the formation of a ceiling jet ("relatively rapid gas flow in a shallow layer beneath the ceiling surface that is driven by the buoyancy of the hot combustion products from the plume" [42], p. 429) of accumulated smoke and combustion gases. Buoyancy forces and inclination cause the ceiling jet to primarily move upward along the PV panel, where the gas layer heats up the PV panel by convection and radiation, in addition to direct radiation from the flames. The heating results in re-radiation from the PV panel back to the pre-heating zone of the unburnt surface. The angular orientation of the setup leads to a larger pre-heating zone compared to a horizontal setup, as shown in Figure 4.

In scenario c) where $L_f > H$ the flame height surpasses the gap height, and the flame impinges upon the PV panel. Consequently, the flame is deflected underneath the angular orientated PV panel, becoming a component of the ceiling jet beneath the panel, which in turn leads to a higher view factor between the flame and the fuel surface. In addition, the flame also radiates more heat compared to the gas layer and the heated panel due to the inherent high flame temperatures, which in turn leads to an extended pre-heating zone. This corresponds with findings by Stølen et al. [3] who conducted small-scale experiments on an inclined roof construction with PV panels mounted parallel to the construction; temperature measurements in the roof construction was highest for 6 and 9 cm gap height, there was a small

difference in measured temperature within 12 and 15 cm gap height, while the lowest temperature was measured in experiments without a PV panel. The burning rate is intensified by the thermal feedback through the hot gas/flame layer and the heated panel itself. An illustration of factors determining rate of burning is shown in Figure 7.

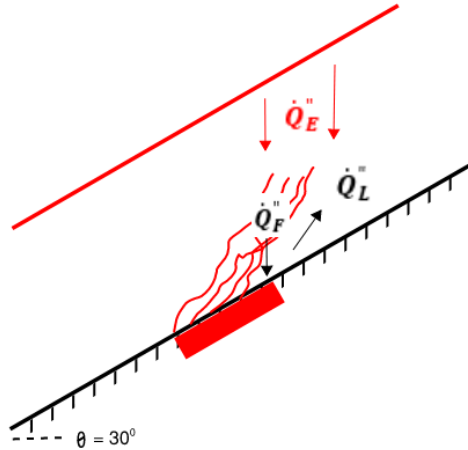


Figure 7: Illustration of factors determining rate of burning.

The following equation presents the rate of burning with the effect of the PV panel as an external heat flux imposed on the burning area [43]:

$$\dot{m}'' = \frac{\dot{Q}_F'' + \dot{Q}_E'' - \dot{Q}_L''}{L_v} \quad \text{Eq. 5}$$

Where

\dot{m}''	Rate of burning expressed as a mass flux	[kg/m ² s]
\dot{Q}_F''	Heat transferred back to the fuel surface from the flames	[kW/m ²]
\dot{Q}_E''	External heat flux imposed on the surface	[kW/m ²]
\dot{Q}_L''	Heat losses as a heat flux from the surface	[kW/m ²]
L_v	Effective heat of vaporisation of the fuel	[kJ/kg]

The rate of burning contributes to the heat release rate through the following equation [44]:

$$\dot{Q} = \chi \dot{m} \Delta H_c = \chi \dot{m}'' A \Delta H_c \quad \text{Eq. 6}$$

Where

Q	Rate of heat release	[kW]
χ	Combustion efficiency	[-]
\dot{m}''	Mass loss rate of the fuel	[kg/sec]
A	Surface area of the fuel	[m ²]
ΔH_c	Heat of combustion of the fuel	[kJ/kg]

The surface area of the fuel in addition to the mass burning rate contributes to the rate of heat release. Thomas [45] argues that the increase in the area of burning have more influence on the rate of fire development than the increase of the rate of burning. This effect will not be investigated any further in this thesis.

2.2 Thermogravimetric analysis

Thermogravimetry, a subfield of thermal analysis, investigates the mass variation of a substance as a function of time or temperature during controlled heating or cooling processes. The weight change profile is recorded in either isothermal or scanning modes. The core principle of thermogravimetric analysis (TGA) involves examining a sample's mass change under predefined conditions, making it ideal for studying thermal phenomena such as absorption, adsorption, desorption, vaporization, sublimation, decomposition, oxidation, and reduction [46]. TGA data is frequently used for various determinations, including identifying polymers/materials in composite materials, studying polymer decomposition, generating evolved products, determining kinetic data, quantifying thermal stability, determining low volatile content, quantifying single polymer components, determining filler content, and assessing oxidative stability [47].

The optimization of factors influencing mass change during experiments is crucial for studying kinetics. These factors encompass the weight and volume of the analyzed sample, its physical form, the characteristics of the sample holder, the atmosphere in which the analysis is performed, the pressure maintained in the sample chamber, and the heating or cooling rate. Although temperature conditions can induce mass changes in samples, it is essential to recognize that not all thermal alterations affect mass variation, rendering TGA unsuitable for examining the melting and crystallization behavior of samples [46].

Thermogravimetric analysis can be classified into three primary types [46], [47]:

1. Dynamic TGA: In this type of TGA, the sample undergoes continuous heating at a fixed heating rate, resulting in a linear change in sample temperature over time.

2. Isothermal TGA: This type of TGA involves maintaining the sample at a constant temperature for a specific time interval, during which any mass changes occurring in the sample are recorded.
3. Quasistatic TGA: In this TGA method, the sample is heated to a constant weight at each of a series of increasing temperatures.

A cylindrical furnace with a long, constant-temperature zone at its center is used in TGA experiments. Static air is rarely used due to potential uncertainties in composition during a run and the possibility of reverse reactions with vapor-phase effluent. A flowing purge gas is commonly employed, and sometimes vacuum operation is utilized for evolved gas analysis techniques. Crucibles made of platinum, which is inert, can withstand temperatures up to 2042 K, and can be cleaned with strong acid, are preferable [47].

A highly sensitive balance suspends a sample over a precisely controlled furnace, using heating rates between 5-20 K/min to identify broad decomposition stages and slower rates of around 1 K/min to isolate individual events. Sample sizes are typically kept as small as possible, usually around 5-10 mg per run, to minimize bulk effects and avoid thermal gradients within the sample [47].

The thermogravimetric curve is generally represented as a plot of weight change in relation to temperature or time. An example of a typical TG curve is depicted in Figure 8 illustrates the pyrolysis of a specific type of asphalt, which can be divided into three stages: i) From ambient temperature to 250 °C where dW/dT equals 0, an indication of little chemical or physical reactions taking place. ii) From 250-425 °C where dW/dT slowly decreases to a steady value, indicating production of volatiles. iii) From 425-530 where dW/dT changes from a steady value to a maximum and then 0 [48].

The vast majority of chemical reactions, comprising about 95% of them, are composed of multiple steps [49].

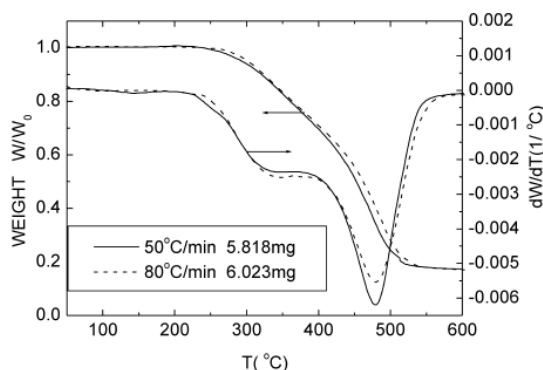


Figure 8: A TG curve of asphalt [48], p. 50.

2.3 Cone calorimetry

Dr. Vytenis Babrauskas developed the cone calorimeter at the National Bureau of Standards (NBS) in the early 1980s, and it is currently the most widely used small-scale calorimeter. The standard test procedure and apparatus are standardized as ASTM E1354 [50] in the United States and as ISO 5660-1 [51] internationally. The standardized cone calorimeter specimens are exposed to an open environment with ample ambient air supply for combustion [52].

The apparatus features a cone heater, spark igniter, specimen holder, and load cell located below the hood. The oxygen consumption method is used to determine heat release rate, and the gas flow rate in the exhaust duct is determined by the pressure drop across and temperature at an orifice plate in the duct. A methane burner calibration is performed to determine the orifice constant. The heater is made up of a 5kW electrical heating element wrapped inside an insulated stainless steel conical shell. The heater can be oriented horizontally or vertically, and maximum radiant heat flux to the specimen exceeds 100kW/m^2 .

The specimen size in both orientations is $0,1\text{m} \times 0,1\text{m}$, and the optional retainer frame in the horizontal orientation and the standard specimen holder in the vertical orientation reduce the exposed area to $0,094\text{m} \times 0,094\text{m}$. An electric spark is utilized as the ignition pilot for vertical specimens and over the center of horizontal specimens. The combustion products and dilution air are extracted through the hood and exhaust duct by a high-temperature fan, and the initial flow rate can be adjusted between 10 and 32L/s .

Most cone calorimeters have instrumentation for measuring light extinction in the exhaust duct using a laser light source, which is described in ASTM E1354 [50] and ISO 5660-2 [53]. Additionally, instrumentation to measure concentrations of soot, carbon dioxide, carbon monoxide, and other gases is commonly included [52].

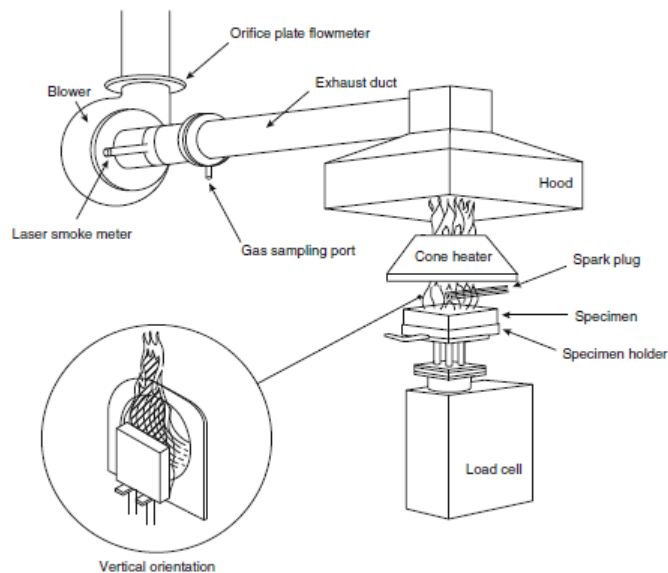


Figure 9: Cone calorimeter. The image is sourced from Marc Janssens in SFPE Handbook [52], p. 926

2.4 Computational Fluid Dynamics Modelling

Computational Fluid Dynamic (CFD) is a versatile tool for analysing a wide range of fluid flow problems, including fire-related ones. Unlike zone models, which are limited to simple fire scenarios, CFD enables the study of complex problems that are difficult to replicate through reduced-scale physical modelling [54].

CFD models employ partial differential equations to conserve mass, momentum, and energy in a fire and its surrounding space. These equations are solved numerically on a three-dimensional mesh of control volumes, providing time-varying predictions of variables like temperature, gas velocity, and gas species concentrations. Direct Numerical Simulations (DNS), which directly solves the governing equations without modifications or models, demands very fine spatial and temporal resolution, making it impractical for large-scale fire simulations. However, due to computational limitations, modifications are needed to model unresolvable turbulence, resulting in large eddy simulation (LES) and Reynolds-averaged Navier-Stokes (RANS) equations [54].

Large eddy simulation (LES) models are derived similarly to Reynolds-averaged Navier-Stokes (RANS) models, with the primary difference being the emphasis on spatial averaging in LES as opposed to temporal averaging in RANS. The eddy viscosity in LES must be small enough to avoid over-smoothing small, resolvable eddies, while still large enough to ensure numerical stability and account for sub-grid scale energy dissipation [54].

The eddy viscosity model in LES is based on the turbulent viscosity coefficient, which includes an empirical constant and a filter length comparable to the size of a grid cell. The diffusive parameters, thermal conductivity, and material diffusivity are related to the eddy viscosity through the turbulent Prandtl and Schmidt numbers, which are assumed constant and of order unity [54].

Uncertainties and complexities arise in modelling turbulent flow, combustion chemistry, radiation, mass, momentum, and heat transfer at solid boundaries, as well as in the numerical solution of the equation set. Despite considerable progress in CFD, challenges remain in addressing complex issues related to combustion and fire science, such as flame spread, oxygen vitiation, soot formation, and water suppression [54].

A variety of fire-specific CFD models have been developed, some catering to specific fire scenarios, while others, such as Fire Dynamics Simulator (FDS), can handle various fire scenarios [54].

Fire Dynamics Simulator (FDS) is a computational fluid dynamics (CFD) model designed to simulate fire-driven fluid flow. It numerically solves a version of the Navier-Stokes equations suitable for low-speed, thermally-driven flow, focusing on smoke and heat transport from fires. It employs a second-order accurate, explicit predictor-corrector scheme, and turbulence is addressed through Large Eddy Simulation (LES) [55]. FDS Solves the following governing equations [56]:

$$\left. \begin{aligned} \frac{\partial \rho}{\partial t} + \nabla \cdot (\rho \mathbf{u}) &= 0 \\ \frac{\partial \rho Y_a}{\partial t} + \nabla \cdot (\rho Y_a \mathbf{u}) &= -\nabla \cdot (\rho \mathcal{D}_a \nabla Y_a + \dot{m}_a''') \\ \frac{\partial \rho \mathbf{u}}{\partial t} + \nabla \cdot (\rho \mathbf{u} \mathbf{u}) &= -\nabla p + \nabla \cdot \mathcal{T} + \mathbf{f} \\ \frac{\partial \rho h}{\partial t} + \nabla \cdot (\rho h \mathbf{u}) &= \frac{Dp}{Dt} + \dot{q}''' - \nabla \cdot \dot{\mathbf{q}}''' + \epsilon \end{aligned} \right\} \text{Eq. 7}$$

Where

ρ	Density
$\dot{\mathbf{q}}'''$	Radiation and conduction heat fluxes
\dot{m}_a'''	Rate of formation per unit volume of a species a
\mathcal{D}_a	Diffusion coefficient of the species a
\mathcal{T}	Tension tensor for the Newtonian fluids
ϵ	Kinetic energy dissipation
h	Sensible enthalpy of the fluid that is a function of the specific heat temperature of the fluid

The equations presented in Eq. 7 form a set of partial differential equations that describe various physical properties of the fluid. These include the density (or component mass fractions), velocity, pressure, and sensible enthalpy. Within this set, the momentum equation comprises three separate equations, each corresponding to one of the three velocity components. Thus, the system consists of five equations in total, addressing six unknowns. To resolve this system and achieve closure, an equation of state is employed [56]:

$$p = \rho RT \sum_a \left(\frac{Y_a}{W_a} \right) \text{Eq. 8}$$

Where

R	Universal gas constant
W_a	Molecular weight of the species a

The combustion model in FDS typically uses a single-step, mixing-controlled chemical reaction with three lumped species. Radiative heat transfer is incorporated via the Finite Volume Method (FVM) for a gray gas, and the absorption coefficients of gas-soot mixtures are calculated using the RadCal narrow-band model. Geometry is approximated on a rectilinear mesh, and FDS can handle multiple meshes for complex computational domains. Parallel processing is achieved through OpenMP and Message Passing

Interface (MPI), and all solid surfaces are assigned thermal boundary conditions and burning behaviour information [55].

The following sub-chapters aim to provide a concise outline of important aspects of the FDS model that are relevant to this study, based on information given in the FDS user's guide [55] and technical reference guide [56].

2.4.1 Combustion model

In FDS, various combustion models are used to calculate the heat release rate per unit volume. This is done by multiplying the mass production rate of a specific species with its heat of formation, as shown in Eq. 9. The default combustion model in FDS is known as the "Single-Step, Mixing-Controlled Combustion" model. In this model, it is assumed that there is instantaneous and complete mixing of lumped species, which are essentially aggregates of individual chemical species. For more complex reactions that involve the formation of carbon monoxide and soot, a more comprehensive approach is essential. The rate at which these chemical reactions occur is heavily influenced by the mixing time in the turbulent combustion. The mixing time is in turn affected by several physical processes including diffusion, advection, and buoyant acceleration. The model accounts for these variables by employing a reaction time scale model, which identifies the fastest process to dictate the flow time scale.

$$\dot{q}''' = - \sum_{\alpha} \dot{m}_{\alpha}''' \Delta h_{f,\alpha} \quad \text{Eq. 9}$$

Where

\dot{q}'''	Heat release rate per unit volume	[kW/m ³]
\dot{m}_{α}'''	Mass production rate of species α	[kg/m ³ s]
$\Delta h_{f,\alpha}$	Heat of formation of species α	[kJ/kg]

Based on user-defined parameters of the type of fuel species, its chemical formula, the yield of carbon monoxide and soot, and the heat of combustion, the default combustion model in FDS automatically generates lumped species categories like AIR, FUEL, and PRODUCTS.

2.4.2 Pyrolysis model

In FDS, two principal pyrolysis models are used to simulate the behaviour of materials exposed to fire: the simple pyrolysis model and the complex pyrolysis model.

Simple Pyrolysis model

The simple pyrolysis model in FDS is typically utilized for forecasting thermal changes and the dispersion of smoke within a designated area caused by a fire. Users can input time-varying heat release rate (HRR)

and link it to a surface. Utilizing this data, FDS calculates the volume of combustible gases entering the domain and initiating combustion. Alternatively, the user can be implementing a time dependent rate at which combustible gases enters the domain by using a burner SURF line applied to a VENT or an obstructions surface.

Once the defined ignition temperature is met, the surface transitions into an active emitter of combustible gaseous fumes. The heat release can be programmed to halt when the mass of the burning surface has been entirely combusted. Implementing this pyrolysis model necessitates the user to estimate a heat release rate for the burning object, data that can be sourced from literature or from conducting fire experiments.

Complex Pyrolysis model

In the investigations conducted for this thesis, a complex pyrolysis modelling is utilized for examining the combustion of solid materials exposed to heat. Due to heat conduction, combustible gases are introduced into the simulation domain through the decomposition of solid materials. Based on the solid's heating and various competing chemical reactions, FDS estimates the amount of flammable gases entering the domain. These reactions might concurrently produce other solid and gaseous by-products like char and water vapor. FDS employs the Arrhenius equation to derive the rate of the chemical reactions, shown in Eq. 10.

$$r_i = \rho_{s,i}^{n_i} A_i \exp\left(-\frac{E_i}{RT_s}\right) \quad \text{Eq. 10}$$

Where

r_i	Reaction rate of the i^{th} component	[-]
A_i	Pre-exponential factor	[-]
E_i	Activation energy	[kJ/mol]
n_i	Reaction order	[-]
R	Universal gas constant	[J/molK]
T_s	Temperature where the reaction occurs	[K]
$\rho_{s,i}$	Density of the i^{th} component of the layer	[kg/m ³]

Be aware that the density of the i^{th} material component in a layer, $\rho_{s,i}$, is calculated by dividing the mass of that component by the volume of the layer. Therefore, $\rho_{s,i}$ will increase when the i^{th} component is generated as a by-product of another reaction, or conversely, it will decrease if the component undergoes decomposition.

The burning rate of a solid material in this model, is driven by user-defined kinetic values, its density, emissivity, absorption coefficient, specific heat capacity among other combustion-related variables. It

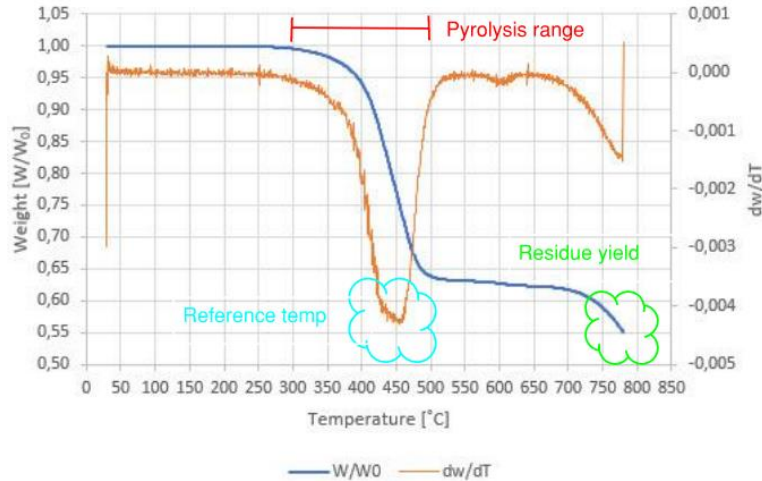
also factors in the temperature of the material throughout the burning progression, as determined by analysing heat conduction within the material. The complex pyrolysis model employs a comprehensive array of data. To acquire such data, researchers utilize specialized analytical tools, such as thermogravimetric analysis (TGA) and cone calorimetry, geared specifically for obtaining insights into the material's thermal characteristics.

Kinetic constants (A and E) are generally not available for most materials. Nevertheless, these materials can still be modelled through a simplified reaction scheme. The fundamental assumption here is that each material component can participate in a maximum of one reaction. Instead of specifying the kinetic constants A and E, FDS allows for the use of alternative parameters to calculate effective values, such as REFERENCE_TEMPERATURE. To better understand the parameter REFERENCE_TEMPERATURE, refer to the graph depicted in Figure 10. These curves represent the TGA experiment conducted at HVL, involving a single-component material (Icopal roofing membrane) undergoing one reaction that transforms the solid into a gas. The Mass Fraction curve (shown in blue) represents the normalized density of the material (Y_s), which decreases as the material is gradually heated, in this example at 10 K/min. The Reaction Rate curve (shown in orange) depicts how the mass fraction changes over time (dY_s/dt). The temperature at which the mass fraction of the material decreases at its maximum rate is what FDS designates as the REFERENCE_TEMPERATURE. The kinetic constants for component i of a multi-component solid are given by Eq. 11:

$$E_{i,1} = \frac{er_{p,i}}{Y_{s,i}(0)} \frac{RT_{p,i}^2}{T} ; A_{i,1} = \frac{er_{p,i}}{Y_{s,i}(0)} e^{E/RT_{p,i}} \quad \text{Eq. 11}$$

Where

$T_{p,i}$	Reference temperature	[°C]
$r_{p,i}/Y_{s,i}(0)$	Reference rate	[s ⁻¹]
$Y_{s,i}(0)$	Mass fraction of the material in the original sample undergoing the reaction. For a single reaction material $Y_{s,i}(0) = 1$	[-]
T	Heating rate which the temperature of the TGA test apparatus was increased	[K/s], [K/min] in FDS



$$\frac{dY_s}{dt} = -AY_s \exp(-E/RT_s) \quad Y_s(0) = 1$$

$$T_p = 450 \text{ }^\circ\text{C}$$

$$r_p \approx -0,0042 \text{ s}^{-1}$$

$$T = 10 \text{ K/min}$$

$$V_s \approx 0,55$$

Figure 10: Results from the TGA experiment conducted on Icopal Topsafe at HVL. The mass fraction W/W_0 of Icopal Topsafe is represented by the blue curve, undergoing heating at 10 K/min. The reaction rate is represented by the orange curve dY_s/dt . The ordinary differential equation that describes the transformation is shown at right. Note that the parameters T_p , r_p , and V_s represent the reference temperature, reaction rate, and residue yield of the single reaction. From these parameters, values of A and E can be estimated using the Eq. 11.

PYROLYSIS_RANGE (ΔT) is an additional parameter that can be used to fine tune the shape of the reaction curve, estimating over what temperature range the reaction takes place. Upon closer examination of the orange curve in Figure 9, the PYROLYSIS_RANGE is estimated from the temperature range of $500 \text{ }^\circ\text{C} - 300 \text{ }^\circ\text{C} = 200 \text{ }^\circ\text{C}$. By using these input parameters, an estimate is made of the peak reaction rate, $r_{p,i}$, with which $E_{i,1}$, then $A_{i,1}$, are calculated using Eq. 12. It's important for the user to choose between using either the kinetic constants A and E or the REFERENCE_TEMPERATURE parameter, but not both simultaneously.

$$\frac{r_{p,i}}{Y_{s,i}(0)} = \frac{2T}{\Delta T} (1 - v_{s,i}) \quad \text{Eq. 12}$$

Where

ΔT	Pyrolysis range	[$^\circ\text{C} / \text{K}$]
$r_{p,i}/Y_{s,i}(0)$	Reference rate	[s^{-1}]
$v_{s,i}$	Yield of solid residue	[-]

2.4.3 Conductive heat transfer

In the context of a room fire, the solid surfaces of the enclosure are exposed to both radiative and convective thermal energy. A fraction of this heat is channelled into the solid material via conductive heat flux. As heat is conducted through a solid surface, consisting of one or multiple layers composed of various materials, the surface may undergo thermal decomposition reactions changing their chemical

composition through the complex pyrolysis model described in the previous chapter. FDS operates on the assumption that conductive heat flows orthogonally to the surface of the solid material, which is mathematically modelled through a one-dimensional heat conduction equation for the solid-phase temperature. Eq. 13 is pertinent for assessing heat conduction into the solid material in a direction orthogonal to its surface.

$$\rho_s c_s \frac{\partial T_s}{\partial t} = \frac{\partial}{\partial x} \left(k_s \frac{\partial T_s}{\partial x} \right) + \dot{q}_{s,c}'' + \dot{q}_{s,r}'' \quad \text{Eq. 13}$$

Where

ρ_s	Density	[kg/m ³]
c_s	Specific heat	[kg/kJK]
T_s	Temperature	[K]
t	Time	[sec]
x	Position	[m]
k_s	Thermal conductivity	[kW/mK]
$\dot{q}_{s,c}''$	Heat loss due to pyrolysis	[kW/m ²]
$\dot{q}_{s,r}''$	Radiative absorption and emission	[kW/m ²]

The assumption of one-dimensionality comes with its own set of limitations, notably the exclusion of radial heat spread or the simultaneous heating of multiple sides of an obstruction. Moreover, there are geometric constraints on the obstruction itself when it comes to heat transfer calculations. In FDS, obstructions are utilized as three-dimensional solid objects that impede flow, serving to represent various elements in a model, such as walls, floors, and ceilings, among other.

The process of constructing an obstruction in FDS is multi-faceted, beginning with the specification of materials. These defined materials are then employed to generate surfaces, which are subsequently integrated into the obstruction itself. Material properties like density, specific heat, and conductivity are pivotal in determining standard heat conduction properties.

2.4.4 Mesh resolution

A mesh is composed of cubic cells, or control volumes, where the mesh resolution is contingent upon how well the flow field is resolved/resolution of the calculation. When establishing the cell dimensions, it's crucial to account for the constraints that larger cell sizes place on the occurrence of turbulence. FDS calculates the average value for each cell, and if the cell division is too coarse, the maximum and minimum values will be underestimated. Therefore, achieving a mesh-independent solution will be necessary to minimize the error source in the numerical solution. Independence can be achieved by starting with a relatively coarse mesh and gradually refining the mesh until it is no significant differences

in the results, also known as a mesh sensitivity analysis. To save computing time, it may be necessary to allow some variation in the mesh grid cell size in the model as there will be the greatest need for a fine resolution near the fire. As a first estimate for validation of simulations involving buoyant plumes, FDS user guide refers to the non-dimensional expression $D^*/\delta x$, where D^* is a characteristic fire diameter and δx is the nominal size of a mesh cell. D^* is defined as:

$$D^* = \left(\frac{\dot{Q}}{\rho_\infty C_p T_\infty \sqrt{g}} \right)^{\frac{2}{5}} \quad \text{Eq. 14}$$

Where

D^*	Characteristic fire diameter	[-]
\dot{Q}	Total heat release rate of the fire	[kW]
ρ_∞	Ambient air density	[kg/m ³]
C_p	Specific heat capacity of air at constant pressure	[J/kgK]
T_∞	Ambient temperature	[K]
g	Gravitational acceleration	[m/s ²]

2.4.5 Orientation

In FDS's default configuration, the force of gravity is oriented in the negative z-axis direction. To modify this and model a sloping roof, the gravity vector can be redefined by using the MISC line. The user inputs a numerical triplet in the form of GVEC=0., 0., -9.81 (x, y, z), where the units are in m/s². In this thesis, the aim centres on the study of a sloping roof construction with a 30° incline, wherein the gravitational force is configured as GVEC=-4.905., 0., -8.495709211 in the FDS model. The gravity changes in the model were calculated as follow:

$$\text{x-direction: } \sin(30^\circ) \cdot -9,81 \text{ m/s}^2 = -4,905 \text{ m/s}^2$$

$$\text{z-direction: } \cos(30^\circ) \cdot -9,81 \text{ m/s}^2 = -8,495709211 \text{ m/s}^2$$

$$\text{Control: } \sqrt{(-4,905 \text{ m/s}^2)^2 + (-8,495709211 \text{ m/s}^2)^2} = 9,81 \text{ m/s}^2$$

2.5 Literature review

This chapter offers a concise overview of related research articles that focus on the fire dynamics in the cavity between roof constructions and Building-Applied Photovoltaic (BAPV) panels. Since the study by Stølen et al. [3] constitutes such a significant part of this thesis, it has been decided to reproduce details from large portions of the report. This is to provide the reader with a thorough understanding of the foundation for the chapter regarding Computational Fluid Dynamics (CFD) modelling, which will be further described later in this thesis.

2.5.1 2016: Photovoltaic installations on warehouse buildings – an experimental study of the propagation on fire

Kristensen's [57] study investigates the impact of photovoltaic (PV) arrays on flat roof constructions in case of fire through four full-scale experiments and a parametric analysis. It was found that heat reflection from PV panels significantly increased heat flux, leading to fire spread under the panels. The tested mitigation solutions, consisting of PIR insulation, mineral wool, or mineral wool with alufoil, were not fully effective in preventing fire spread. The addition of alu-foil, however, showed a considerable reduction in heat transfer. The study recommends avoiding flammable plastic supports in PV array mounting systems to minimize fire risks.

2.5.2 2017: Fire-induced re-radiation underneath photovoltaic arrays on flat roofs

Kristensen et al. [24] investigated the impact of fire-induced heat reflection from a gas burner on real PV panels installed on flat roofs. Heat flux measurements were taken at eight points near the gas burner to examine the difference between the heat flux received at the same distance from the gas burner, with and without the influence of an inclined PV panel. Results showed a significant increase in received heat flux due to PV panels, indicating their contribution to fire spread along the roof. The heat flux was higher under the most elevated part of the panel due to flame deflection and non-homogeneous temperature distribution. The study concluded that it is the fire dynamics, not the fire load, that promotes fire spread with inclined PV panels on flat roofs, making the results relevant for any inclined roof covering panel with limited combustibility.

2.5.3 2018: Experimental Study of the Fire Behaviour on Flat Roof Constructions with Multiple Photovoltaic (PV) Panels

Kristensen and Jomaas [34] conducted a series of four full-scale experiments where six real inclined PV panels were installed in the centre of an existing horizontal roof construction with EPS insulation. Two kinds of mitigation layers (PIR and mineral wool) were used to prevent downwards spread of fire to the EPS. The results confirm that it is the changed fire dynamic scenario that is the main cause for fire spread over the membrane, and not the fire load of the panels, the wind or the low critical heat flux of the membrane. The mitigation layers used to protect a subjacent layer of EPS from ignition partially succeeded for both solutions within an hour after ignition. The study shows that the geometry of PV

installations significantly impacts fire propagation, with fire risk being influenced by both the PV panels and existing roof materials. The introduction of PV panels can increase fire probability and overall risk if proper fire mitigation and management solutions are not employed.

2.5.4 2021: Experimental study of flame spread underneath photovoltaic (PV) modules

Kristensen et al. [25] conducted a series of experiments with real PV panels, mock-up PV panels (made of stainless steel), and without PV panels to determine the fire spread in the cavity between a horizontal roof construction with PV panels mounted parallel to the roof surface. The roofing membrane consisted of 2 mm opaque black polymethyl methacrylate (PMMA). The experiments studying flame spread in horizontal gaps of varying heights and sample widths revealed a critical gap distance, below which a low flame spread rate accelerates rapidly. This critical height is influenced by the initial fire size and has significant implications for PV installations. While baseline experiments were consistent with a heat transfer model based on radiative heat transfer, some discrepancies emerged for low gap heights, warranting further investigation. The presence of a critical gap height offers a potential mitigation measure for minimizing flame spread damage in PV installations, which should be considered in conjunction with other design factors. Sustainable flame spread occurred if the gap height was below a critical gap, determined to be 10 cm for the stainless-steel board, and 11cm for the PV modules. No flame spread was observed if the gap height > 12cm. The hot smoke layer influenced the flame spread scenario by increasing the flame spread length due to enclosed smoke-enhanced pre-heating and decreasing the flame spread rate because of reduced effective gap height, which in turn increased the velocity of ambient air entering the fire plume.

2.5.5 2022: Experimental Study of the Fire Dynamics in a Semi-enclosure Formed by Photovoltaic (PV) Installations on Flat Roof Constructions

Kristensen et al. [35] conducted a series of 42 experiments with both real PV panels and mock-up PV panels (made of stainless steel) to determine the fire spread in the cavity between a horizontal roof construction classified B_{ROOF} (t4) and PV panels with variations in gap height and inclination. The study focuses on the importance of materials beneath the roofing membrane in relation to BAPV systems with the considerations of (i) the varying thermal properties of insulation materials that could affect the heating of the roofing membrane, (ii) the need for a mitigation layer in cases where the roof is unfit for a large DC system (e.g. existing buildings), such as those with expanded polystyrene insulation, and (iii) isolating the behaviour of the roofing membrane from subjacent materials to observe the influence of flame retardants in PVC-based membranes without interference from commercial insulation products. For PV panels inclined between 10° and 15° it has been determined that the critical gap height is > 12cm. Critical gap height can be described as the height of the cavity where the effect of re-radiation is too low to sustain or develop a fire. As the tilt increases, the heat flux beneath the highest portion of the panels intensifies. The trapped smoke layer's effect was eliminated when PV modules were inclined, enabling upward buoyancy-driven flow of combustion products and resulting in a faster flame spread rate

compared to horizontal modules. Compliance with standards does not guarantee prevention of flame spread on roofing membranes with the introduction of BAPV.

2.5.6 2022: EBOB - Solar cell installations on buildings. Experimental study of fire spread in cavity behind solar cell modules on pitched roof surfaces.

Stølen et. al. [3] have authored a technical report summarizing the findings from a series of 29 experiments designed at investigating fire propagation in the cavity behind PV panels mounted on inclined roof surfaces. The study encompassed small-, medium-, and full-scale experiments. A consistent feature across all experiments was a roof structure constructed as a typical combustible construction with a bitumen-based roofing material placed on a 22mm chipboard. This construction type has been tested and classified to comply with $B_{\text{ROOF}}(t_2)$, a classification established as a pre-accepted solution for roofing structures in the Norwegian building regulations (with exceptions for du- fourplexes, linked houses and single-family homes that can be constructed with unclassified roofing, provided the distance to adjacent buildings is at least 8,0m) [5]. The roof construction used in the experiments featured a 30° inclination, with externally mounted mock-up PV panels (stainless steel plates) positioned parallel to the roof surface. The author of this master's thesis was an active involved project collaborator in the planning and execution of the medium- and full-scale experiments. Consequently, the experimental setup, conducting of experiments, results, and discussion/conclusion related to the medium- and full-scale experiments will be derived in chapters 3-6 of this thesis.

Material, equipment and experimental setup

The researchers examined the impact of varying gap heights (6, 9, 12, and 15cm) between the PV panel and the roof surface on the fire propagation at two distinct wind speeds (2 and 4m/s). The experiments adhered to the test setup specified by CEN/TS 1187 [4], test method 2 – a standardized procedure employed to evaluate different setup of combination of materials in a roof construction against the $B_{\text{ROOF}}(t_2)$ classification as per EN 13501-5 [58].

The roof construction measured 400 x 1000mm (W x L) and was comprised, from the bottom up, of a 12mm calcium silicate (solely for bracing purposes and not part of the actual test setup), a 22mm chipboard, and a 3,3mm roofing membrane. The roofing membrane employed was Icopal Topsafe 3°, a single-layer membrane with a polyester core impregnated and coated with SBS-asphalt on both sides. The product is covered with slate granules and features a self-adhesive edge. It has been fire tested in accordance with CEN/TS 1187 test 2 [4] and classified as $B_{\text{Roof}}(t_2)$ when laid on 19mm thick chipboard with a density of $680 \pm 50\text{kg/m}^3$ [59]. The chipboard used in the test setup was of the type NS-EN 312 P6: High load-bearing plate for use in dry conditions, with an average density of $680 \pm 20\text{kg/m}^3$ [60]. Figure 11 gives an illustration of the experimental test setup of the 30° inclined roof construction.



Figure 11: Illustration of the experimental setup used for the small-scale experiments with the PV panel positioned 12cm above the roof surface and with a wind speed of 2m/s. The image is sourced from Stølen et al.[3], p. 10.

The mock-up PV panel were made of a 3mm stainless steel plate measuring 350 x 850mm (W x L). Four stainless steel mounting brackets was attached so the gap heights (6, 9, 12 and 15cm) easily could be adjusted. The PV panel was mounted centrally and parallel on the 30° sloping roof construction, with a distance of 15cm from the lower part of the PV panel to the eaves. Figure 12 illustrates the construction of the mock-up PV panel.



Figure 12: Picture of the mock-up PV module used in the small-scale experimental setup. The mounting brackets and thermocouples are attached on top of the plate. The image is sourced from Stølen et al.[3], p. 11

The fire source used in the experiments was a standardized wood crib described as an EN-crib according to test method 2 in CEN/TS [4], consisting of 6 pine sticks with dimensions of 10 x 10 x 100 mm (W x L x H) laid across two sticks, totaling 8 sticks. The crib's overall dimensions were 100 x 100 x 20 mm (W x L x H). The wood cribs were dried for 24 hours at 105 °C in an oven prior to the tests, weighing

approximately 40 g. A propane burner was used to ignite the cribs before being placed on the roofing membrane. Figure 13 gives an illustration of how the EN-crib was constructed.

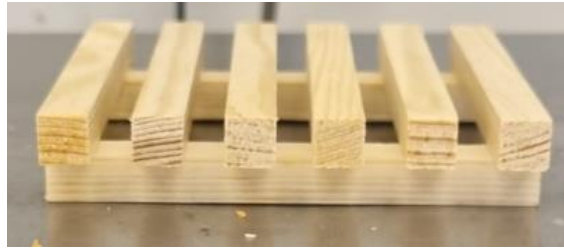


Figure 13: Illustration of the construction of an EN-crib.

Temperatures were measured along the center of the construction; in the three upper layers of the roof construction, as well as on the top of the stainless-steel mock-up PV panel. Type K thermocouples (copper plate IMO) were used under the chipboard, type K thermocouples (twisted) were stapled onto the surface of the chipboard and roofing membrane and spot-welded on top of the PV panel. The thermocouples were connected to a Fluke 2638A Hydra Series III Data Acquisition System/Digital Multimeter for logging. Figure 14 shows a schematic illustration of the instrumentation and test setup for the small-scale experiments.

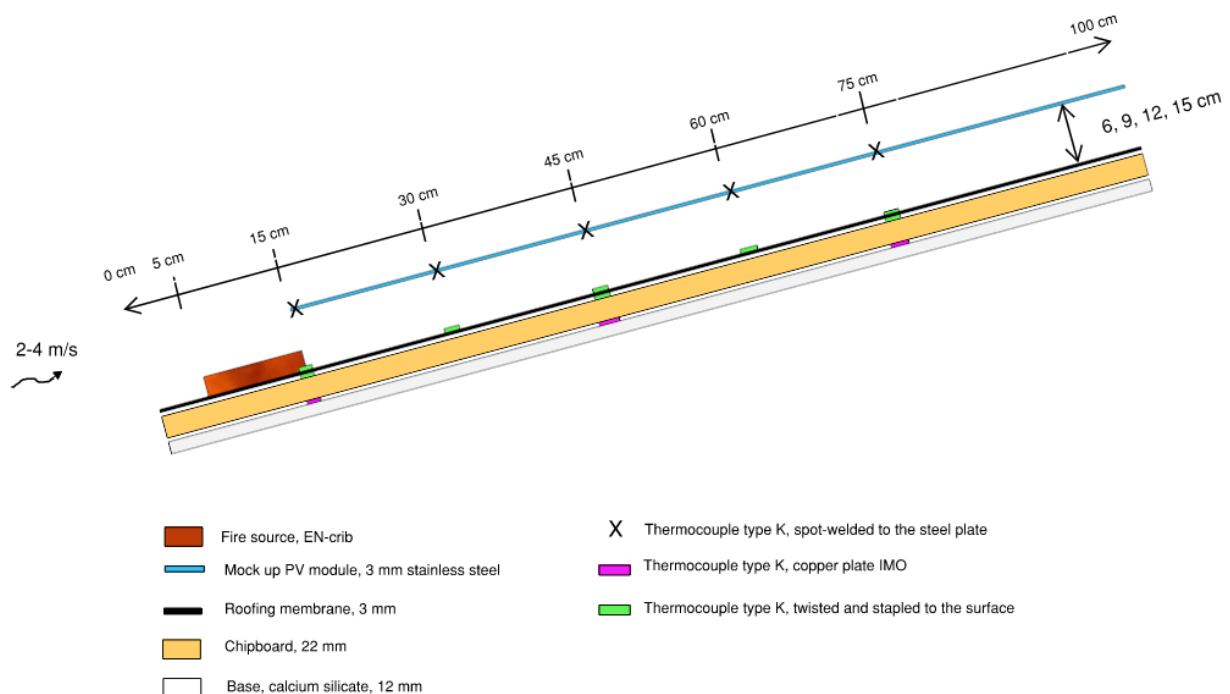


Figure 14: A schematic illustration of the instrumentation and test setup for the small-scale experiments. The figure is a modified reconstruction of an illustration made Stølen et al.[3], p. 11

A total of 21 small-scale experiments were conducted, comprising 1-3 individual tests for each setup, as shown in Table 3.

Table 3: A summary displaying the quantity of individual trails in the various types of setups [3]

Gap height between the roof surface and PV module	Wind speed 2 m/sec	Wind speed 4 m/sec
6 cm	2 experiments	2 experiments
9 cm	2 experiments	2 experiments
12 cm	2 experiments	3 experiments
15 cm	3 experiments	3 experiments
Without PV module	1 experiment	1 experiment

Results and conclusion

The average damage length for the different setups (Table 3), along with the standard deviation, is shown in Figure 15. The black dashed line shows the requirement for classification for $B_{\text{ROOF}}(t_2)$, which is a damage length of $\leq 55,0$ cm for the average of three tests. There is also a requirement that none of the tests should have a damage length $> 80,0$ cm [58]. On average, none of the test setups measured a damage length of > 55 cm, and there were no individual tests with damage lengths ≥ 80 cm. Thus, all the test setups met the requirements for classification $B_{\text{ROOF}}(t_2)$. Of all the tests, the setup with the PV panel mounted 6 cm from the roof surface stood out as having the longest damage length.

It must be mentioned that for the experiment to be valid according to CEN/TS 1187 test 2 [4], it is required to conduct the test three times. RISE Fire Research only carried out two experiments with each setup, so there is not quite enough data to be able to say whether the tests are valid or not. For experiments with a 6 cm gap height and 4m/s wind, it is on the limit. If a hypothetical third experiment had exceeded damage length of 55cm, the test would not have been valid. This means that there is about a 50-50 chance that it could have been valid or not. In defense of the study, mounting PV modules on the roof in the test setup for CEN/TS 1187 test 2 [4] is not accordance to the standard, so there is a bit of deviation from the standard anyway.

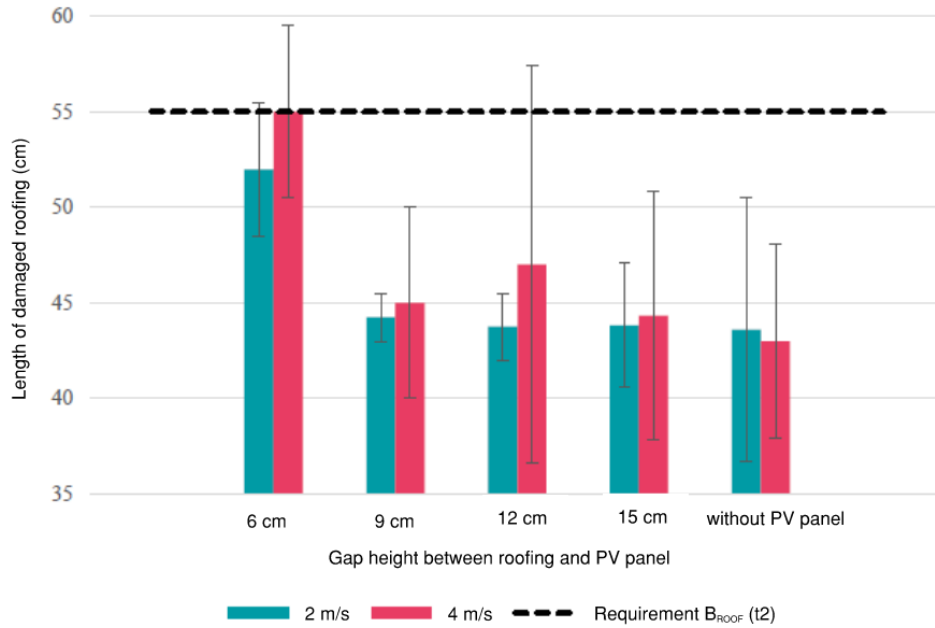


Figure 15: Length of the damaged area of the roof covering after the experiments for different distances between the roof covering and PV panel at two different wind speeds. The black dashed line shows the requirement for classification for $B_{ROOF}(t_2)$, which is $\leq 55,0\text{cm}$ for the average [58]. The image is sourced from Stølen et al.[3], p. 19, where the text is translated to English.

The solid line in Figure 16 shows the average temperatures under the chipboard in various positions for test setups with 6cm gap height between PV panel and the roof surface, with a wind speed of 2m/sec. Dashed lines represent temperatures for corresponding test setups conducted without the PV panel. The largest temperature rise can be observed 150mm from the edge of the roof, where the temperature is also almost identical for experiments with and without the PV panel. In the position 450mm from the edge of the roof, the largest temperature difference between experiments with and without the PV panel can be seen. The measured temperature 750mm from the edge of the roof was low in both experiments in presence and absence of the PV panel.

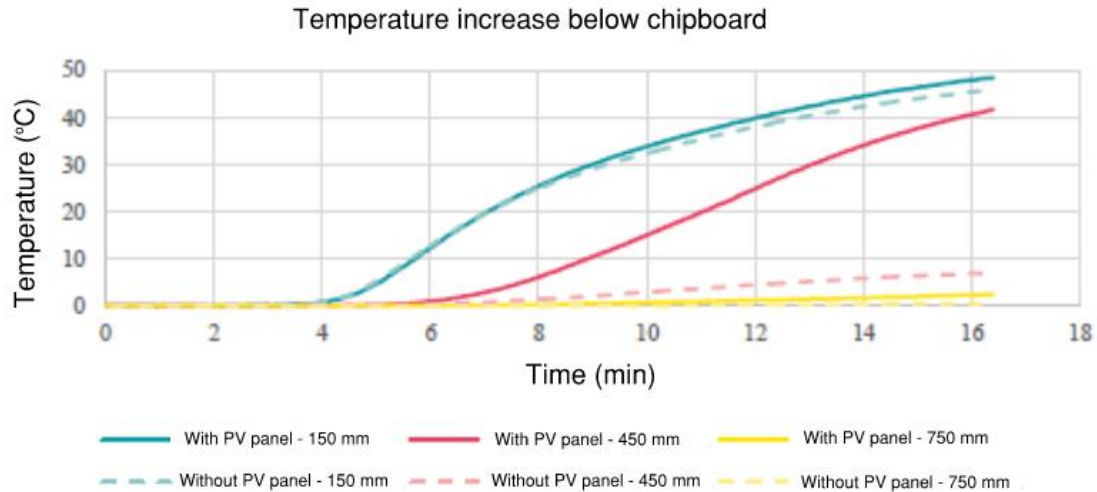


Figure 16: Temperature increase measured below the particleboard for one experiment conducted without a PV panel (dashed lines) and two experiments with a PV panel mounted 6cm above the roof surface (solid lines). The temperatures shown with PV panel is an average of two experiments. The image is sourced from Stølen et al.[3], p. 20, where the text is translated to English.

It was observed that the PV panel contributes to an increased temperature within the roof construction in an area above the fire, and that the temperature increases as the gap height between the PV panel and the roof surface is reduced. The effect of wind in relation to temperature increase was found to be greatest when the wind speed was 2m/sec for a gap height of 6cm, and 4m/sec for a gap height of 9cm. The findings showed a correlation with the measured temperature in the steel of the PV panel, where the highest temperature was measured in the test setup with a gap height of 6 cm and a wind speed of 2m/sec (Figure 17). Wind speed had no impact on the temperature under the chipboard for gap heights > 9cm and test setups without a PV panel.

The experiments showed a significance between the presence and absence of the PV panel, but it was concluded that the difference was not substantial enough to have a significant impact on fire spread during the early stages of a fire. Stølen et al. [3] estimated that the underside of the PV panel generated a radiant flux equivalent to 2,4kW/m² for the highest measured temperature in the steel (200°C). In comparison, Backstrom and Sloan [61] found critical radiant flux values of 14-26kW/m² for various roof coverings classified as “A” according to test method UL 790. Stølen et al. assumed that a real PV panel might contribute to higher heat radiation than the mock-up panel used in these experiments due to the inherent insulating effect of the material composition of the PV panel.

PV panel mounted 6 cm above the roof surface wit 2 m/sec wind

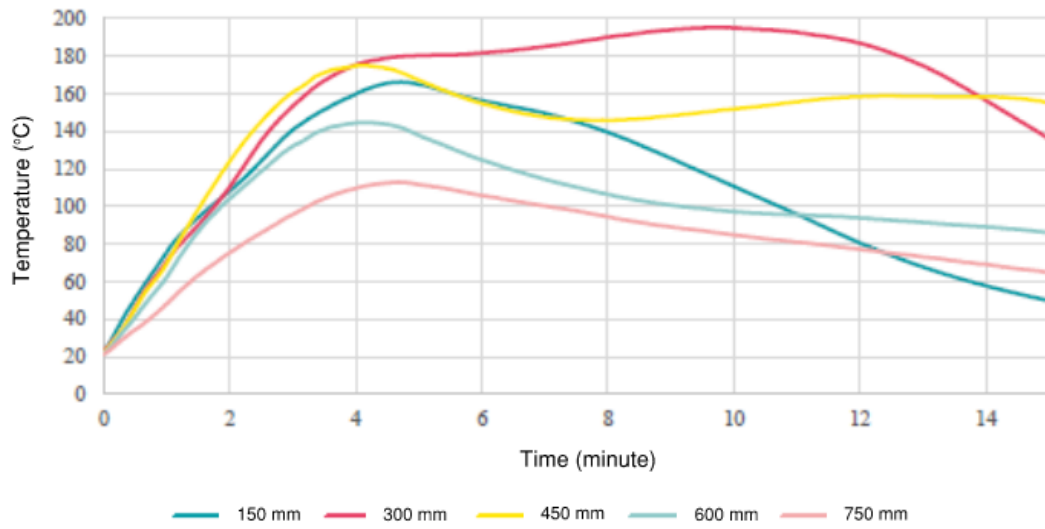


Figure 17: Temperature in the PV panel that was mounted 6 cm above the roof surface. The temperatures are an average of two experiments with 2 m/s wind. The image is sourced from Stølen et al.[3], p. 21, where the text is translated to English.

3. Methodology

This thesis is divided into five parts: I) A series of medium- and full-scale experiments of a sloped roof construction with mock-up PV panels, II) a series of wood crib burning experiments, III) TGA to collect data on the material properties of the roofing membrane used in the experiments, IV) Computational Fluid Dynamics Modelling using FDS to recreate data conducted in the experiments and V) analysis of the results. Figure 18 illustrates the work process used to answer the aim and objectives of this thesis.

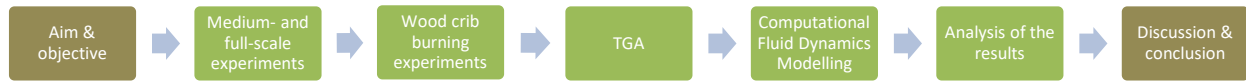


Figure 18: Flowchart illustrating the work process used to answer the aim and objectives of this thesis

Medium- and full-scale experiments

This section will present how the experimental set-up was designed to investigate what effects mock-up BAPV panels has on flame propagation along a 30° inclined roof construction. The motivation behind the medium-scale experiments was to research the size of a standardized initial fire, which could mirror a realistic brand fire, and which entailed fire development and propagation on the roof surface. The medium-scale experiments were carried out with different sizes of initial fire with both the presence and absence of a PV module.

Wood crib burning experiments

This section will present how experiments were conducted on EN-cribs and UL B-cribs to acquire data on HRR and MLR. These types of wooden cribs was used as fire source in both small-, medium- and full-scale experiments. Data from the experiments would subsequently be used in FDS simulations.

TGA

This section will present how TGA was conducted to collect data on the material properties of the roofing membrane used in the small-, medium- and full-scale experiments. Data from the TGA would subsequently be used in FDS simulations.

Computational Fluid Dynamics Modelling

This section will present how computer simulations (FDS) were used to recreate the results from a specific small-scale experimental setup (T4) conducted by Stølen et al. [3].

Analysis of the results

This section will present the results derived from the medium- and full-scale experiments, wood crib burning experiments, TGA experiment and the FDS simulations. The aim of this chapter will be to illustrate what impact building applied photovoltaic (BAPV) panels have on the propagation of fire along a 30° inclined roof construction. FDS simulation could provide further information regarding impact of

wind, gap height between PV modules and the roof construction, how the heat spreads inward into the construction etc.

Discussion and conclusion

The discussion and conclusion will attempt to give answers/indications to the aims and objectives based on the findings in the analyses of the results.

3.1 Experiments conducted in collaboration with RISE Fire Research

In the fall of 2022, a series of six medium-scale experiments and two full-scale experiments were conducted to investigate the impact of mock-up BAPVs on the propagation of fire along a 30° inclined roof construction. The author of this master's thesis was actively involved as a project collaborator in the planning and execution of these experiments, which are part of DSB/DiBK-project. The experiments are a continuation of previously conducted small-scale experiments by Stølen et al. [3], referenced in Chapter 2.5.6. The aim of conducting medium-scale experiments is to determine the smallest size of the fire source that would establish itself in the roof membrane and lead to further spread along the length of a realistic roof construction. The full-scale experiments were conducted to examine the validity of the results from small- and medium-scale setups in comparison to a realistic residential roof covered with BAPVs. All medium- and full-scale experiments were conducted outdoors at the RISE Fire Research test facility in Trondheim, in contrast to the small-scale experiments, which were conducted indoors. Other differences include; I) the dimension of the roof construction, II) the number of mock-up PV modules, III) gap height, and IV) weather and wind conditions.

Small-scale experiments were conducted indoors with forced wind speeds of 2 and 4m/s, while medium- and full-scale experiments were conducted outdoors with varying wind. In small-scale experiments, the effect of different gap heights (6, 9, 12, and 15cm) between the mock-up PV module and roof construction was studied. The choice was made to use a 12cm gap height in medium- and full-scale experiments based on; a 12cm gap height was considered to be a realistic measurement for typical BAPV installations based on a number of internet searches on the dimensions of mounting systems. Additionally, Backstrom et al. [62] have tested various gap heights and concluded that it was the setup with a gap height of 5 inches (approximately 12cm) that resulted in the worst fire scenario. In the medium-scale experiments, a single PV module was utilized, mirroring the approach taken in the small-scale experiments. Conversely, the full-scale experiments employed a total of six PV modules, arranged as three modules in width and two in height. This configuration was chosen to more accurately represent a realistic setup, aligning with the dimensions of the roof construction. Otherwise, the materials used in the roof construction and the PV modules were the same for both small-, medium-, and full-scale experiments.

3.1.1 Material, equipment and experimental set-up

The experiments adhered to the test setup specified by CEN/TS 1187 [4], test method 2 – a standardized procedure employed to evaluate different setup of combination of materials in a roof construction against the B_{ROOF} (t2) classification as per EN 13501-5 [58]. In addition, the American standard for fire testing roof coverings, UL 790 [6], was used as a source for both the positioning of the fire source and the standardization of one size of fire source used in the experiments.

The roof construction was comprised, from the bottom up, of a layer of 12mm OSB (solely for bracing purposes and not part of the actual test setup), a 22mm chipboard, and a 3,3mm roofing membrane. The roofing membrane employed was Icopal Topsafe 3°, a single-layer membrane with a polyester core impregnated and coated with SBS-asphalt on both sides. The product is covered with slate granules and features a self-adhesive edge. It has been fire tested in accordance with CEN/TS 1187 test 2 [4] and classified as B_{Roof} (t2) [59] when laid on 19mm thick chipboard with a density of $680 \pm 50\text{kg/m}^3$. The chipboard used in the test setup was of the type NS-EN 312 P6: High load-bearing plate for use in dry conditions, with an average density of $680 \pm 20\text{kg/m}^3$ [60].

The mock-up PV panel was made of a 2mm stainless steel plate measuring 1000 x 1700mm (W x L). For reinforcement, a 5mm steel frame with dimensions of 40 x 40mm (W x L) was welded on, along with four 3mm steel brackets measuring 120 x 91 x 40mm to set the gap height of 12cm. The PV panel was mounted parallel on the 30° sloping roof construction. UL 790 [6] specifies that the shortest distance from the eaves to the PV panel should be at least 60cm. The choice was made to place the center of the fire source 30cm from the lower part of the PV panel. The goal was then to place the first thermocouple directly above the fire, it then naturally followed that the placement of the next thermocouple would be a corresponding 30cm from the top of the same PV panel, resulting in a distance of 1,1m between the thermocouples on the upper side of the PV panel. Figure 19 gives an illustration of how the PV module was constructed, and the placement of the two spot-welded thermocouples. The underside of the PV panels was sooted with a diesel fire prior to the experiments, so that the emissivity from the PV panels would be as similar as possible in each experiment.

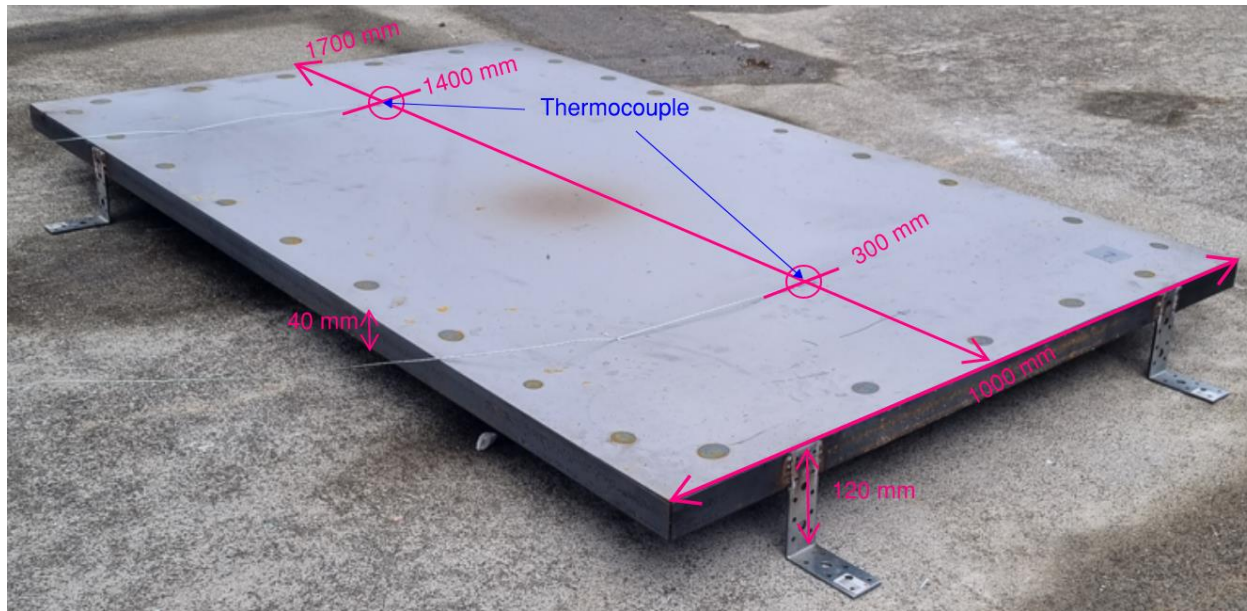


Figure 19: Illustration of how the PV module was constructed, and the placement of the two spot-welded thermocouples

3.1.2 Medium-scale experiments

In the series of six medium-scale experiments, two different standardized wood cribs were used as fire sources: I) The EN-crib described in test method 2 in CEN/TS [4], consisting of 6 pine sticks with dimensions of 10 x 10 x 100mm (W x H x L) laid across two sticks, totaling 8 sticks. The crib's overall dimensions were 100 x 100 x 20mm (W x L x H). II) The UL B-crib (Class B brand) described in the UL 790 [6], composed of 6 spruce sticks with dimensions of 19,1 x 19,1 x 150mm (W x H x L) arranged in three layers where the middle layer is laid perpendicular to the other two layers, totaling 18 sticks. The crib's overall dimensions were 150 x 150 x 57,3mm (W x L x H). Common to both types of wood cribs were that they were dried for 24 hours at 105°C in an oven prior to the tests, then placed in a desiccator for cooling. The EN-crib weighed approximately 40g, and the UL-B crib weighed approximately 500g, after being dried.

The medium-scale experiments were conducted with four different sizes of the initial fire: I) 1 x EN-crib, II) 2 x EN-cribs stacked on top of each other, III) 3 x EN-cribs stacked on top of each other and IV) 1 x UL B-crib (illustrated in Figure 20). The cribs were ignited using a propane burner before being placed on the roofing membrane. Ignition of the EN-crib stopped once the fire had established itself in the crib. The ignition of the UL B-crib was performed in accordance with UL 790 test standard [6], which specifies that the crib should be ignited with a propane burner for 30 seconds against each of the two largest surfaces, then 30 seconds against each of the smaller surfaces, and finally 30 seconds against each of the two largest surfaces again, totaling 4 minutes before the ignited UL B-crib is placed on the roofing membrane.

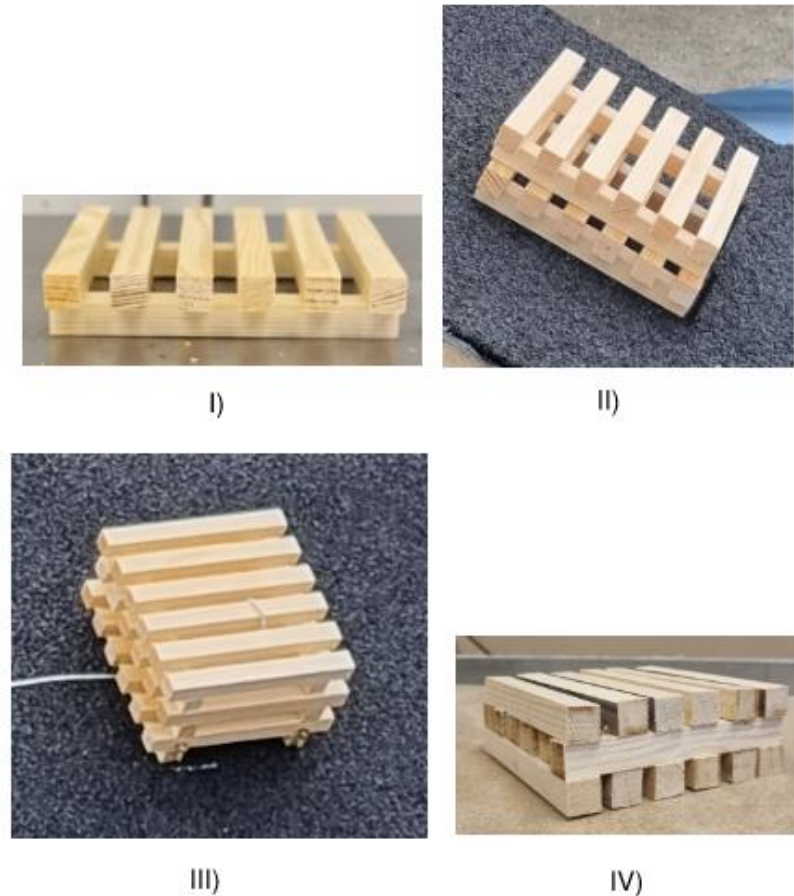


Figure 20: Illustration of the four different sizes of initial fire tested in the medium-scale experiments. I) 1 x EN-crib, II) 2 x EN-cribs stacked on top of each other, III) 3 x EN-cribs stacked on top of each other and IV) 1 x UL B-crib.

The dimensions of the 30° inclined roof construction were 120 x 240cm (W x L) with one PV panel placed in the center, at a distance of 60cm from the lower part of the PV to the eaves. Temperatures were measured along the center of the construction; in the three upper layers of the roof construction, as well as on the top of the stainless-steel mock-up PV panel. Type K thermocouples (copper plate IMO) were used under the chipboard, type K thermocouples (twisted) were stapled onto the surface of the chipboard and roofing membrane and spot-welded on top of the PV panel. The thermocouples were connected to a Fluke 2638A Hydra Series III Data Acquisition System/Digital Multimeter for logging. Figure 21 shows a schematic illustration of the instrumentation and test setup for the medium-scale experiments.

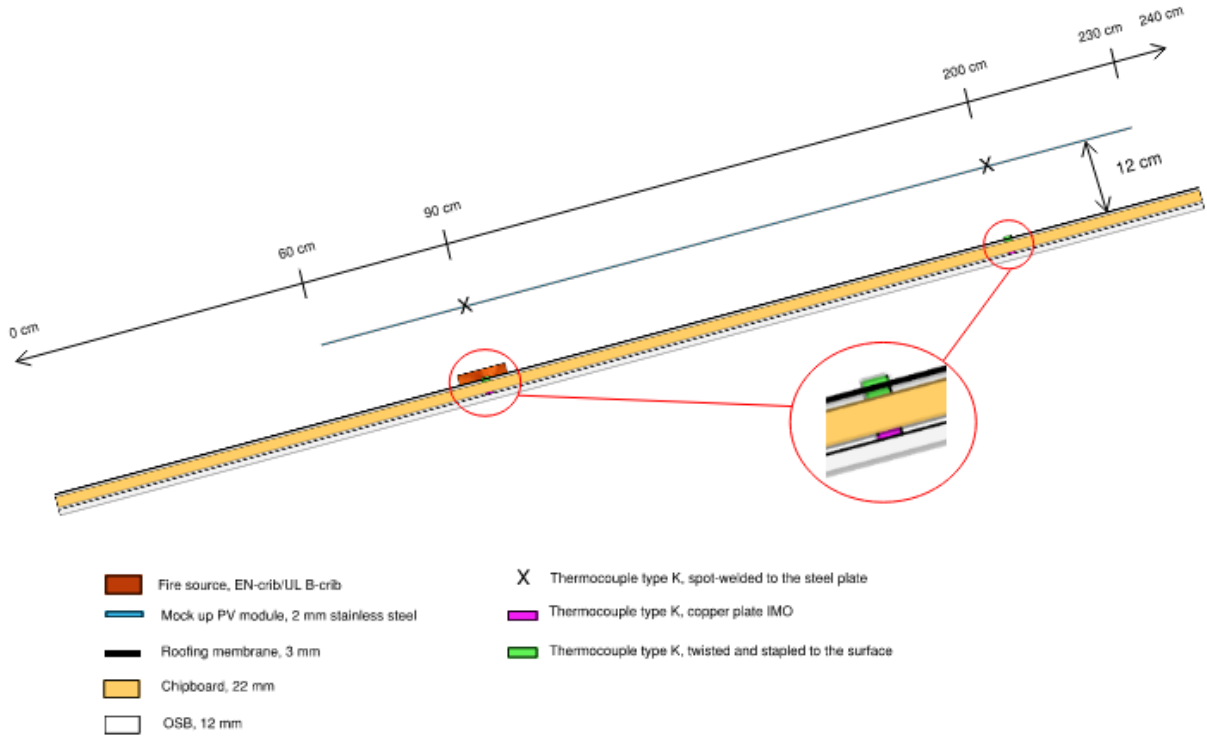


Figure 21: A schematic illustration of the instrumentation and test setup for the medium-scale experiments. The figure is a modified reconstruction of an illustration made by Stølen et al.[3], p. 15

A handheld RS 327-0640 Hot Wire Anemometer was used for wind measurement. At the time the experiments were carried out, the temperature was 14 °C, there was no precipitation, and the wind speed was between 0-1m/s. The test rig was oriented towards the northern direction.

Table 4 gives an overview of both the number and the setup of medium-scale experiments.

Table 4: Overview of the test setup for the six medium-scale experiments

Test ID	Fire source	PV panel
M1	1 x EN-crib	No
M2	2 x EN-crib	No
M3	1 x UL B-crib	No
M4	1 x UL B-crib	Yes
M5	1 x EN-crib	Yes
M6	3 x EN-crib	Yes

Figure 22 shows the test setup used in the medium-scale experiments; I) test M3 without a PV panel and II) test M4 with a PV panel.

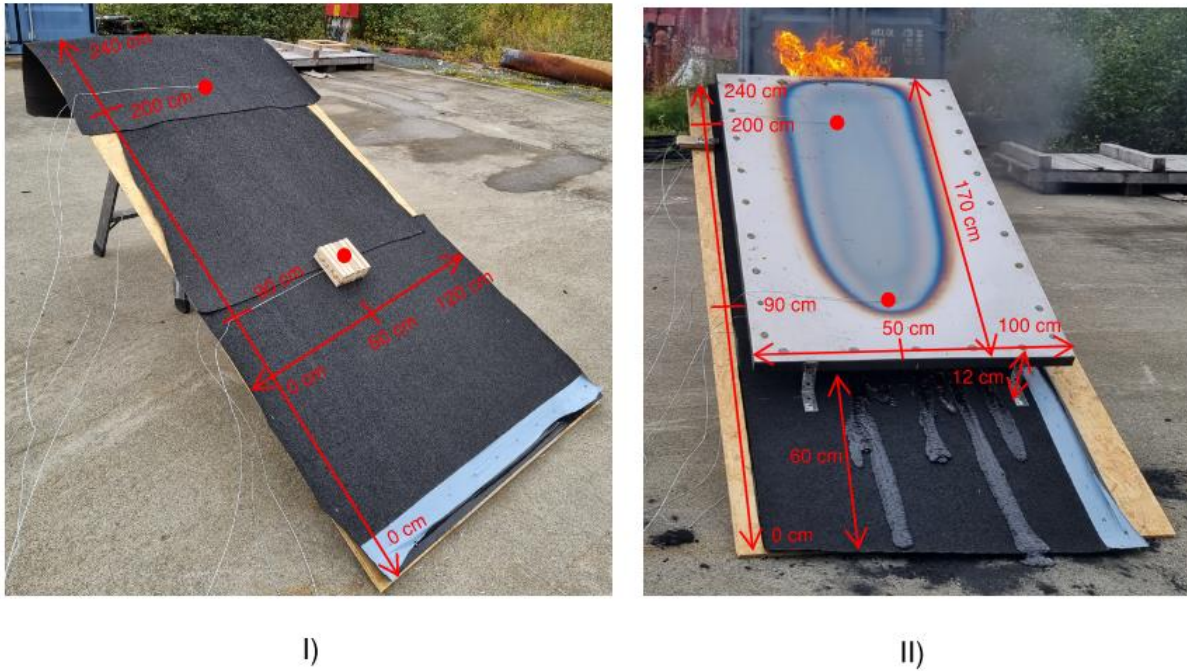


Figure 22: Illustration of the test setup used in the medium-scale experiments; I) test M3 without a PV panel and II) test M4 with a PV panel.

3.1.3 Full-scale experiments

The intention behind conducting full-scale experiments was to assess the validity of the results from the small- and medium-scale setups compared to a realistic residential roof covered with BAPV. Similar to the previous medium-scale experiments, the use of materials and construction of the roof structure were identically executed. The differences from the experiments were the dimension of the test rig itself and the number of PV modules.

The dimensions of the 30° inclined roof construction were 420 x 540cm (W x L) with a total of six PV panels; three PV panels in the row and with two columns. The first row of PV panels was mounted 60cm from the lower part of the PV to the eaves, and the distance between each PV panel was 4cm. The test setup is illustrated in Figure 23.

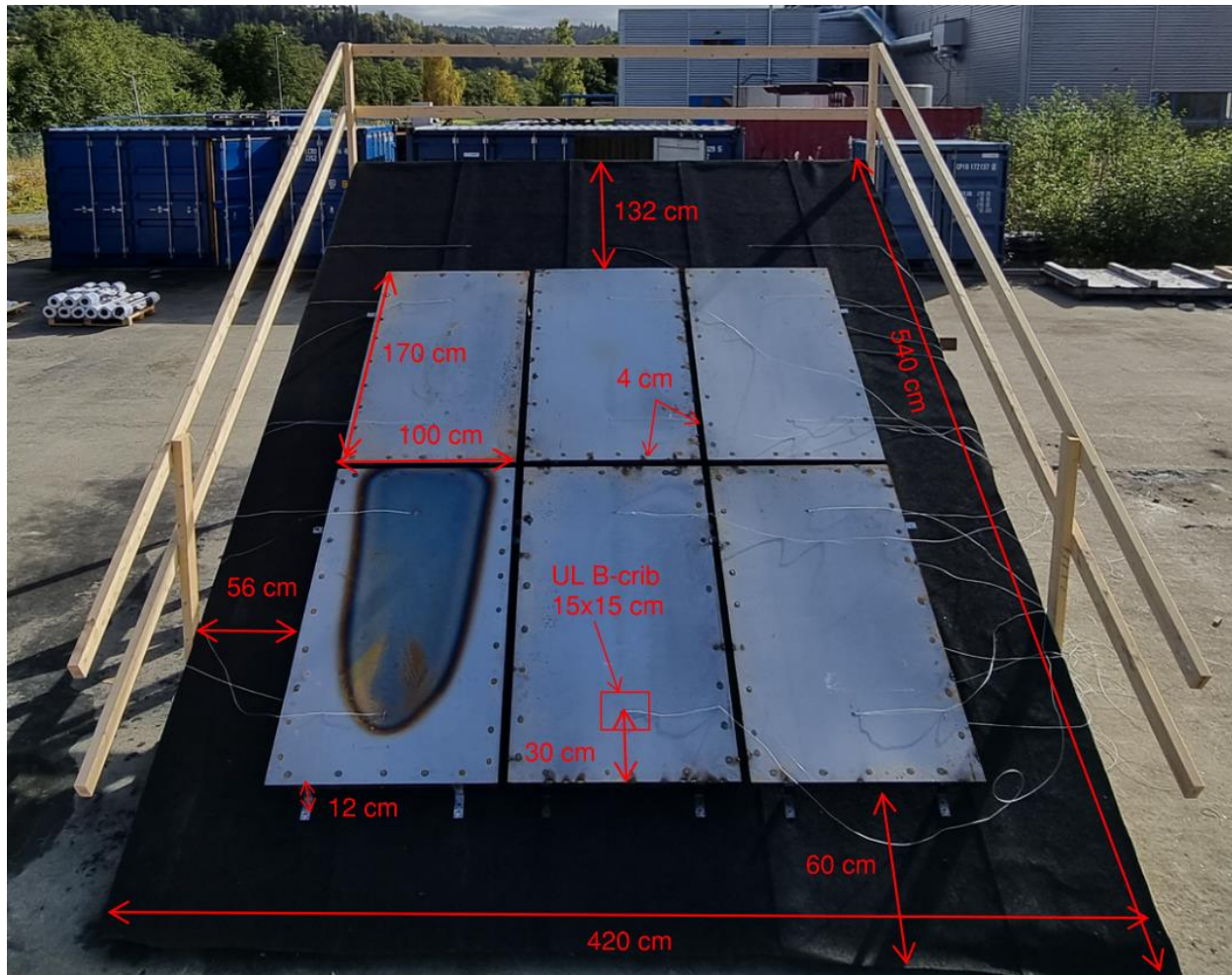


Figure 23: Illustration of the dimensioned test setup for the full-scale experiment.

The experience from testing different crib sizes in the medium-scale experiments indicated that the EN-crib, even when stacked in three heights, did not produce enough heat for a fire to establish and spread upward in the roof structure. Therefore, the choice fell on the UL B-crib as the fire source, as the experiment with the PV module produced flames that protruded outside of the rooftop. The ignition procedure of the UL B-crib was the same as in the medium-scale experiment. The ignited crib was placed under the middle PV panel on the bottom row, at a distance of 30cm from the bottom of the PV panel to the center of the wooden crib.

From the experiments conducted in medium-scale, it was observed that flame spread mostly occurred along the vertical axis, and little horizontally. For that reason, a slightly different setup was chosen for the instrumentation of the full-scale experiment. Temperatures were measured along the center of the PV modules. For the middle column of PV modules where the fire source is located, temperatures were measured in the three upper layers of the roof construction, as well as on the top of the stainless-steel mock-up PV panel. For the two outermost columns of PV modules, temperatures were measured on top

of the roofing membrane, as well as on the top of the PV panel. Type K thermocouples (copper plate IMO) were used under the chipboard, type K thermocouples (twisted) were stapled onto the surface of the chipboard and roofing membrane and spot-welded on top of the PV panel. The thermocouples were connected to a Fluke 2638A Hydra Series III Data Acquisition System/Digital Multimeter for logging. Figure 24 and Figure 25 shows the instrumentation for the test setup in the full-scale experiment.

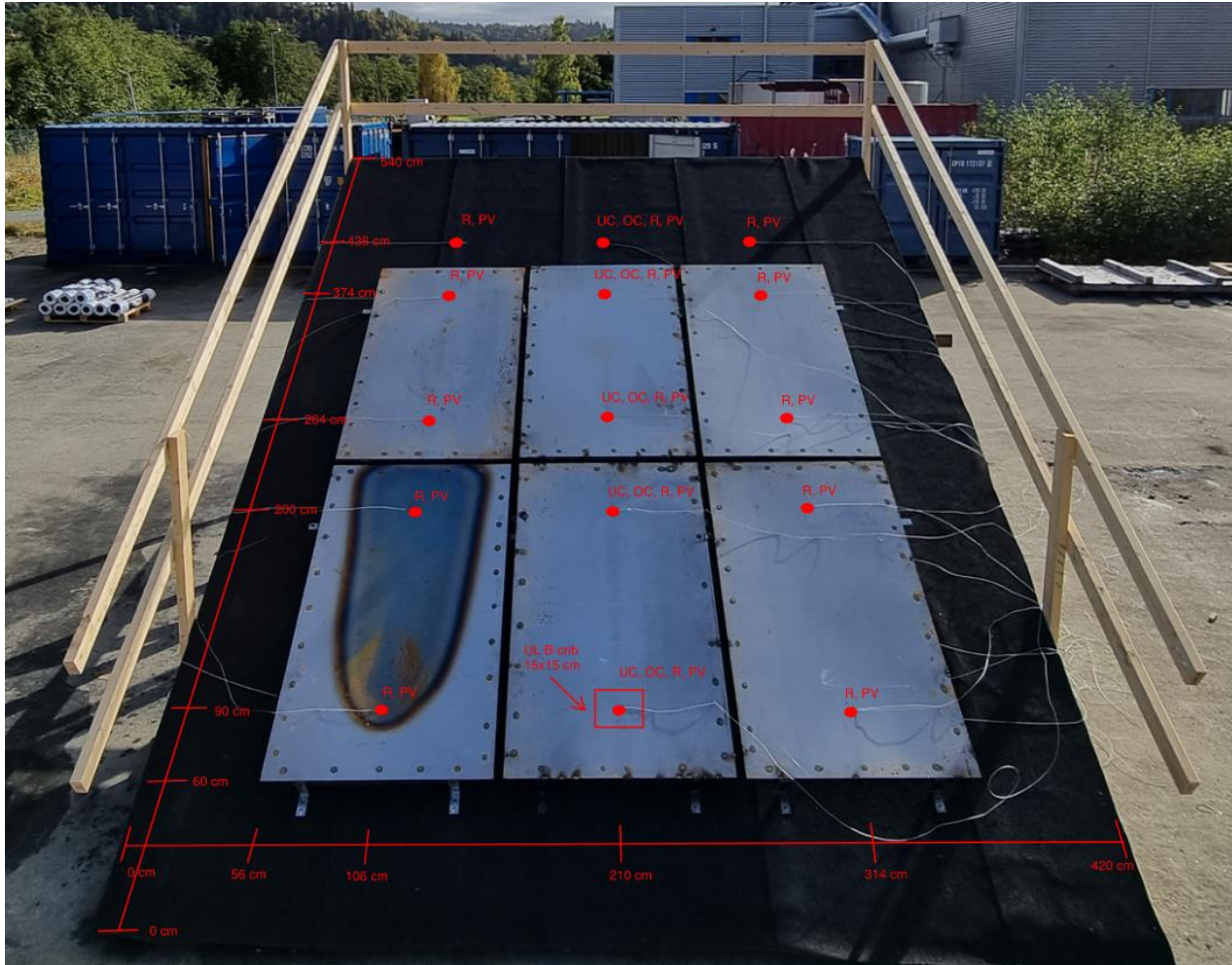


Figure 24: Illustration showing the instrumentation for the test setup in the full-scale experiment. In the middle column of PV modules, where the initial fire is located, temperatures were measured in three layers of the roof construction as well as on the top of the stainless-steel mock-up PV panel. The codes UC, OC, R, and PV indicate which layer of the roof construction the thermocouple was placed: UC – under chipboard, OC – over chipboard, R – roofing membrane, PV – on top of the PV module. For the two outermost columns of PV modules, temperatures were measured on top of the roofing membrane, as well as on the top of the PV panel.

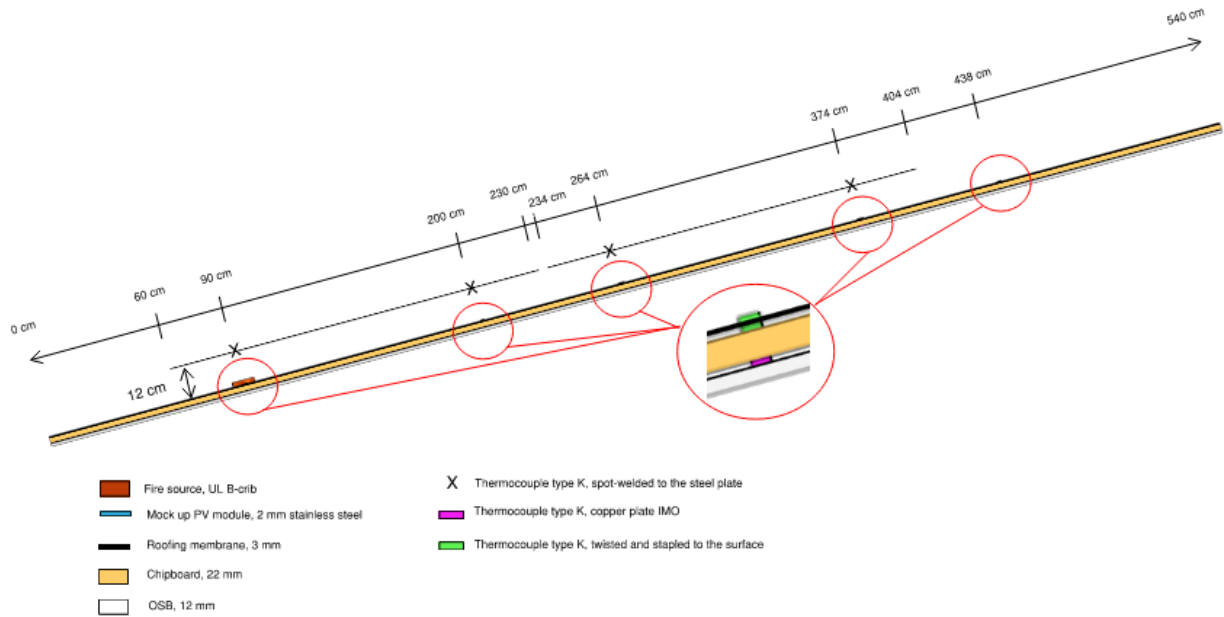


Figure 25: Section view of the center of the roof construction where the initial fire is located. The figure is a schematic illustration of the instrumentation and test setup for the full-scale experiment.

The experiment was conducted outdoors, where both a Netatmo measurement station connected to a local weather station at RISE and a handheld RS 327-0640 Hot Wire Anemometer were used for wind measurements. During the experiment, the temperature was 13°C, with no precipitation and wind speeds of 0-1m/s coming from the northwest. The test rig in the full-scale experiment was oriented toward the northern direction.

In the second full-scale experiment, a steel gutter was installed at the eaves of the roof to investigate whether accumulated melted roofing material contributes to greater fire spread in the lower part of the roof construction. Additionally, the dimensions in the upper part of the roof construction were increased by 1,3m in width and 1m in length at the center of the construction to examine how far the fire spread, measured from the top row of PV panels. The changes to the test setup in experiment 2 can be seen in Figure 26.

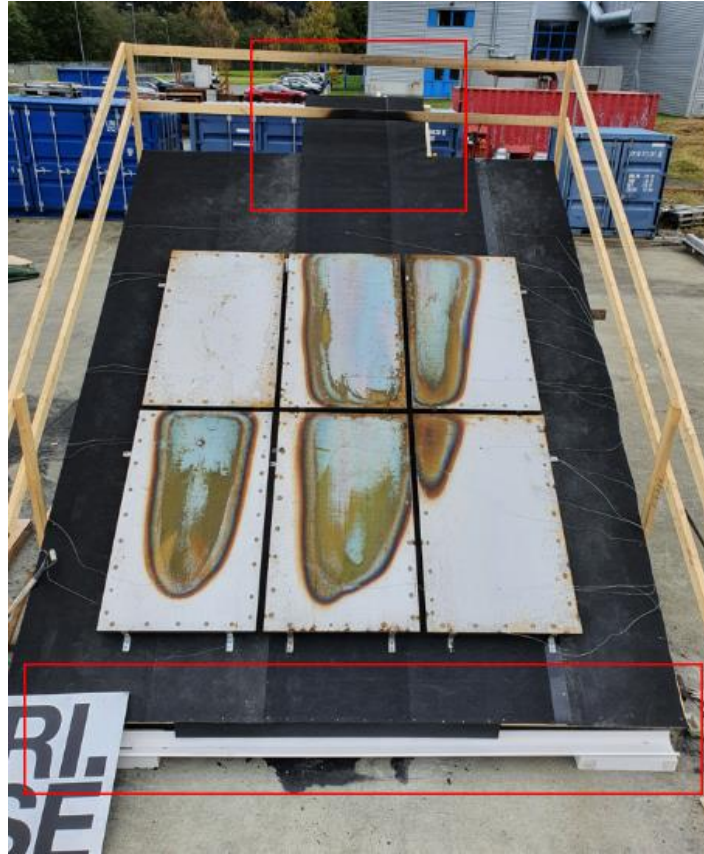


Figure 26: Illustration showing the changes from the test setup in experiment F1 to experiment F2; a steel gutter was installed at the eaves to collect melted roofing membrane, and the middle part of the roof construction was extended by 1 m in length and 1,3 m in width.

3.2 Wood crib burning experiments

As part of further research, fire tests were conducted on the wooden cribs used as the fire source in both small-, medium- and full-scale experiments. The rationale for these experiments was to acquire data on the Heat Release Rate (HRR) and Mass loss rate (MLR) for both the EN-crib and the UL B-crib, which would subsequently be used in FDS simulations. In the study of the EN-crib, cone calorimeter were used. Both the mass and dimensions of the UL B-crib were too large to be accommodated by the cone calorimeter apparatus; therefore, four free-burning tests in a well-ventilated indoor lab were conducted instead. This type of test setup proved to be the closest approximation to the experiments conducted in Trondheim.

3.2.1 Cone calorimeter

A series of three EN-cribs were tested using the cone calorimeter in accordance with ISO 5660 test method [51] and instrumentation according to ASTM E1354 [50]. The aim of the tests was to investigate experimental data for the HRR of the fire source used in the small- and medium-scale experiments in Trondheim, which will further be used as input to make the FDS model more accurate. Prior to the

experiments, the cribs were dried for 24 hours in a drying cabinet at 105°C. The apparatus used in the experiments was Netzsch TCC 918. Before the experiments were initiated, a 60-point checklist was carried out to calibrate the cone calorimeter and thus ensure the reliability of the results. The main elements in the checklist were gas analysis, weighing accuracy, C-calibration, and experimental procedure. The specimens were placed directly in the sample pan without a retainer frame. With this setup, the wooden cribs had free access to oxygen from all sides except from the underside, similar to the experiments with the roof constructions. Differences in the test setup for the cone calorimeter compared to the experiments in Trondheim is that i) the burning crib is placed on a horizontal surface in the cone calorimeter, whereas in Trondheim, the crib was placed on a 30° inclined structure, ii) and the crib received 15kW/m² radiation from the cone throughout the entire experiment. Figure 27 is an illustration of the test setup used for the burning of EN-cribs in the cone calorimeter.

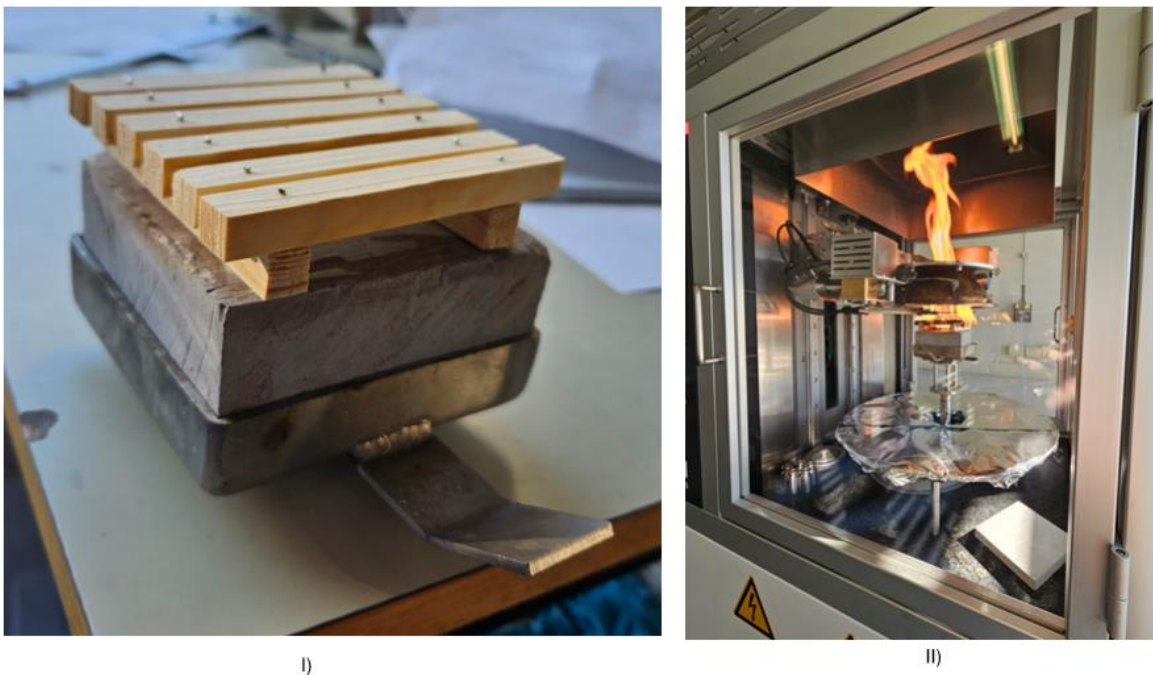


Figure 27: Illustration of the test setup used for the burning of EN-cribs in the cone calorimeter; I) Illustration of how the wooden crib was placed directly in the sample pan without a retainer frame. II) Picture showing a burning EN-crib in the cone calorimeter.

The cone calorimeter experiments were conducted indoors at the fire lab of Western Norway University of Applied Sciences, supervised by Anita Katharina Meyer, Staff engineer at Department of Safety, Chemistry and Biomedical laboratory sciences. All tests were conducted with the samples exposed to a heater with a heat flux of 15kW/m². Table 5 provides an overview of the test setup for the cone calorimeter experiments.

Table 5: Overview of the test setup for the cone calorimeter experiments.

Test ID	Fire source	Ventilation	Initial mass	Time to ignition	Test duration
CC1	1 x EN-crib	Without retainer frame	50,40 g	30 sec	10 min
CC2	1 x EN-crib	Without retainer frame	51,24 g	30 sec	10 min
CC3	1 x EN-crib	Without retainer frame	50,28 g	30 sec	10 min

3.2.2 Free burning

A series of four UL B-cribs were burned in a well-ventilated indoor environment. Prior to the experiments, the cribs were dried for 24 and 46 hours in a drying cabinet at 105°C. The ignition of the UL B-cribs was performed in the same manner as in the experiments conducted in Trondheim. After ignition, the burning cribs were placed on a non-flammable surface on a tared Kern D5 scale connected to a KEYSIGHT 34972A LXI Data Acquisition/Switch Unit data logger and a PC. The LabVIEW software was used to log time versus the weight loss of the burning cribs. Tests 1-3 were conducted by placing the burning wooden cribs on a solid surface, in contrast to test 4 where the wooden crib was placed on a metal grate with a 5cm gap height to a solid surface, allowing free access to oxygen from the underside as well. The test setups are illustrated in Figure 28. The rate of combustion of cribs under well-ventilated conditions is dictated by two primary factors: i) the size of the opening between the sticks, or ii) the dimensions and mass of the sticks themselves. An increased opening size results in an accelerated combustion rate, predominantly governed by the dimensions and mass of the sticks involved in the process [63].

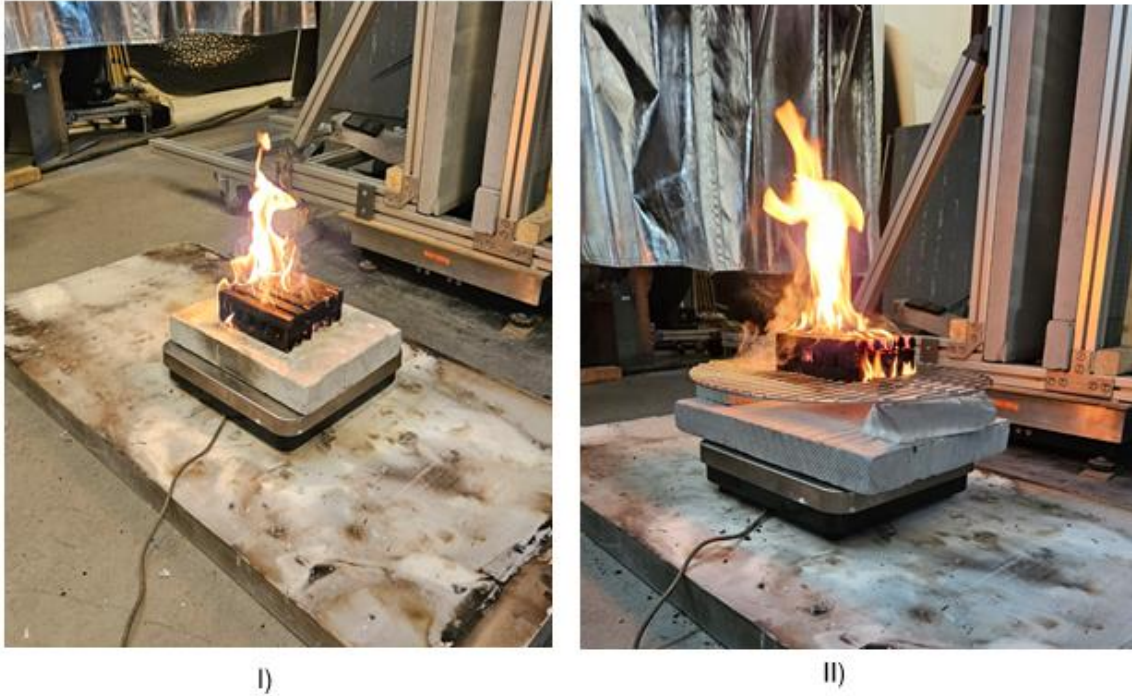


Figure 28: Illustration of the test setup for free burning of UL B-cribs; I) test setup for experiments 1-3 with cribs placed on a solid surface II) test setup for experiment 4 with crib placed on a metal grate with a 5 cm gap height to a solid surface

The experiments were conducted indoors at the fire lab of Western Norway University of Applied Sciences, supervised by Anita Katharina Meyer, Staff engineer at Department of Safety, Chemistry and Biomedical laboratory sciences. Table 6 provides an overview of the different test setups for the free burning wood crib experiments. By accident, the cribs for experiments FB3 and FB4 were dried for approximately 22 hours longer than for experiments FB1 and FB2.

Table 6: Overview of the test setup for the free burning wood crib experiments

Test ID	Fire source	Ventilation	Time spent for drying
FB1	1 x UL B-crib	Crib placed on a solid surface. Well-ventilated on 5 of 6 sides	24 hours
FB2	1 x UL B-crib	Crib placed on a solid surface. Well-ventilated on 5 of 6 sides	24 hours
FB3	1 x UL B-crib	Crib placed on a solid surface. Well-ventilated on 5 of 6 sides	46 hours

FB4	1 x UL B-crib	Crib placed on a metal grate with a 5 cm gap height to a solid surface. Well-ventilated on 6 of 6 sides	46 hours
-----	---------------	---	----------

3.3 Thermogravimetric analysis

To study the pyrolysis of the roofing membrane used in the experiments conducted in Trondheim, a thermogravimetric analysis was conducted using the Netzsch STA 499 F3 Jupiter apparatus (Figure 29), following the testing method according to DIN 51006 [64]. The results from the TGA were used to estimate the kinetic energy (activation energy and pre-exponential factor) for the pyrolysis, data which will be further used as input to make the FDS model more accurate. The TGA were conducted at the lab of Western Norway University of Applied Sciences, supervised by Maria de Las Nieves Fernandez Anez, Associated Professor at Department of Safety, Chemistry and Biomedical laboratory sciences. Only one experiment could be conducted as the university's resources were very limited.

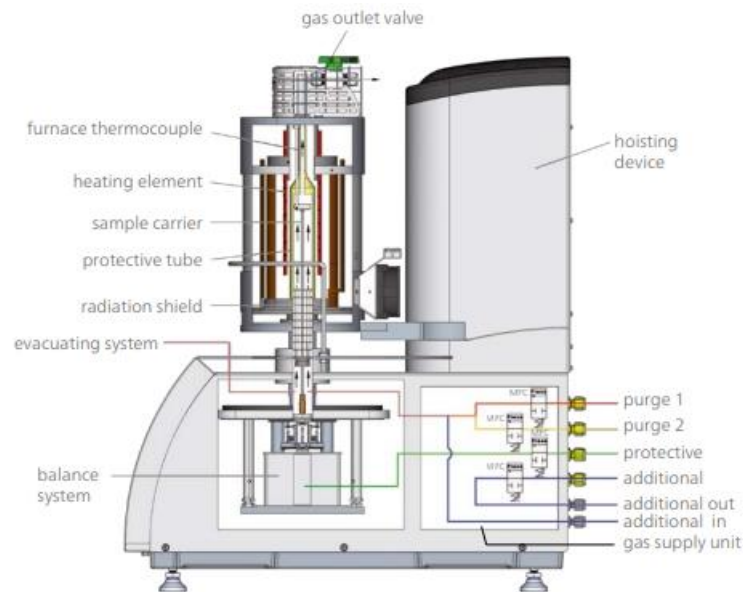


Figure 29: The apparatus used to perform the TGA was of the type Netzsch STA 499 F3 Jupiter. The figure is sourced from a brochure on Netzsch's website [65].

The apparatus underwent calibration before testing to ensure the reliability of the results. Normally, the test sample is ground into dust/smaller particles, but the roofing membrane was too tough for this. Therefore, the roofing membrane was cut into smaller pieces and placed in a crucible. The test was conducted at atmospheric pressure and with nitrogen as the ambient gas, to exclusively identify data about pyrolysis without the interference of combustion with air. The test started at 30 °C and was carried out at a heating rate of 10K/min until the test ended at 800°C. Figure 30 provides an illustration of the TGA test setup.

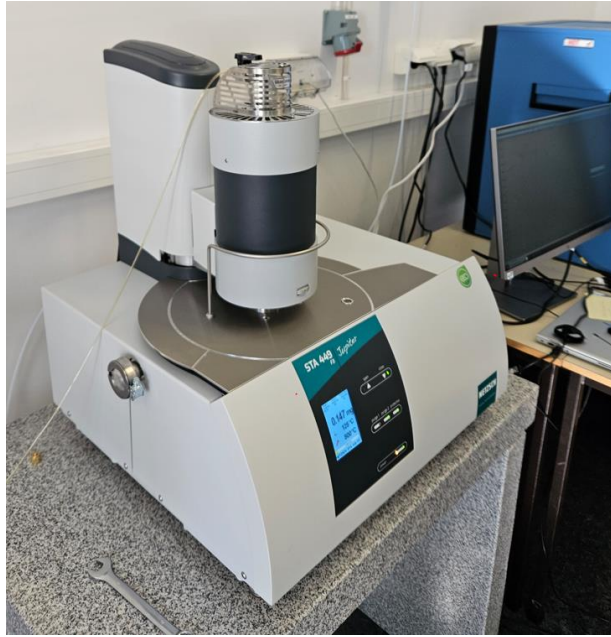


Figure 30: Illustration of the TGA test setup

3.4 Computational Fluid Dynamics Modelling

Numerical simulations were used to recreate the test setup T4 used in the small-scale experiments by Stølen et al. [3]; a PV module mounted with a 6cm gap to the roof surface, and a forced/constant wind with the speed 2m/s. The fire source used in the experiment was an EN-crib. Data from cone calorimetry- and TGA tests were used as input for the fire source and the pyrolysis of the roofing membrane in the FDS modelling.

Numerical simulations were performed leveraging the solid-phase pyrolysis solver incorporated in the Fire Dynamics Simulator (FDS) version 6.7.4 which is a highly advanced fire simulation program that uses Computational Fluid Dynamics (CFD) to model the physical processes involved in the fluid dynamics (e.g. spread of smoke and fire). It numerically solves the large eddy simulation (LES) from the Navier-Stokes equations for low Mach number. These equations involve a set of three-dimensional, nonlinear partial differential equations expressing conservation of mass, momentum and energy. Numerically, these equations are resolved by partitioning the physical space into various distinct cells. Assumptions are made within these cells that parameters including temperature, gas velocity, and others maintain a uniform state, with their variance dependent solely on the progression of time. However, the quantity of these partitioned cells that can be employed is inherently restricted by the computational power available. Computational power is the reason why the small-scale experiment was specifically chosen to recreate, rather than the medium- and large-scale experiments.

The FDS script used to model the small-scale experiment can be found in Appendix B – FDS script.

3.4.1 Pyrolysis model

An important factor for achieving the most reliable results from an FDS simulation is the accuracy of the pyrolysis reactions for the materials used in the model, in this case the construction of the roof. For simplicity, it has been decided to limit the number of materials undergoing pyrolysis to wood and roofing membrane. For modelling the pyrolysis of wood and roofing membrane, the single-reaction scheme introduced by Rinta-Paavola & Hostikaa [66] was chosen. This approach involves defining a single material and generalizing values for the most accurate fit. Figure 31 shows a schematic layout of how the single-reaction scheme that was implemented in the FDS model. Data for spruce is sourced from the study by Rinata-Paavola & Hostikaa [66], while data for Icopal Topsafe is obtained from the TGA experiment conducted at HVL, as represented in Figure 32.



Figure 31: Representation of spruce and Icopal Topsafe's single reaction scheme

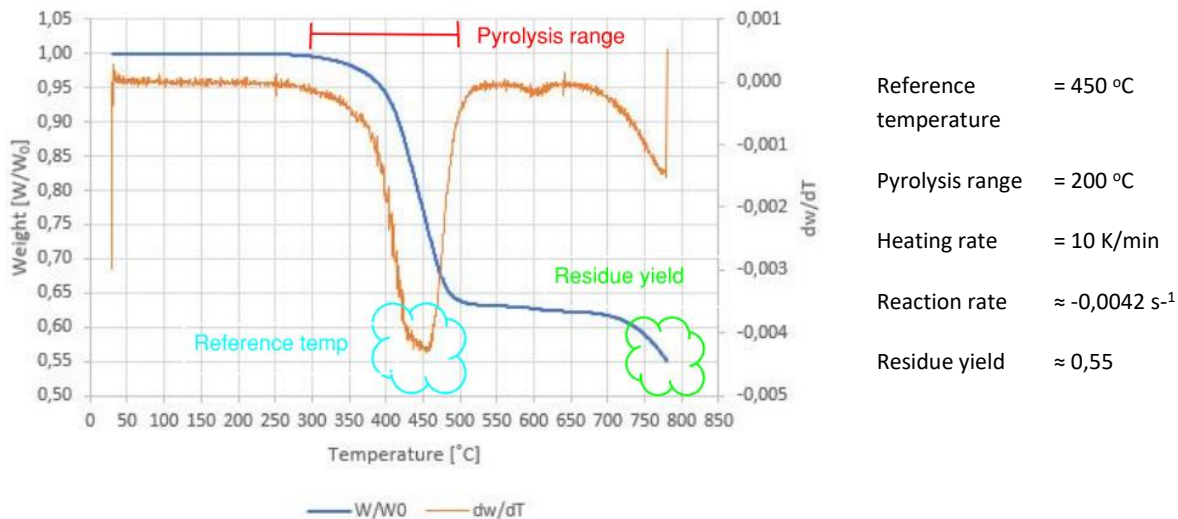


Figure 32: Results from the TGA experiment conducted on Icopal Topsafe at HVL. The mass fraction W/W_0 of Icopal Topsafe is represented by the blue curve, undergoing heating at 10 K/min. The reaction rate is represented by the orange curve dW/dt . The reference temperature, reaction rate, and residue yield represent the parameters of the multiple reactions.

Choosing the single-reaction scheme for pyrolysis modelling brings with it uncertainties due to the model's simplifications and assumptions. By reducing the pyrolysis process to a single reaction, the scheme might not adequately represent the intricate reactions involved in decomposition of wood components like hemicellulose, cellulose, and lignin. The chipboards used in the roof construction also contain components beyond just wood [67]; water, glue, paraffin wax, ammonia, ammonium nitrate, and urea.

The moisture content in the wood cribs used in the experiments in Trondheim was measured immediately after they were removed from the drying cabinet. The wood cribs were then transported to the outdoor test area, where some time also passed before they were ignited and placed on the roof construction. This means that the wood cribs may have absorbed moisture during this intervening period. For the chipboard, moisture content was not measured, but according to the installation instructions from the supplier of the chipboards, the boards should not contain more than 10% moisture when installed [60]. From the study by Rinata-Paavola & Hostikaa [66], a 9% moisture content in the wood is described, which has subsequently been used in the reaction scheme of the FDS model.

In the preceding sections, several uncertainties associated with the setup of the pyrolysis model have been presented. To assess the influence of these uncertainties on the accuracy of the simulation, a sensitivity analysis focusing on the various parameters could be performed. This would involve comparing factors like moisture content, single- and parallel-step reaction schemes, among other pertinent variables. Such an analysis would clarify how much the assumptions and simplifications inherent in the single reaction scheme, as well as variations in other parameters, influence the model's output. A total of 5 simulations were conducted, all with a mesh cell size of 0,01m, where variations were made in the parameters reference temperature and pyrolysis range for the roofing membrane. The starting point for the parameters was a reference temperature of 450°C and a pyrolysis range of 200°C. The setup for the experiments can be seen in Table 7. It should be noted, however, that other parameter analyses fall outside the remit of this thesis but remain an important avenue for future research.

Table 7: Overview showing the setup of the parameter sensitivity analysis in FDS for the parameters reference temperature and pyrolysis range. The cell size of 0,01m remained the same in all analyses. The starting point for the parameters was a reference temperature of 450°C and a pyrolysis range of 200°C

Test ID	Cell size, δx [m]	Reference temperature [°C]	Pyrolysis range [°C]
FDS1	0,01	300	200
FDS2	0,01	350	200
FDS3	0,01	400	200
FDS4	0,01	450	300
FDS5	0,01	450	350

3.4.2 Model geometry

The geometry of the model follows the setup of the small-scale experiment T4 conducted by Stølen et al. [3], with some minor but necessary adjustments to ensure that the dimensions of the materials align with the mesh grid size and its associated calculations performed in the domain. An overview of the adjustments between the small-scale experiment and FDS model geometry is shown in Table 8. The biggest difference between the small-scale experiment and the FDS model is the thickness of the PV module. With the available computing power and a mesh size of 5mm, the total computation time amounted to 9 days. Reducing the mesh size by a factor of 2 would result in approximately 16 times more computation time [55], which would not have been feasible for this thesis. Another adjustment worth mentioning is the simplification of the wood crib in FDS. As seen in Figure 33, method 3 has been selected, where a burner is applied to a VENT and placed on top of the surface of an inert obstruction. When a wood crib is modelled in this manner, the burning time remains consistent, and it experience uniform combustion across its entire surface area post-ignition. If there's insufficient oxygen, the fire will decrease or even extinguish in real life, this is not the case for method 3 as the cribs burning time will still adhere to the pre-determined HRR. The inert obstruction will impede airflow through the object, which may affect the fire propagation upwards the roof construction. In addition, the inert object will impede conductive heat transfer from the fire to the roof construction. As a final result, the device for measuring temperature in the roof construction positioned closest to the fire will also be affected by the mentioned impediment.

Table 8: Overview of adjustments between small-scale experiment [3] and FDS model geometry

	Small-scale experiment T4 [3]	FDS model
Roof construction dimensions	40 x 100 x 3,7 ¹⁾ cm (W x L x H)	40 x 100 x 2 ¹⁾ cm (W x L x H)
Roof construction thickness¹⁾	3 mm roofing membrane + 22 mm chip board + 12 mm calcium silicate	3 mm roofing membrane + 17 mm chip board
Mock-up PV module dimensions	35 x 85 x 0,2 cm (W x L x H)	36 x 85 x 1 cm (W x L x H)
Gap height between mock-up PV module and roof construction	6 cm	6 cm
Wood crib dimensions	100 x 100 x 20 mm (W x L x H). A total of 8 wood sticks measuring 10 x 10 x 100 mm (W x H x L), with six sticks placed over the final two sticks	100 x 100 x 20 mm (W x L x H). A 'burner' applied to a VENT, placed on top of the surface of an inert obstruction
Position of wood crib	5 cm from the edge of the roof	4 cm from the edge of the roof
Wind	2 m/s	2 m/s
The roof construction inclination	30°	A flat construction where gravitational force is configured as

		GVEC=-4.905., 0., -8.495709 (X, Y, Z axes)
--	--	--

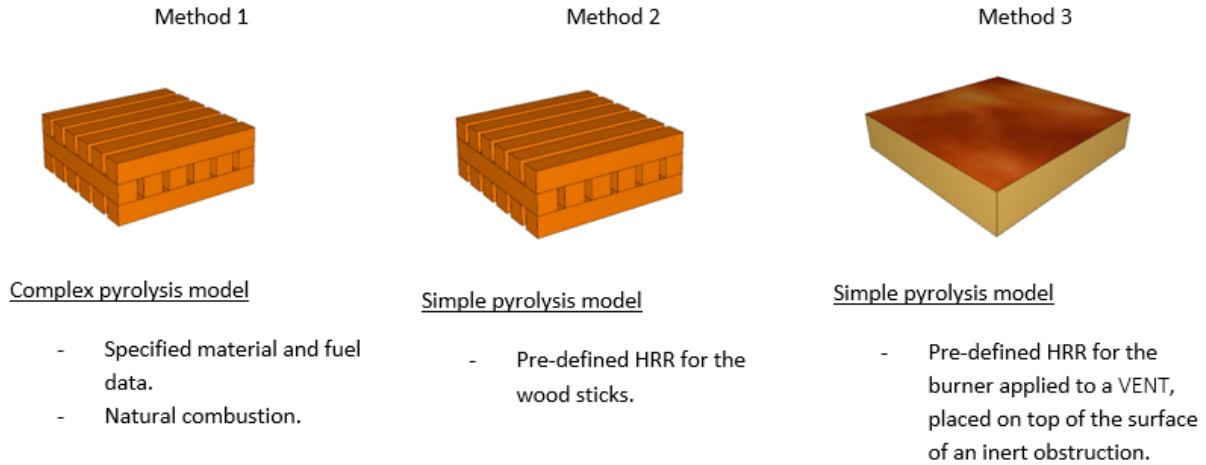


Figure 33: Schematic figure of the modelling of wood cribs

Figure 34 shows illustrations of the FDS model. On the outside of the roof construction and PV module the simulated domain is expanded 8 cm from the front and 2cm above the PV module to capture the fire plume and combustion reactions occurring outside the construction, contributing to total HRR during the fire.

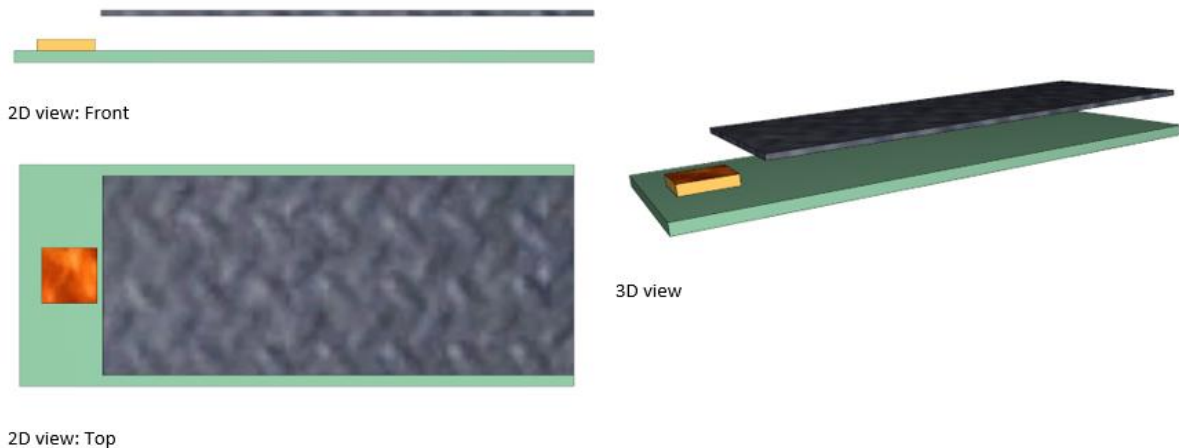


Figure 34: Snippets of model geometry

3.4.3 Material properties

The material properties of the roof construction and the PV module were each characterized using two SURF lines. The roof construction SURF line consisted of a three mm layer of 100 % Icopal Topsafe + a 22mm layer of 91 % spruce and 9 % water. The PV module SURF line consisted of a 2mm layer of 100 % steel. Table 9 provides an overview of the material properties used in the setup of the FDS model.

Table 9: Material properties used in the setup of the FDS model.

Material	Icopal Topsafe	Spruce	Char spruce	Water	Steel
Density [kg/m ³]	1143 [68] ^{a)}	408 [66]	59 [66]	1000 [66]	7850 [69]
Specific heat [kJ/kgK]	1,47 [68] ^{a)}	0,92 (30°C) 1,8 (230°C) [66]	1430+0,335T- (7,32·10 ⁷)/T ² (absolute temperature) [66], [70]	4,7 (20°C) 6,7 (230°C) [66]	0,46 [69]
Conductivity [W/mK]	0,2 [68] ^{a)}	0,09 [71]	0,22 [71]	0,6 [66]	45,8 [69]
Emissivity [-]	0,9 [68] ^{a)}	0,9 [66]	0,85 [66]	0,9 [66]	0,95 [69]
Heat of combustion [kJ/kg]	3,333·10 ⁴ [68] ^{a)}	1,375·10 ⁴ [66]	-	-	-
Heat of reaction [kJ/kg]	83 [68], [72] ^{c)}	19 [66]	-	2500 [71]	-
Reference temperature [°C]	450 ^{b)}	-	-	-	-
Heating rate [K/min]	10 ^{b)}	-	-	-	-
Pyrolysis range [°C]	200 ^{b)}	-	-	-	-
Pre-exponential Factor [1/s]	-	2,19311·10 ¹¹ [66], [71]	-	8,725·10 ¹⁶ [66], [71]	-
Activation Energy [kJ/mol]	-	1,905·10 ⁵ [66], [71]	-	1,36·10 ⁵ [66], [71]	-
Mass Fraction Exponent [-]	-	1,89 [66], [71]	-	3,31 [66], [71]	-

^{a)} Data was carried out through email correspondence with Snorre Semmingsen, Product Approvals and Development Manager at BMI Norway (manufacturer of Icopal Topsafe) [68].

^{b)} Data from the TGA experiment conducted on Icopal Topsafe at HVL (Figure 32)

^{c)} Specific data for Icopal Topsafe could not be found. Email correspondence with Snorre Semmingsen, Product Approvals and Development Manager at BMI Norway (manufacturer of Icopal Topsafe), suggests

that bitumen makes up approximately 60% of the composition of Icopal Topsafe. For that reason, data for bitumen was used instead [68]

The SURF lines were then linked to their respective obstruction surfaces and attributed BACKING='AIR'. It means; should the obstruction be no thicker than one cell, the innermost layer will be exposed to the air temperature on its reverse side. On the other hand, if the obstruction is situated at the domain's boundary or is thicker than one cell, it is presumed to abut an air gap at ambient temperature [55].

3.4.4 Reactions

For simplicity, it has been decided to limit the number of materials undergoing pyrolysis to wood and roofing membrane. 'SPRUCE PYROLYZATE' and 'BITUMEN PYROLYZATE' are the two reactions incorporated in the model. The REAC lines from the model is illustrated beneath:

&REAC

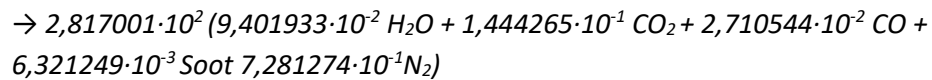
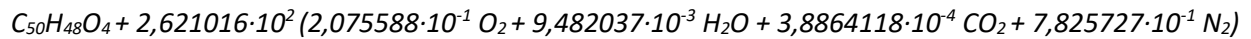
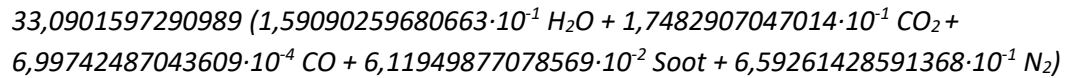
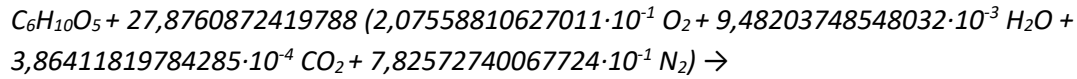
```
ID='SPRUCE_PYROLYZATE',  
HEAT_OF_COMBUSTION=1.375E+4,  
FUEL='SPRUCE_PYROLYZATE',  
SPEC_ID_NU='SPRUCE_PRODUCTS','AIR','SPRUCE_PYROLYZATE',  
NU=33,0901597290989,-27.8760872419788,-1.0/
```

&REAC

```
ID='BITUMEN_PYROLYZATE',  
HEAT_OF_COMBUSTION=3.333E+4,  
FUEL='BITUMEN_PYROLYZATE',  
SPEC_ID_NU='BITUMEN_PRODUCTS','AIR','BITUMEN_PYROLYZATE',  
NU=2.817001E+02,-2.621016E+02,-1.0/
```

In order to facilitate multiple reactions in a single simulation, 'complex stoichiometry' must be specified. As a result, the oxidation interaction between fuel and air needs to be clearly defined. The combustion process was modelled as a single-step reaction of $C_6H_{10}O_5$ (spruce) and $C_{50}H_{48}O_4$ (bitumen) [73] p. 5 figure 2. The molecular formula for bitumen was used in lack of micro-scale calorimetry to assess to correct formula for Icopal Topsafe. Values for soot and CO yields in spruce are respectively 0,015 and

0,004 (g/g) [74], along with 0,030 and 0,300 (g/g) for bitumen [75]. The stoichiometric balanced equation for spruce and bitumen is given as:



3.4.5 Initial fire

The initial fire implemented in the model is an INERT box with the dimensions 100 x 100 x 20mm (W x L x H), where a BURNER is applied to a VENT, placed on top of the surface of the inert obstruction. The crib was placed in the center of the model, 4cm from the eaves. The crib had to be positioned 1cm further back than what was done in the small-scale experiments; otherwise, the crib would have blocked all data from the DEVICE placed directly near the fire. The BURNER was specified based on the burning characteristics from cone calorimeter tests on EN-cribs, as illustrated in Figure 35.

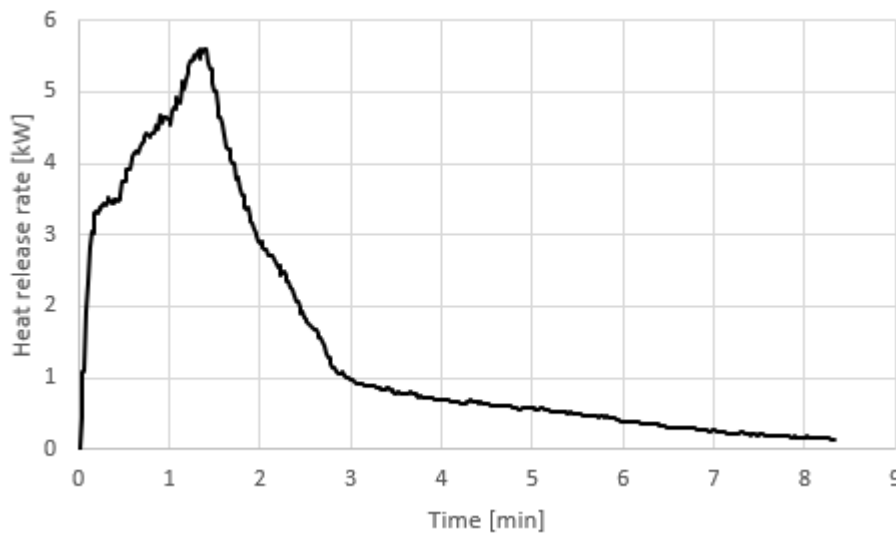


Figure 35: A series of three EN-cribs were tested using the cone calorimeter to acquire data for the initial fire used in the model. The experimental data for the heat release rate is illustrated in the figure above.

3.4.6 Device configuration

Temperature measurements were recorded, using solid-phase devices, along the centerline in the following layers of the construction: below the chipboard, above the chipboard on atop of the roofing, and on top of the surface of the PV module.

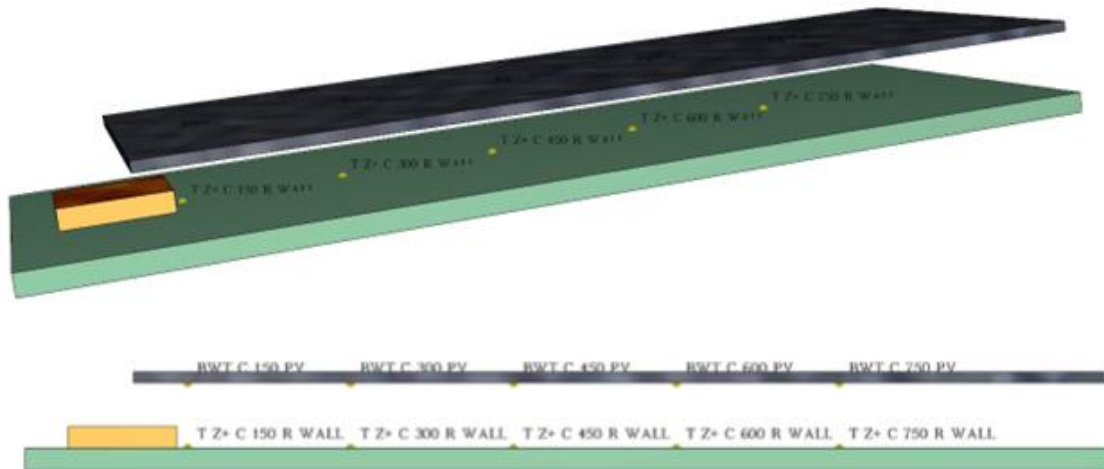


Figure 36: Illustration of the positioning of the solid-phase devices measuring temperatures in FDS

3.4.7 Mesh

The mesh resolution serves as a critical parameter in FDS, as it significantly influences the quality of the numerical solution. This quality is particularly manifested in the accuracy with which the flow field and geometry are resolved. FDS calculates the average value for each cell, and if the cell division is too coarse, the maximum and minimum values will be underestimated. Therefore, achieving a mesh-independent solution will be necessary to minimize the error source in the numerical solution. Independence can be achieved by starting with a relatively coarse mesh and gradually refining the mesh until it is no significant differences in the results. To save computing time, it may be necessary to allow some variation in the mesh grid cell size in the model as there will be the greatest need for a fine resolution near the fire/burner. As a first estimate for validation of simulations involving buoyant plumes, FDS user guide refers to the non-dimensional expression $D^*/\delta x$, where D^* is a characteristic fire diameter and δx is the nominal size of a mesh cell. $D^*/\delta x$ can roughly speaking be given in the interval from 4-16, where 4 represents a coarse mesh resolution, 10 medium and 16 fine.

Data from cone calorimeter tests of EN-cribs gives a mean HRR $\dot{Q} \approx 5,60\text{kW}$. Section 2.4.4 provides an explanation of the D^* -approach and Table 10 gives a representation of the mesh resolution $D^*/\delta x$ used in the sensitivity analysis. For calculations related to the mesh resolution, see Appendix A – FDS mesh calculations.

In this thesis, three mesh resolutions were employed; 20mm, 10mm and 5mm.

Table 10: A representation of the mesh resolution used for sensitivity analysis. For calculations, see Appendix A – FDS mesh calculations

Cell size, δx [m]	$D^*/\delta x$	Number of cells
0,02	6	9840
0,01	12	51 120
0,005	24	382 080

The mesh sensitivity analysis consisted of executing simulations at various grid resolutions while keeping boundary conditions and material properties constant. This was done to evaluate how cell size affects the simulated fire dynamics. Temperature and HRR served as the comparative parameters across these analyses.

4. Results

This chapter will present the results derived from; i) the medium- and full-scale experiments conducted in collaboration with RISE Fire Research, ii) wood crib burning experiments, iii) TGA experiment and iv) the FDS simulations.

4.1 Experiments conducted in collaboration with RISE Fire Research

In the fall of 2022, a series of six medium-scale experiments and two full-scale experiments were conducted to investigate the impact of mock-up BAPVs on the propagation of fire along a 30° inclined roof construction [3]. The author of this master's thesis was actively involved as a project collaborator in the planning and execution of these experiments.

4.1.1 Medium-scale experiments

Of the total 6 experiments conducted with the medium-scale setup, the first 3 experiments were conducted in the absence of a PV module, while the last 3 were conducted with a PV module mounted 12 cm above the roof surface. Figure 37 shows overview images from experiment M4.



Figure 37: An illustration of the experiment with test setup M4; UL B-crib and PV module.

4.1.1.1 Temperature measurements

Temperatures were measured in two positions in the different layers of the construction. For the test setups with a PV module, temperatures were measured in the same positions on top of the PV module, this applies to experiments M4-M6, the M3 setup was carried out without a PV module. The first two experiments (M1 and M2) were conducted without instrumentation, and for this reason, temperature measurements for these experiments are not available. Figure 38 shows an overview of the measured temperatures in experiments M3-M6. The temperature measurements on top of the PV module correspond with the extent of damage (Table 11), showing that experiment M4 is the setup with the highest measured temperatures. An interesting observation is that the temperature measured at the 900mm position is approximately the same in experiments M3 and M4, both conducted with UL B-crib, but in presence and absence of a PV module. The effect of the PV module is shown for the measured temperature at the 2000mm position, where the temperature variation is greatest for M4 with a PV module.

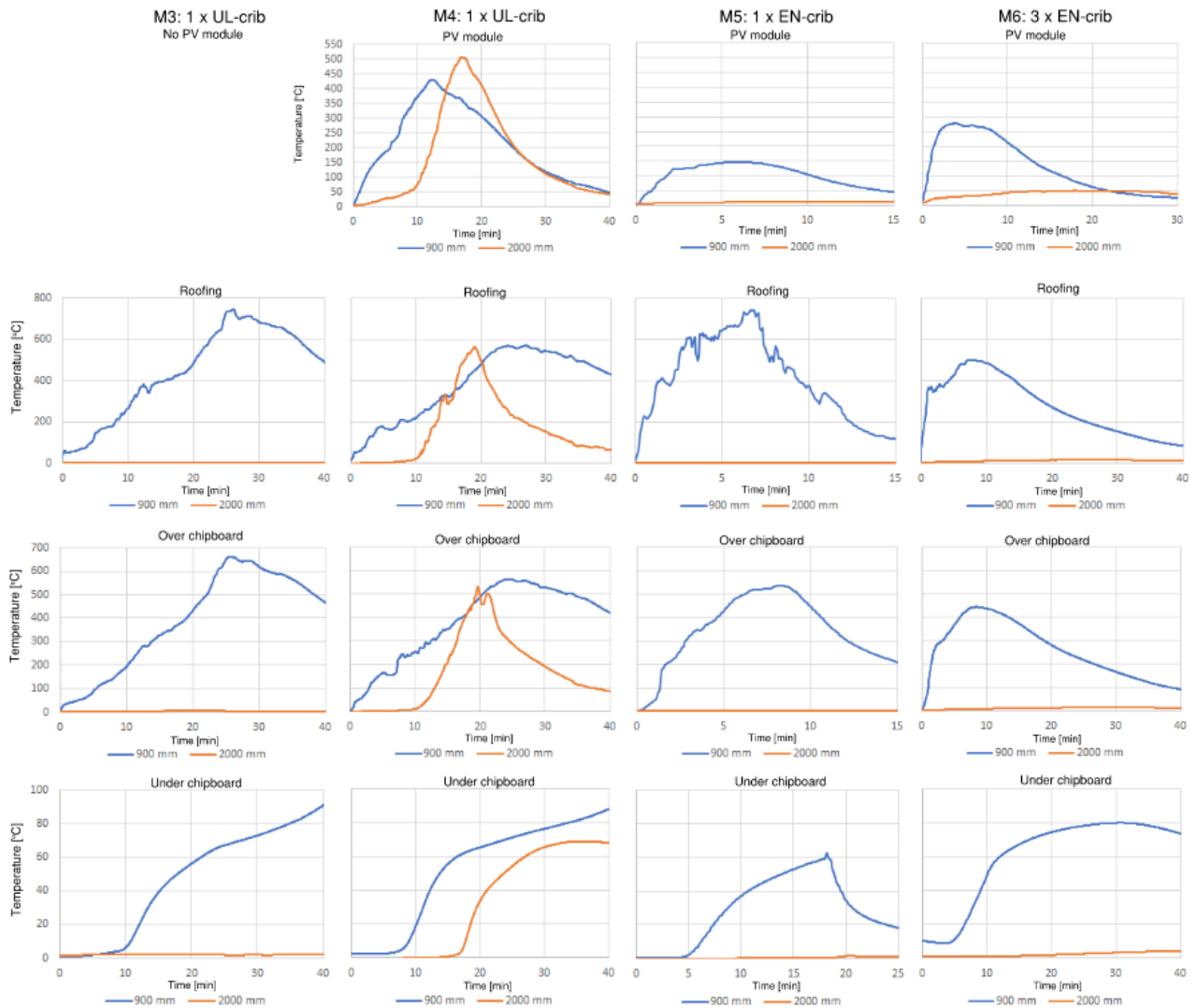


Figure 38: Overview showing measured temperatures in two positions in the different layers of the construction, as well as on top of the PV module for the setups M3-M6. The M3 experiment was carried out without a PV module. The M1 and M2 experiments were not instrumented for temperature measurements. The Y-axis shows temperatures (Celsius) that are common for all figures in the same row. The X-axis shows time (minutes) which is individual per figure. The blue curve shows the measured temperature 900mm from the eaves/in the centre of the wooden crib/30cm from the lower end of the PV module. The orange curves show the measured temperature 2000mm from the eaves/30cm from the upper end of the PV module. The figure shows 4 columns, each column corresponding to the described test setup at the top of the figure.

4.1.1.2 Extent of damage

Table 11 summarizes the measured length and width of the damage extent on the roofing membrane from the various experiments, while Figure 39 illustrates the damages. Both fire spread and extent of damage were greatest in experiment M4 (Figure 37) with UL B-crib and PV module.

Table 11: Summary of measured damage extent on the roofing membrane in the medium-scale experiments. The length of the damaged area was measured from the centre of the wooden crib upwards along the roof surface, while the width was measured at the point where the damage area was widest.

Test ID	Initial fire	PV module	Length of the damaged area	Width of the damaged area
M1	1 x EN-crib	No	12 cm	12 cm
M2	2 x EN-crib	No	12 cm	16 cm
M3	1 x UL-crib	No	38 cm	26 cm
M4	1 x UL-crib	Yes	150 cm ¹⁾	80 cm
M5	1 x EN-crib	Yes	15 cm	12 cm
M6	3 x EN-crib	Yes	70 cm	17 cm

¹⁾ The fire spread all the way to the top of the roof surface. Flames were observed approximately 1 meter outside of the ridge.

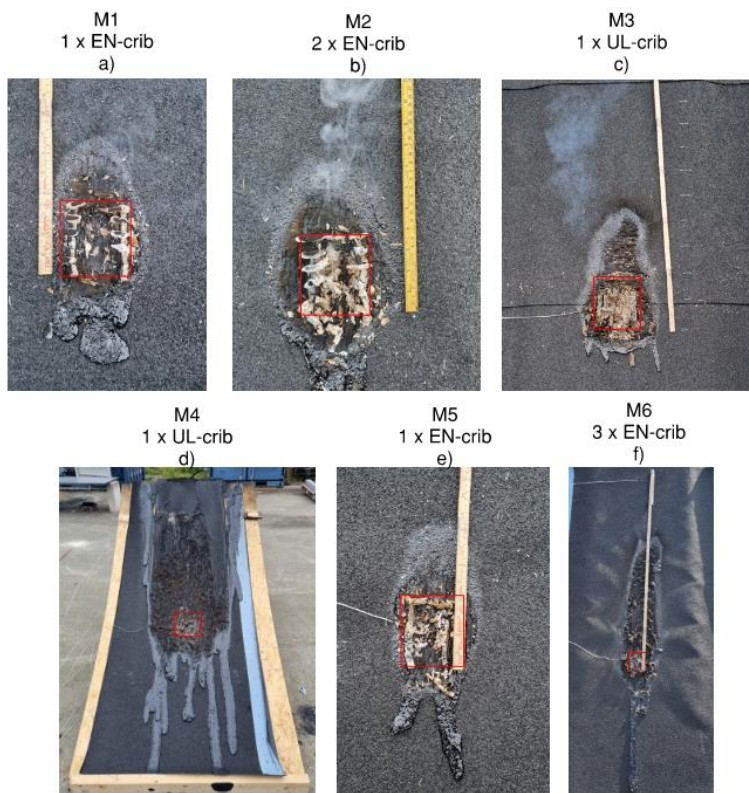


Figure 39: Overview showing the extent of damage to the roofing membrane in the medium-scale experiments. a)-c) show the extent of damage from experiments without PV module. d)-f) show the extent of damage from experiments with PV module. Red squares illustrate the approximately placement and size of the wooden cribs.

4.1.2 Full-scale experiment

In total, 2 full-scale experiments were conducted, both performed with UL B-crib and PV modules mounted 12cm above the roof surface. Unlike experiment F1, in experiment F2, a steel gutter was installed at the eaves, and the middle part of the roof construction was extended by 1,0m in length and 1,3m in width. The changes were made to study the effect of collecting melted roofing membrane and extending the construction on flame spread. Figure 40 shows overview images from experiment F1.



Figure 40: Overview images from experiment F1

4.4.2.1 Observations

Observations made in both full-scale experiments correspond with experiment M4 in the medium-scale setup in that the fire from the ignited wooden crib spreads upwards along the roof surface in the cavity formed by the PV modules. The fire in both experiments resulted in melted roofing membrane running down the roof, as shown in Figure 41. In experiment F1, flames in the melted roofing membrane that collected on the ground could be observed. To prevent the flames at the eaves from establishing themselves in the roof ridge, the flame was manually extinguished with water several times during the experiment. Visible flames were not observed in experiment F2, where the melted roofing felt collected in the gutter. Observations made for both experiments are compiled in Table 11.



Figure 41: Illustration showing the melted roofing membrane at the eaves in both experiments. In experiment F1 a) the roofing membrane was collected on the ground, while in experiment F2 b) the roofing membrane was collected in a gutter. Only in experiment F1 did the fire spread downwards in the roof construction.

Table 12: Observation log from the two large-scale experiments F1 and F2. The log is sourced from Stølen et al. [3] p. 27.

Observation	Time from the start of the experiment	
	[min:sec]	
	F1	F2
Ignited UL-crib placed on the roof surface	00:00	00:00
Flames reaching the upper edge of the lower modules	11:11	13:00
Flames reaching the upper edge of the upper modules	16:30	19:30
Melted roofing material running down from the roof	14:54	12:00
Fire in melted roofing material below the roof	18:58	Not observed
Fire in the railing above the top of the test object	21:20	26:30
Fire extinguished itself	75:13	59:24

4.4.2.2 Temperature measurements

Temperature measurements were made in the centerline of the three columns of PV modules in both experiments. Figure 42 provides an overview of the temperatures measured on top of the PV modules and on the roofing membrane. As can be seen from the figure, a comparison is made of temperatures

measured in experiments F1 and F2 at different positions along the roof construction. Only the centerline of the middle PV modules was instrumented for temperature measurements into the roof construction. Therefore, Figure 43 provides an overview of the temperatures measured above and below the chipboard.

From Figure 42, little temperature increase is observed on the left side, only a greater increase in the center and on the right side of the construction. On the right side, it is observed that the temperature increase is greatest for the top measurement points on the PV module and the roofing membrane. From the measurements made in the centerline of the middle modules, it is seen that the temperature goes from being stably low to suddenly increasing between 10 and 20 minutes, with the exception of the measurement point in the center of the initial fire where a rapid temperature rise is observed immediately. Maximum temperatures on PV modules and roofing membrane are respectively about 550°C and 750°C for both experiments.

Further inwards the roof construction, as seen from Figure 43, the same observations apply for above and below the chipboard in the centerline of the middle PV modules. The maximum temperature measured above the chipboard was highest for experiment F2 at about 800°C compared to experiment F1 at about 550°C. However, the opposite was true for measurements under the chipboard, where F1 measured a maximum temperature of about 100°C and F2 measured about 80°C.

It is also observed that the temperature increase below the chipboard starts around 20 minutes, a delay compared to the other layers in the construction and the PV module.

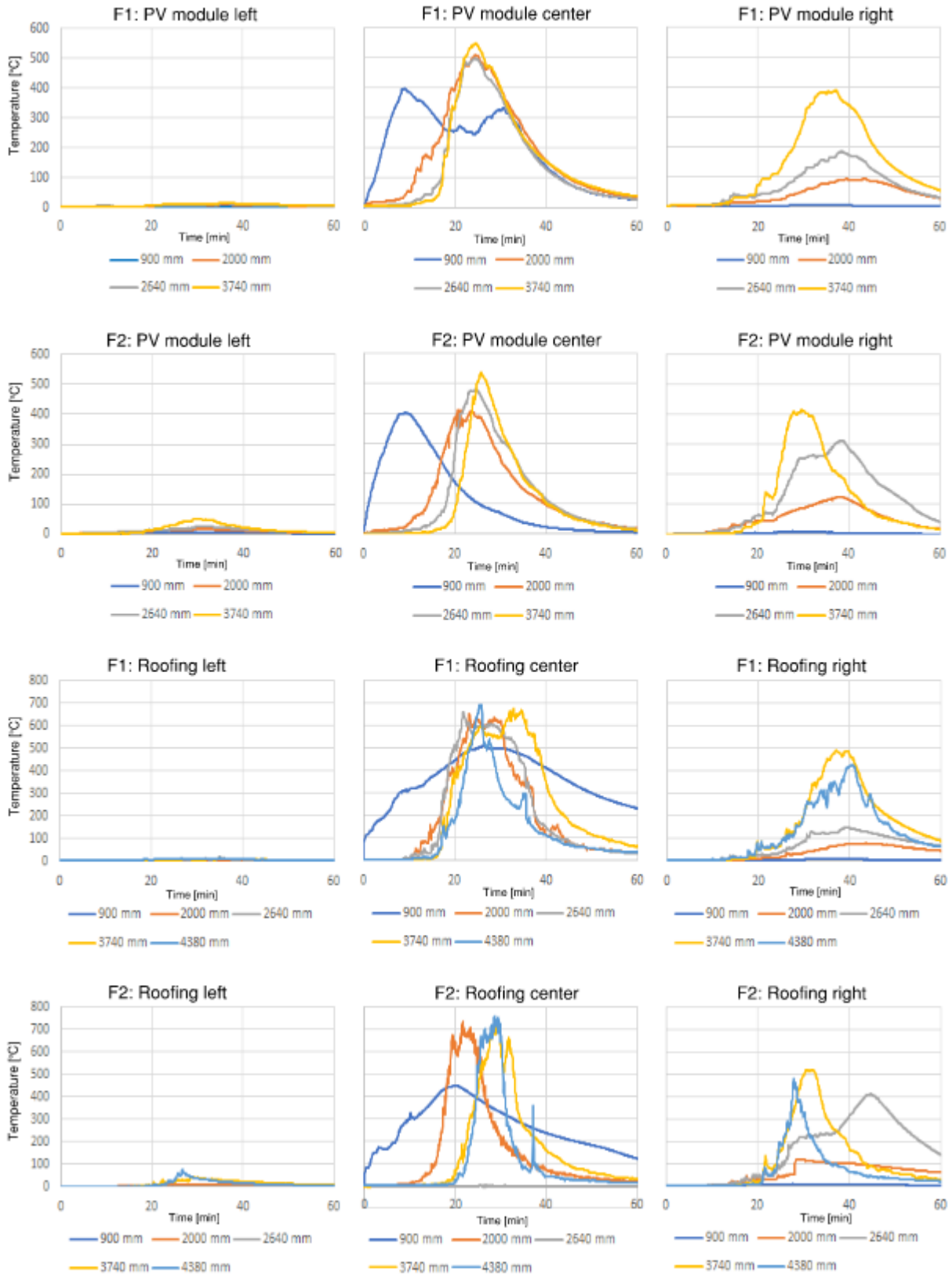


Figure 42: An overview of the temperatures measured on top of the PV modules and on the roofing membrane for experiments F1 and F2. Temperature measurements were made in the centreline of the three columns of PV modules in both

experiments. The Y-axis shows temperatures (Celsius) that are common for all figures in the same row. The X-axis shows time (minutes) which is individual per figure.

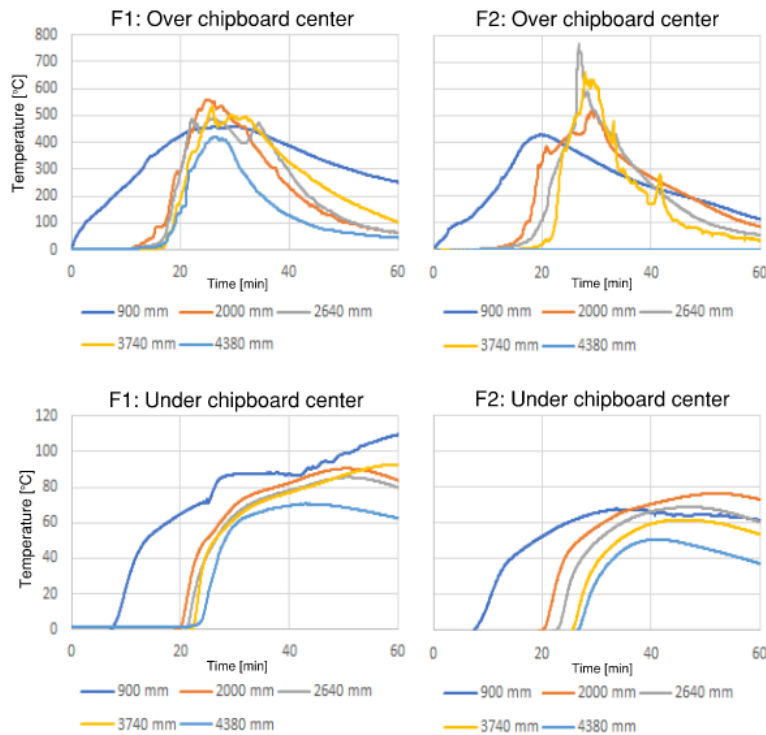


Figure 43: An overview of the temperatures measured above and below the chipboard in the centreline of the middle PV modules in both experiments. The Y-axis shows temperatures (Celsius) that are common for all figures in the same row. The X-axis shows time (minutes) which is individual per figure.

4.4.2.3 Extent of Damage

The PV modules were removed after the experiments were completed and the test rig had cooled down. Figure 44 shows the extent of damage from experiments F1 and F2. The placement of the PV modules is marked with red squares and the wooden crib is marked with a yellow square. Similar to the temperature measurements, it is observed that the fire has spread upwards along the construction all the way to the top, specifically along the centre and up towards the right. Even though the centre of the construction was extended in experiment F2, it is observed that the extent of the damage is no longer than for experiment F1. The damaged area to the right in the construction is somewhat wider for experiment F2 than F1.



F1
a)



F2
b)

Figure 44: An overview of the extent of damage for experiments F1 and F2. Red squares illustrate the placement of PV modules, and a yellow square illustrates the placement of the wooden crib.

The chipboards in the centreline of the middle PV modules were dismantled and cut in the same positions as the temperature measurements were made. The cross-section of the chipboards (Figure 46) shows the depth of the charring, which is also listed in Table 12. In Figure 45, it is shown that there was a minor burn-through at the joint of the chipboards in experiment F1, approximately at the 2640mm position. The same OSB boards were used in experiment F2, and as can be seen from the figure, the burn mark did not increase further after experiment F2.



Figure 45: Marks from burn-through at the joint of the chipboards in experiment F1. The burn mark did not increase further after experiment F2

Table 13: Depth of charring in the OSB (oriented strand board) beneath the roofing material along the centreline of the roof for the two large-scale experiments F1 and F2. The table is sourced from Stølen et al. [3] p. 32

Distance from the lower edge of the roof [mm]	Depth of charring [mm]	
	F1	F2
4380	4	3
3740	7	6
2640	9	7
2000	11	6
900	14	10



Figure 46: Depth of charring in the chipboards shown by cross-section in the same positions as the temperature measurements were made

4.2 Wood crib burning experiments

A total of 3 cone calorimetry experiments with EN-cribs and 4 free burning experiments with UL B-cribs were conducted to study the mass loss rate and heat release rate of the initial fires used in this thesis. The results from these tests will be used further as input for modelling in FDS.

4.2.1 Cone calorimeter

A series of three EN-cribs were tested using the cone calorimeter to acquire data for the initial fire used in the FDS model. The mean experimental data for the heat release rate is illustrated in Figure 47. Peak HRR was measured to approx. 5,5kW after 1,5min.

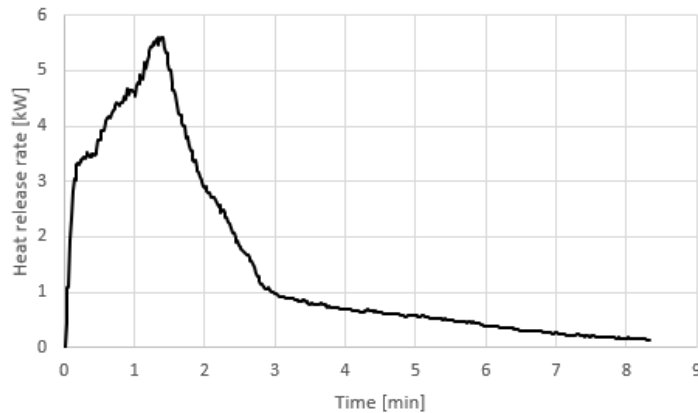


Figure 47: A series of three EN-cribs were tested using the cone calorimeter to acquire data for the initial fire used in the FDS model. The mean experimental data for the heat release rate is illustrated in the figure above.

Figure 48 shows the mass loss rate of the first two cone calorimeter experiments. Data for the mass loss in experiment CC3 was corrupt and cannot be used further. It was decided to run tests without walls (retainer) around the wood crib so that the wood cribs had free access to oxygen from all sides except the bottom. This is similar to the test setup used in the experiment by Stølen et al. [3] except that the wood crib was exposed to a constant cone heat flux. Because the wood crib had no retainer, it lost fewer pieces along the way, an effect that can be particularly seen in the graphs for mass loss. The pieces fell off the scale, resulting in a significant mass loss within a remarkably brief time, or “peaks” as shown in the graphs.

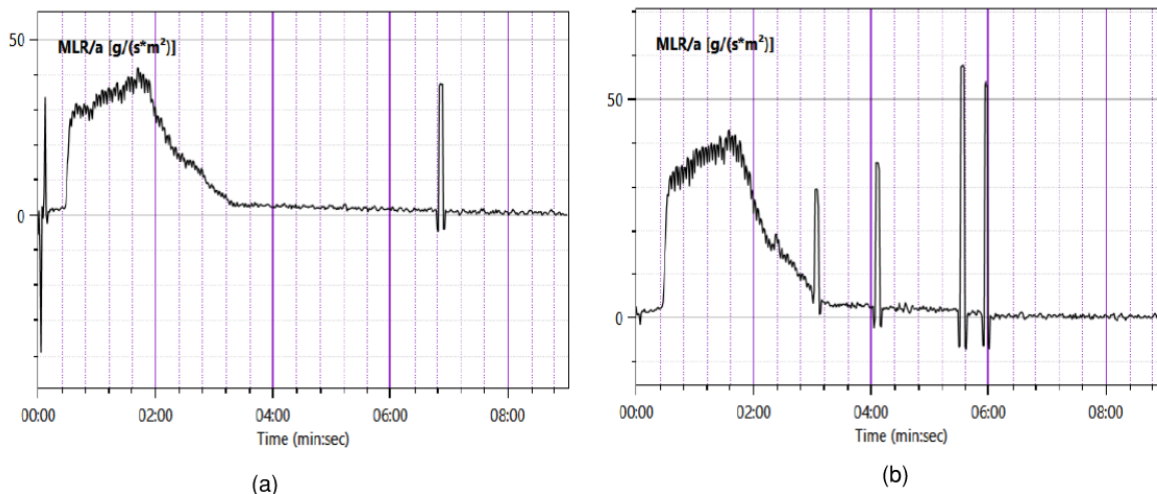


Figure 48: Mass loss rate for experiment a) CC1 and b) CC2. Corrupted/damaged data file for CC3 could not be used.

Table 14 provides a brief overview from the test reports of the cone calorimetry experiments. All three tests gave relatively similar results.

Table 14: Experimental overview for the cone calorimetry test

Test ID	Cone heat flux	Initial mass	Residual weight	Test duration
CC1	15 kW/m ²	50,40 g	1,75 g	10 min
CC2	15 kW/m ²	51,24 g	1,63 g	10 min
CC3	15 kW/m ²	50,28 g	1,63 g	10 min

4.2.2 Free burning

A series of four UL B-cribs were burned in a well-ventilated indoor lab. The ignition of the UL B-cribs was performed in the same manner as in the experiments conducted in Trondheim. By accident, the cribs for experiments FB3 and FB4 were dried for approximately 22 hours longer than for experiments FB1 and FB2. The extended drying time has possibly affected the initial weight shown in Table 15. The same can be said about the residual weight after the flames were extinguished. Here, there is significantly less remaining mass of FB3 and FB4. In addition to FB4 being conducted with free air access from the underside as well, it may be assumed that the amount of moisture in the cribs has an impact on these results. Between 54-98g of weight is lost in the four different experiments as a result of the ignition routine with a propane burner. This constitutes between 18,4-26,7% of the initial mass of the cribs. After the flames were self-extinguished and the tests were completed, the effect of the glowing wood pieces can also be observed. A total of 97,4-98,5% of the initial mass was lost until there was no more heat left in the embers.

Table 15: Overview of weight loss across all experiments where UL B-cribs were burned in a well-ventilated indoor test lab

Test ID	Initial weight [g]	Weight after 4 minutes of ignition [g]	Test duration/flame extinguished [min:sec]	Weight after the flame was extinguished [g]	Residual weight after cooling [g]
FB1	404	329,6	10:00	246,9	6,2
FB2	395	341,8	11:00	254,3	10,2
FB3	384	298,4	10:00	92	9,8
FB4	364	266,9	07:45	57,4	8,8

Figure 49 display the mass fraction and mass loss rate of the UL-B cribs. The outcomes of experiments FB1 and FB2 depict relatively similar graphs. In experiments FB3 and FB4, a notably greater mass loss is observed, particularly in FB4, which had free access to oxygen from the underside. The disparities between FB1/FB2 and FB3 might be attributed to a longer drying time, resulting in potentially reduced moisture in the FB3 crib.

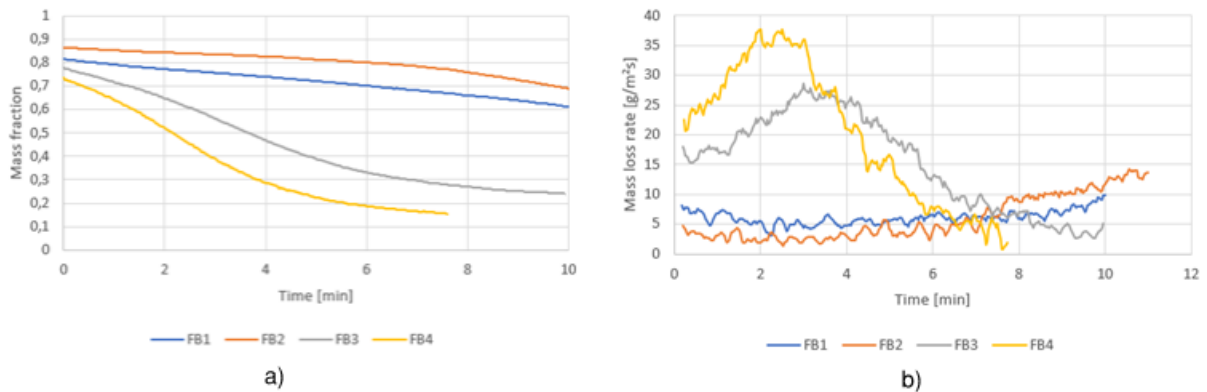
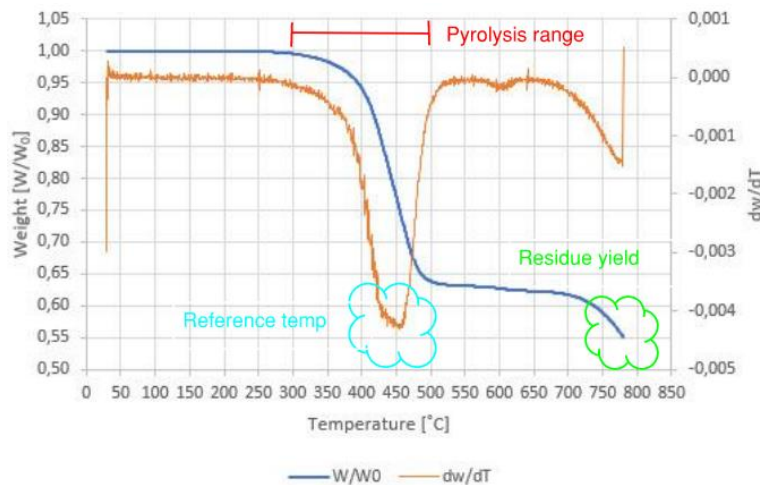


Figure 49: Overview of; a) mass fraction of the UL B-cribs and b) mass loss rate of the UL B-cribs. The measurements started after 4 minutes of ignition with a propane burner

4.3 Thermogravimetric analysis

The test was conducted at atmospheric pressure and with nitrogen as the ambient gas, to exclusively identify data about pyrolysis without the interference of combustion with air. The test started at 30°C and was carried out at a heating rate of 10K/min until the test ended at 800°C. The thermogravimetric curve is represented as a plot of weight change in relation to temperature or time. Figure 50 illustrates the pyrolysis of Icopal Topsafe, which can be divided into four stages: i) From ambient temperature to 300°C where dW/dT equals 0, an indication of little chemical or physical reactions taking place. ii) From 300-450°C where dW/dT changes from a steady value to a maximum and then 0. iii) From 510°C dW/dT is once a steady value of approx. 0 until iv) 690°C where dW/dT rapidly decreases to 800°C, where the test ended. Residue yield of the multiple reactions is 55%.

It would be of interest to perform more TGAs of the roofing membrane with both different heating rates and a higher ending temperature than 800°C. Compared with the TGA curve in Figure 8 performed for asphalt (high bitumen content, similar to Icopal Topsafe), it is seen that the dW/dT for asphalt is divided into three stages, with the maximum value around 480°C, residue yield less than 20%, and the test ending at 600°C. A reason for the higher residue yield for Icopal Topsafe might be that the roofing membrane obviously has a different chemical composition, but also a possible addition of a flame retardant. Since the TGA stopped at 600°C for the asphalt, it is unknown whether this material would also undergo additional pyrolysis at higher temperatures like Icopal Topsafe.



$$\frac{dY_s}{dt} = -AY_s \exp(-E/RT_s) \quad Y_s(0) = 1$$

$$T_p = 450 \text{ } ^\circ\text{C}$$

$$r_p \approx -0,0042 \text{ s}^{-1}$$

$$T = 10 \text{ K/min}$$

$$V_s \approx 0,55$$

Figure 50: Results from the TGA experiment conducted on Icopal Topsafe. The mass fraction W/W_0 of Icopal Topsafe is represented by the blue curve, undergoing heating at 10 K/min. The reaction rate is represented by the orange curve dY_s/dt . The ordinary differential equation that describes the transformation is shown at right. Note that the parameters T_p , r_p , and V_s represent the reference temperature, reaction rate, and residue yield of the multiple reactions.

4.4 Computational Fluid Dynamics Modelling

This chapter will be presented results for the comparison of measurements of temperature and total HRR between FDS and small-scale experiment (T4) conducted by Stølen et al. [3]; a PV module mounted with a 6cm gap to the roof surface, and a forced/constant wind speed of 2m/s. The fire source used in the experiment was an EN-crib. Data from cone calorimetry and TGA tests were used as input for the fire source and the pyrolysis of the roof construction in the FDS modelling.

In addition, results from a mesh sensitivity analysis will be presented to validate the output from FDS.

4.4.1 Mesh sensitivity analysis

Three simulations were conducted where the mesh resolution δx parameter varied; 0,02, 0,01, and 0,005m. All other parameters remained unchanged. The results for HRR, and temperature measured on the roofing membrane at a position of 300 mm from the eaves, are selected as references.

4.4.1.1 *Solid-phase temperature*

The temperature development on the surface of the roofing membrane at a position of 300 mm from the eaves are analysed and compared for the mesh resolution. Figure 51 illustrates the comparison of temperature measurements between the variable mesh resolutions, in addition to temperature measurements in the small-scale experiments.

The temperature curves from FDS closely align with the measurements made in the experiment up to approximately 2 minutes, when the temperature reaches about 300°C. After that point, the curves gradually decrease until around 10 minutes and approximately 100°C, where they then level off. Temperature measurements for a mesh resolution of 5 mm show the greatest difference compared to 10 and 20mm, which more or less align with each other. The temperatures measured with a 5mm mesh resolution are about 50°C lower than those of 10 and 20 mm in the time frame from approximately 2,5 to 8 minutes. However, the temperature curve in the small-scale experiment continues to rise after reaching 300°C in FDS, going up to approximately 550°C around the 12-minute mark, before the curve sharply decreases to about 150°C within roughly 2,5 minutes, at which point the experiment concludes.

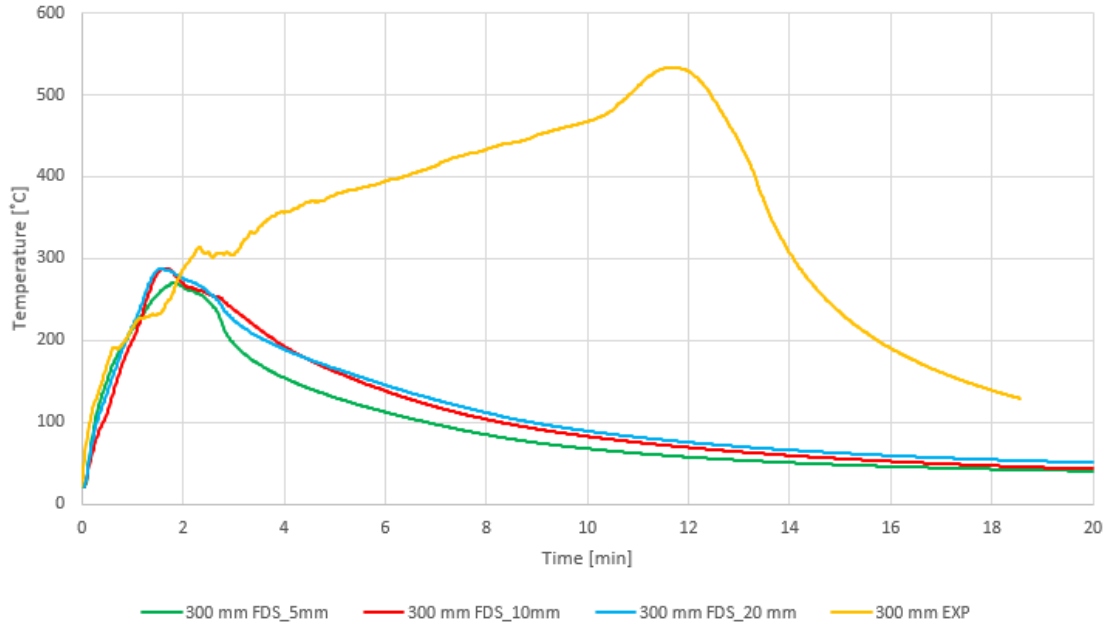


Figure 51: Comparison between the variable mesh resolution δx parameter (5mm, 10mm and 20mm) and small-scale experiments; temperature measurements on top of the roofing membrane at a position of 300mm from the eaves.

Since the greatest temperature changes from the FDS measurements occur in the time frame of 0-4 minutes, a mesh sensitivity analysis has been chosen to be performed on the average and peak temperatures for each of the three mesh resolutions. The results of the analysis are shown in Table 16.

Table 16: Mesh sensitivity analysis. Average and peak temperature in the timeframe between 0 sec to 240 sec

Temp. measured on the roofing membrane at a position of 300 mm from the eaves	Average and peak temperature for each mesh resolution [°C]		
	$\delta x = 0,005$ m	$\delta x = 0,01$ m	$\delta x = 0,02$ m
Average temp.	200	211	215
Peak temp.	270	287	287
	Average temperature difference between mesh resolutions [%]		
	0,005 vs 0,01	0,005 vs 0,02	0,01 vs 0,02
Average temp.	5,50	7,50	1,90
Peak temp.	6,30	6,30	0,00

4.4.1.2 Heat release rate

A mesh sensitivity analysis has also been conducted for the total heat release rate of the initial fire, where each grid resolution is compared with one another and the results from the cone calorimeter tests. Figure 52 presents the total HRR for each grid resolution, where one can observe that the curve for each of the three grid resolutions is approximately identical to the curve from the cone calorimeter tests. There is a rapid increase in total HRR from 0-1,5 minutes, after which there is a relatively steep decrease until 3 minutes where the curve flattens out. The most significant deviation is observed in the decreasing phase in the form of the 10mm grid resolution.

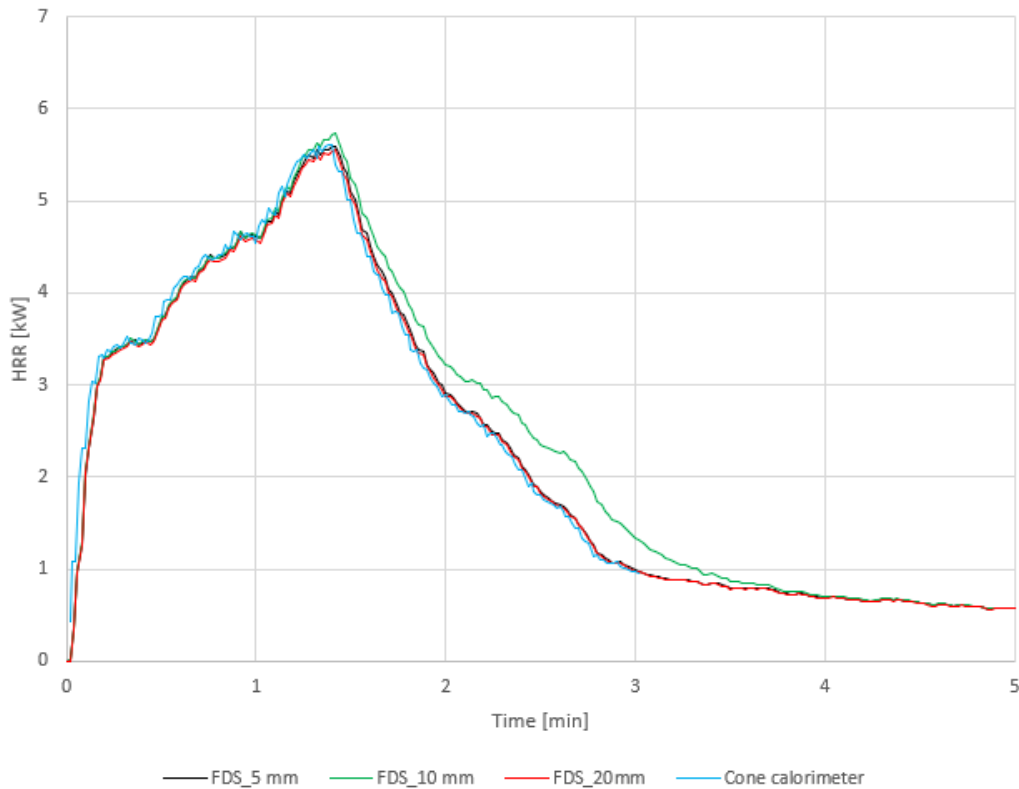


Figure 52: Comparison between the variable mesh resolution δx parameter (5 mm, 10 mm and 20 mm) and cone calorimeter experiments set against total heat release rate.

Since the greatest HRR changes from the FDS measurements occur in the time frame of 0-2 minutes, a mesh sensitivity analysis has been chosen to be performed on the average and peak HRR for each of the three mesh resolutions. The results of the analysis are shown in Table 17.

Table 17: Mesh sensitivity analysis. Average and peak total HRR for each mesh resolution in the timeframe between 0 sec to 120 sec.

Total HRR	HRR for each mesh resolution [kW]		
	$\delta x = 0,005$ m	$\delta x = 0,01$ m	$\delta x = 0,02$ m
Average	4,0108	4,0924	3,9779
Peak	5,5974	5,7277	5,5522
	HRR difference between mesh resolutions [%]		
	0,005 vs 0,01	0,005 vs 0,02	0,01 vs 0,02
Average	2,03	0,82	2,78
Peak	2,33	0,81	3,06

4.4.2 Comparison between FDS and small-scale experiment

It has been decided to use the finest mesh resolution $\delta x = 0,005$ m for the execution of the FDS simulations, based on the theory that states the finer the mesh resolution, the more accurate the calculations in FDS will be. With the available computing power and a mesh size of 5mm, the total computation time amounted to 9 days. Reducing the mesh size by a factor of 2 would result in approximately 16 times more computation time [55], which would not have been feasible for this thesis. The following sub-chapters presents a comparison of measured temperatures and HRR between FDS and the small-scale experiments will be presented.

4.4.2.1 *Temperatures measured in the different layers of the construction and on top of the PV module*

Comparison of temperatures measured in the different layers of the construction and on top of the PV module between FDS and small-scale experiment is shown in Figure 53 and Figure 54. From the modelling of the initial fire, there has in the preceding sections been observed a rapid increase in total HRR from 0-1,5 minutes, after which there is a relatively steep decrease until 3 minutes where the curve flattens out. This is also somewhat reflected in the curves of FDS, where temperatures early in the fire development (approx. 0-2 min) show a tendency to follow the temperature curves of the small-scale experiment, but quickly enter the decay phase. It is speculated whether the roofing membrane does not pyrolyze enough in FDS for the fire development to become more similar to the experiment. Most results seem to indicate that the contribution from the roofing membrane was greater in the experiment than in FDS.

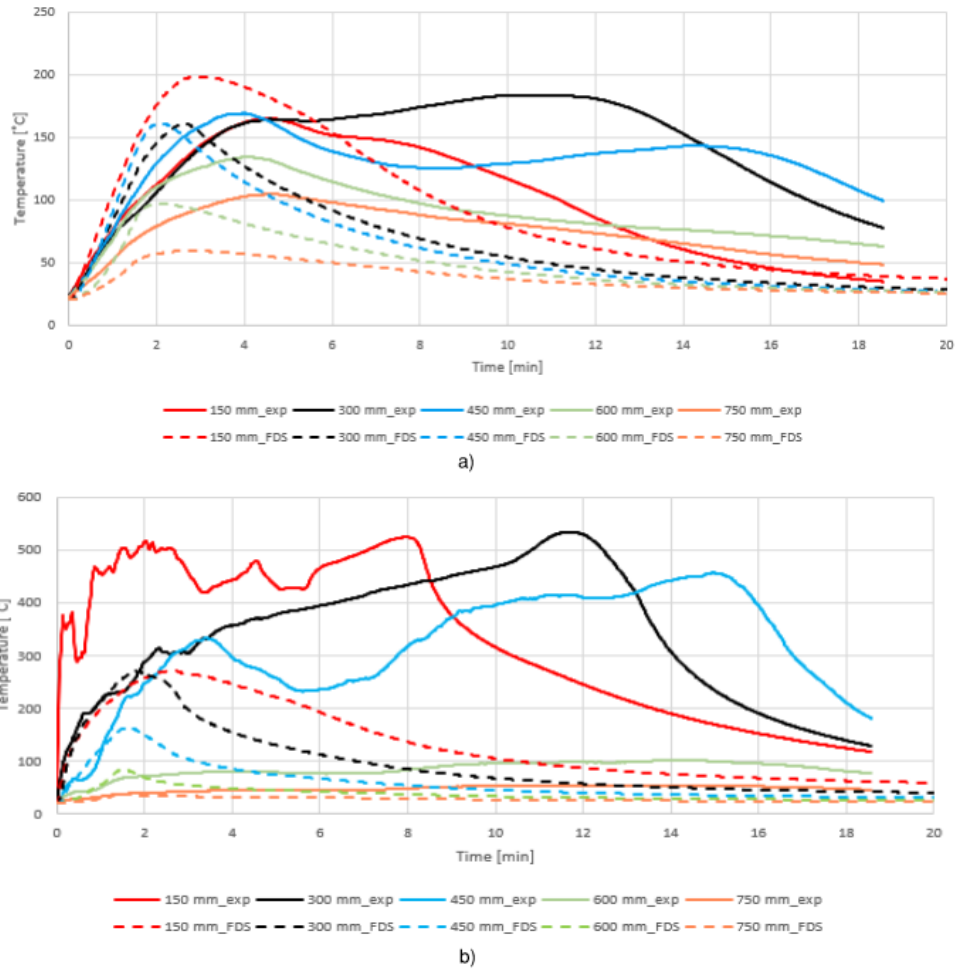


Figure 53: Comparison between FDS and small-scale experiments; a) temperature measurements on top of the PV module and b) temperature measurements on the roofing membrane. Temperature measurements made in the experiment are shown with solid lines, while dashed lines represent measurements made in FDS.

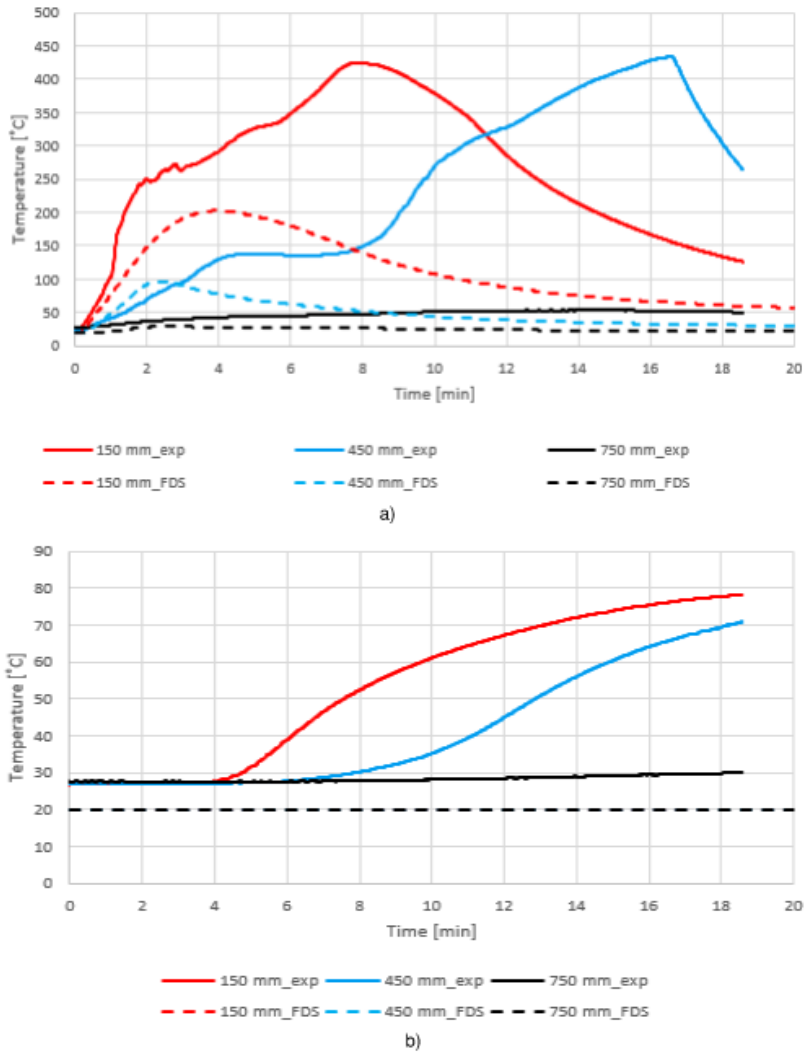


Figure 54: Comparison between FDS and small-scale experiments; a) temperature measurements on top of the chipboard and b) temperature measurements below the chipboard. Temperature measurements made in the experiment are shown with solid lines, while dashed lines represent measurements made in FDS.

4.4.2.2 Heat release rate

The modelling of the heat release rate seems to match very well with the cone calorimeter tests, as shown in Figure 55. The result may be an indication that the initial fire has been modelled correctly. The uncertainties in the setup of the FDS model appear to be other inputs such as the pyrolysis model and/or the chemical composition of the roofing membrane.

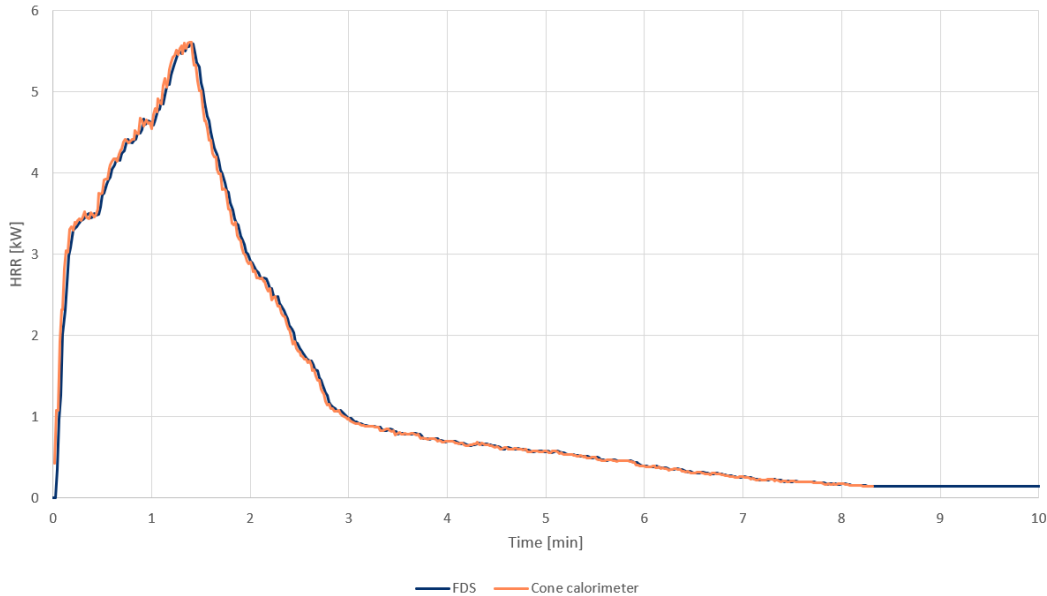


Figure 55: Comparison of HRR for EN-crib measured in FDS and cone calorimeter tests.

4.4.2.3 Temperature slices of the FDS model

A visual representation of fire development in FDS is shown in Figure 56, where temperature slices in the middle of the model are presented at different times. The way the flame adheres along the roof surface may indicate that the roofing membrane is pyrolyzing and contributing to the fire. Alternatively, this could be an optical illusion where one observes the effect of the roof construction's slope without the roofing membrane actually pyrolyzing/pyrolyzing sufficient. The illustrations mirror the results for temperature measurements where the fire has a positive development in the first 1,5 minutes before entering a decay phase. Figure 57, in comparison, shows images from the small-scale experiment T4. A similarity between FDS and the experiment is that the flame clings to the roof surface regardless of the PV module.

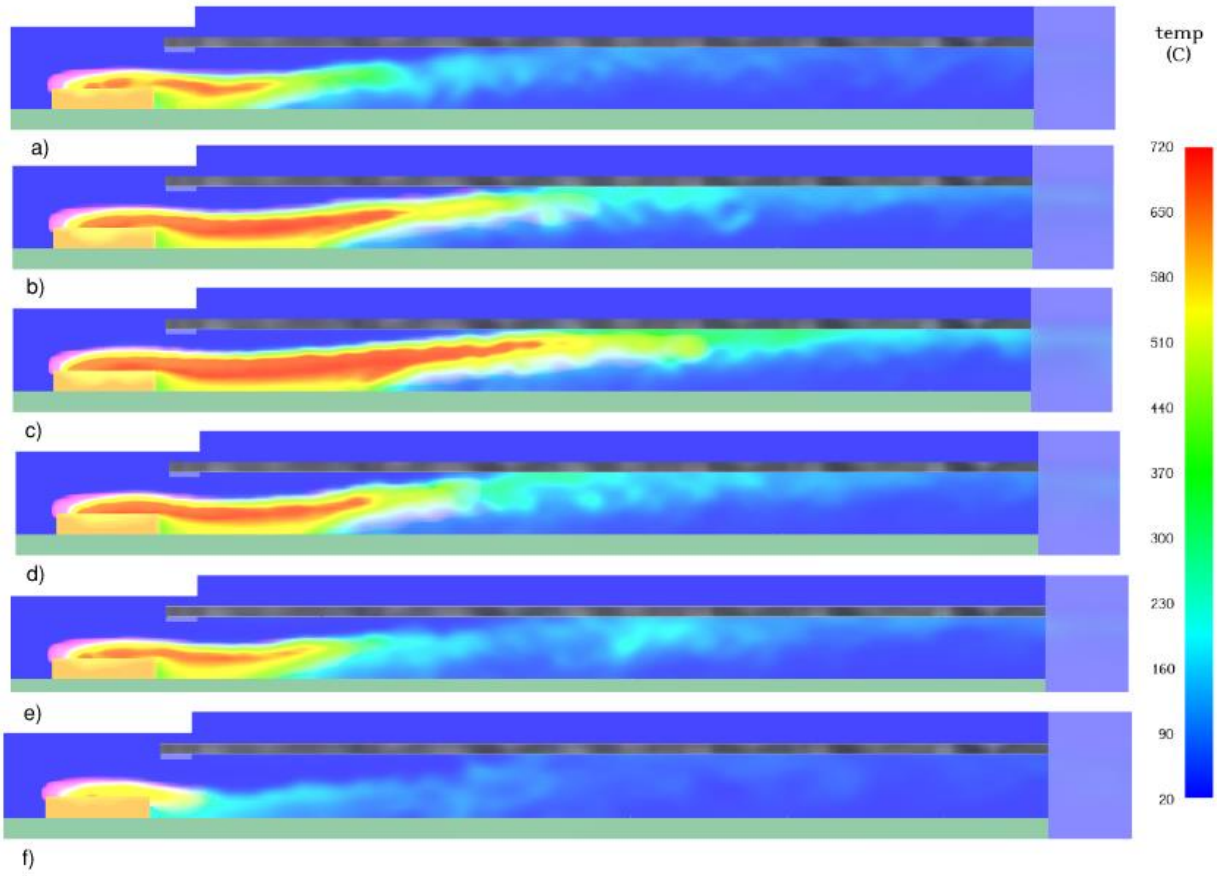


Figure 56: Temperature slices in the middle of the model presented at different times; a) 5 sec, b) 20 sec, c) 90 sec, d) 120 sec, e) 150 sec and f) 200 sec

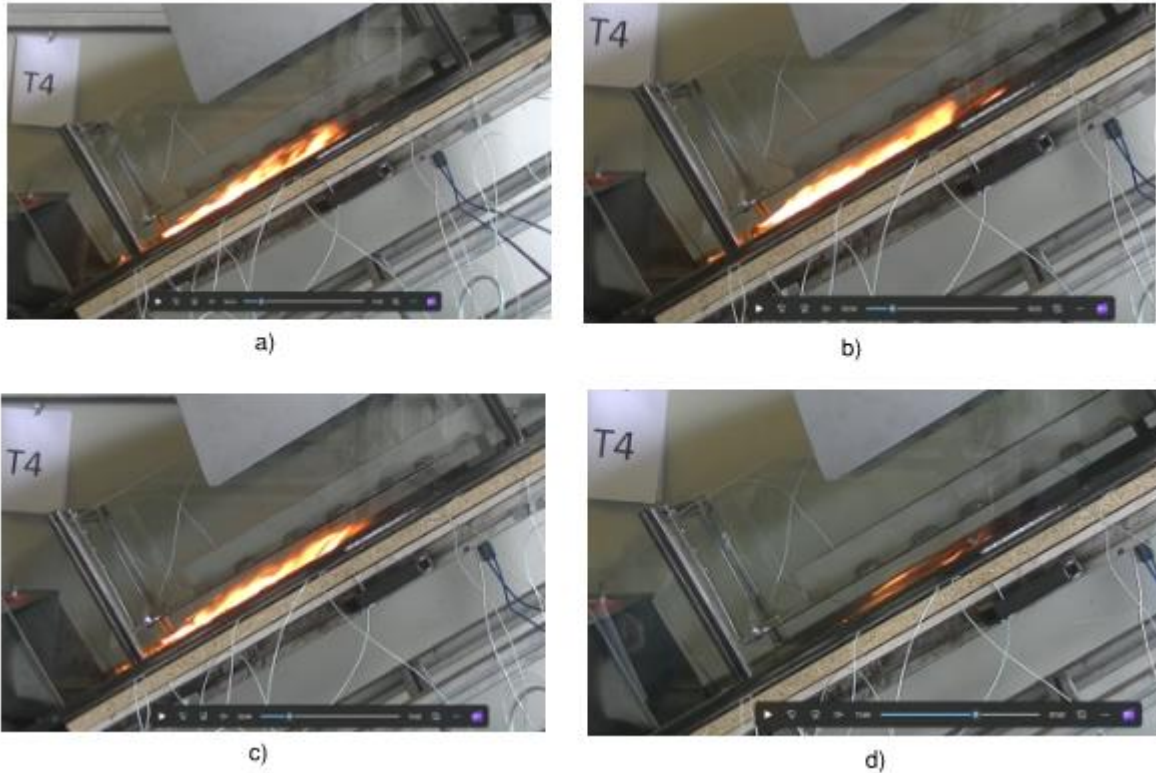


Figure 57: Small-scale experiment T4 with 2 m/s wind and 6 cm gap height between the PV module and roofing membrane, here shown; a) after 120 sec, b) 150 sec, c) 200 sec, and d) 480 sec

4.4.3 Parameter sensitivity analysis

It was decided to take a closer look at the uncertainties of the parameters reference temperature and pyrolysis range associated with the setup of the pyrolysis model for the roofing membrane. Reference temperature is what FDS designates as the temperature at which the mass fraction of the material decreases at its maximum rate. Pyrolysis range is used to fine tune the shape of the reaction curve, estimating over what temperature range the reaction takes place [55]. To assess the influence of these uncertainties on the accuracy of the simulation, a sensitivity analysis focusing on the various parameters was performed. A total of 5 simulations were conducted, all with a mesh cell size of 0,01m. The starting point for the parameters was a reference temperature of 450°C and a pyrolysis range of 200°C. The setup for the parameter sensitivity analysis can be seen in Table 18.

Table 18: Overview showing the setup of the parameter sensitivity analysis in FDS for the parameters reference temperature and pyrolysis range. The cell size of 0,01m remained the same in all analyses. The starting point for the parameters was a reference temperature of 450°C and a pyrolysis range of 200°C

Test ID	Cell size, δx [m]	Reference temperature [°C]	Pyrolysis range [°C]
FDS1	0,01	300	200
FDS2	0,01	350	200
FDS3	0,01	400	200
FDS4	0,01	450	300
FDS5	0,01	450	350

Figure 58 provides an illustrative overview of the temperature measurements from the parameter sensitivity analysis. The results are compared with measurements made in the small-scale experiment. Temperature measurements made in the experiment are shown with solid lines, while dashed lines represent measurements made in FDS. The exception is measurements of HRR where the orange line is data from the cone calorimeter test and the black line is data from FDS. Adjusting these two selected parameters is only estimated to affect the peak temperature in this specific setup. In particular, a change in reference temperature appears to have the greatest impact on peak temperature. An expected effect of lowering the reference temperature was an extension of the pyrolysis zone in the roofing membrane and the duration of the fire. This expectation cannot be said to be reflected in the temperature measurements.



Figure 58: Temperature measurements made in the experiment are shown with solid lines, while dashed lines represent measurements made in FDS. The exception is measurements of HRR where the orange line is data from the cone calorimeter test and the black line is data from FDS. The x-axis shows time (min) and the y-axis shows temperature (°C)/HRR (kW). Both x-axis and y-axis are common for all figures in the same column.

A comparison of the visual representation of fire development in FDS between the “main model” with mesh cell size 0,005m and ref. temp 450°C and the parameter sensitivity analysis with mesh cell size 0,01m and ref. temp 300°C is shown in Figure 59. Illustratively, one can see a higher temperature development and longer flame length for the simulation with the lower ref. temp. The fire in the model with the highest ref. temp starts the decay phase earlier than the fire in the model with the lower ref. temp. The visual representation also shows a significant difference in detail when halving the mesh cell size from 0,01m to 0,005m. Turbulence, smoke development, and the details of the flame itself are more prominently displayed with a finer mesh cell size.

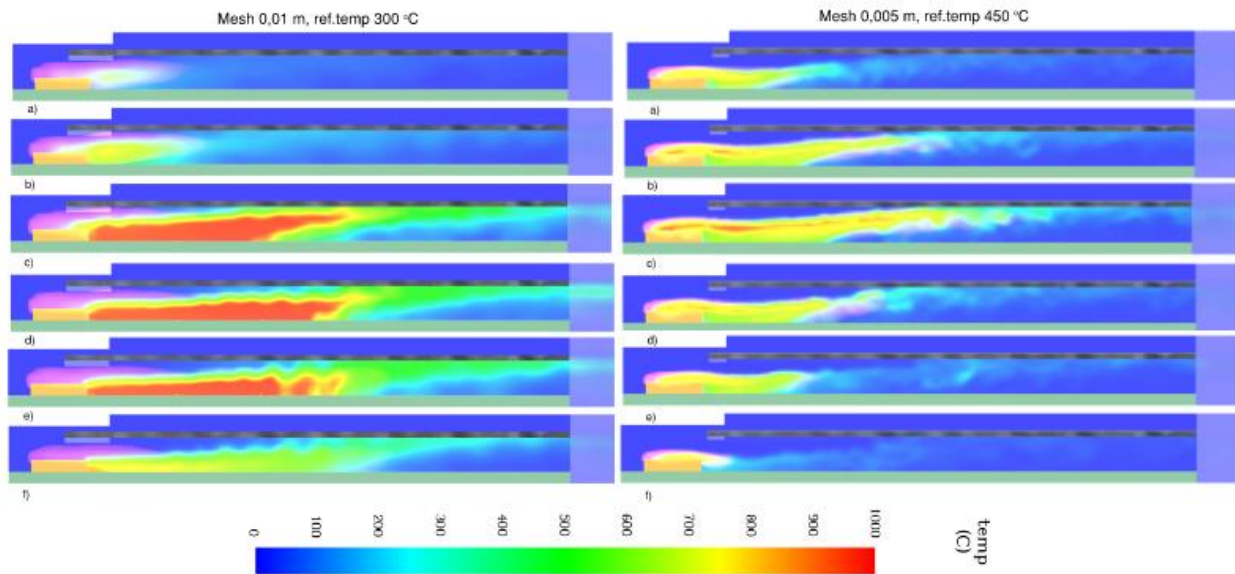


Figure 59: Comparison between the “main model” with mesh cell size 0,005 m and ref. temp 450 °C shown on the right side, and the sensitivity analysis with mesh cell size 0,01 m and ref. temp 300 °C shown on the left side. The remaining parameters and temperature scale is the same for both simulations. Temperature slices in the middle of the model presented at different times; a) 5 sec, b) 20 sec, c) 90 sec, d) 120 sec, e) 150 sec and f) 200 sec.

5. Discussion

This chapter will discuss the results described in Chapter 4; i) the medium- and full-scale experiments conducted in collaboration with RISE Fire Research, ii) wood crib burning experiments, iii) TGA experiment, and iv) the FDS simulations.

5.1 Experiments conducted in collaboration with RISE Fire Research

The medium-scale experiments studied the extent of damage, temperature development, and fire propagation in relation to different sizes of initial fire with both the presence and absence of a PV module. The experiences from the medium-scale experiments influenced the choice of the size of the initial fire used in the full-scale experiments. All experiments were conducted outdoors at RISE Fire Research facility in Trondheim in the autumn, a season where the weather in Norway can have large variations in terms of precipitation, temperature, and wind. The weather was generally stable and similar when the experiments were carried out. However, minor variations could potentially be a source of error in the comparison of the results.

5.1.1 Medium-scale experiments

The extent of damage from the 6 different test setups was the first visual aspect that researchers were introduced to when conducting the experiments. Figure 39 and Table 11 provide both an illustrative and quantitative description of the damage, where the greatest extent of damage was recorded in the test setups with PV modules and the initial fires UL B-crib and 3 x EN-crib. The remaining test setups caused very moderate damage localized to the roofing membrane near the initial fire. 3 x EN-crib and PV module resulted in a damage length of 70cm from the center of the wood crib before the fire extinguished itself, while UL B-crib and PV module led to damage from the center of the wood crib throughout the entire length of the test setup (150cm) in addition to flames being observed approximately 1 meter outside of the ridge. It is assumed that only the test setup with the PV module and UL B-crib would lead to further fire spread if the test rig was extended and the number of PV modules increased towards the ridge. Conducting only one experiment for each test setup is a weakness in terms of the reliability of the results as one cannot prove the validity of the experiments. The results can only be seen as indications and not exact results. However, it is possible to draw parallels to the small-scale experiments of Stølen et al. [3] which showed that the extent of damage did not increase significantly in test setups with 1 x EN-crib and both with the presence and absence of a PV module mounted 12cm above the roof surface. The parallel between small and medium-scale experiments can give an indication of a correlation between the height of the gap between the PV module and the roof surface set against the size of the initial fire. This is consistent with flame spread theory which describes among other things re-radiation and smoke accumulation under the PV module and the extension of the pyrolysis- pre-heating zone leading to extended fire spread.

Temperature measurements were only conducted in the last 4 test setups; one without a PV module and UL B-crib and three with PV module and initial fires UL B-crib, 1 x EN-crib, and 3 x EN-crib. All test setups

gave significant temperature measurements inward in the roof construction at the center under the initial fire. However, it was only the test setup with UL B-crib and PV module that gave significant temperature measurements 110cm from the initial fire in the direction of the ridge. The same also applies to temperature measurements made on top of the PV module. The results are consistent with the observations made for the extent of damage. The highest temperature measured on the underside of the chipboard was just under 100°C. Compared to the ignition temperature of wood (approx. 200°C [76]), the condition would not pose a risk of further fire spread inward in the construction when the starting point is a UL B-crib as the initial fire.

5.1.2 Full-scale experiments

Both test setups were similar except that experiment F2 had a steel gutter installed at the eaves and a smaller field extended at the centre of the ridge. Observations made in experiment F1 showed that melting roofing membrane with visible flames accumulated at ground level, which led the researchers to perform manual extinguishing with water to prevent the entire roof rig from igniting. The steel gutter in F2 was intended to collect melting roofing membrane to investigate whether the accumulation in the gutter would contribute to lateral fire spread and fire spread inward the construction at the eaves. In experiment F2, the temperature in the melted roofing membrane was not high enough for visible flames to be observed, and thus there was no fire spread in the eaves. It could have been of interest to conduct a similar experiment with a larger initial fire to see if melted roofing membrane could pose a real risk for lateral fire spread at the eaves, and whether this fire could take root in the roof construction leading to fire spread over the entire roof surface, not just centred. The extension of the roof construction had no further impact on the results. The indication can be seen in temperature measurements (Figure 42) performed at the measurement point 30cm above the top row of PV modules, only 50°C separates the experiments. It seems that the fire depends on protection/encapsulation for it to pose a greater risk of heat development both upwards along and inward in the construction.

Similar to the temperature measurements, it is observed that the fire has spread upwards along the construction all the way to the top, specifically along the centre and up towards the right. Even though the centre of the construction was extended in experiment F2, it is observed that the extent of the damage is not longer than for experiment F1. The damaged area to the right in the construction is somewhat a little wider for experiment F2 than F1. The temperature measurements were relatively similar in all parts of the construction in both experiments. Under the chipboard, the highest temperature measured was just under 120°C. Similar to the medium-scale test setup with UL B-crib and PV module, these conditions would also not pose a risk of further fire spread inward in the construction.

Along the centreline of the roof construction, under the top row of PV modules, a small area with scorch marks was observed on the OSB. The observation was made under the joint of two overlapping chipboards. It is assumed to have been a weakness in the joint, as the medium-scale experiments were conducted with board layers without a joint and no observations of scorch marks in the OSB. The same OSB were used in F2 without any further extent in scorch marks after the experiment ended. A possible explanation for the weakness in the joint could be errors in the researchers' assembly.

5.2 Wood burning experiments

Experiments were conducted on single EN-cribs and UL B-cribs to acquire data on HRR and MLR. Data from the experiments would subsequently be used in FDS simulations. In the study of the EN-crib, cone calorimeter tests were used. Both the mass and dimensions of the UL B-crib were too large to be accommodated by the cone calorimeter apparatus; therefore, free-burning tests in a well-ventilated indoor lab were conducted instead.

5.2.1 Cone calorimeter

A total of 3 cone calorimetry experiments on EN-cribs were conducted, where the average of the experiments resulted in a peak HRR measured at approximately 5,5kW after 1,5 minutes. There were no significant differences between the 3 experiments.

It was decided to run tests without walls (retainer) around the wood crib so that the wood crib had free access to oxygen from all sides except the bottom. This is similar to the test setup used in the small-scale experiments by Stølen et al. [3] except that the wood crib was exposed to a constant cone heat flux. Because the wood crib had no retainer, it lost fewer pieces along the way, an effect that can be particularly seen in the graphs for mass loss shown in Figure 48. The pieces fell off the scale, resulting in a significant mass loss within a remarkably brief time, or “peaks” as shown in the graphs.

5.2.2 Free burning

A series of 4 UL B-cribs were burned in a well-ventilated indoor lab. The ignition of the UL B-cribs was performed in the same manner as in the experiments conducted in Trondheim. By accident, the cribs for experiments FB3 and FB4 were dried for approximately 22 hours longer than for experiments FB1 and FB2. The extended drying time has possibly affected the initial weight shown in Table 15. The same can be said about the residual weight after the flames were self-extinguished. Here, there is significantly less remaining mass of FB3 and FB4. In addition to FB4 being conducted with free air access from the underside as well, it may be assumed that the amount of moisture in the cribs has an impact on these results. Since there were accidents related to the drying time of the wood cribs, in reality, there were a total of 3 test setups with few experiments conducted for each test setup. This is a weakness in terms of the reliability of the results as one cannot prove the validity of the experiments. The results can only be seen as indications and not exact results.

Between 54-98g of weight is lost in the 4 different experiments as a result of the ignition routine with a propane burner. This constitutes between 18,4-26,7% of the initial mass of the cribs. After the flames were self-extinguished and the tests were completed, the effect of the glowing wood pieces can also be observed. A total of 97,4-98,5% of the initial mass was lost until there was no more heat left in the embers. Figure 49 display the mass fraction and mass loss rate of the UL-B cribs. The outcomes of experiments FB1 and FB2 depict relatively similar graphs. In experiments FB3 and FB4, a notably greater mass loss is observed, particularly in FB4, which had free access to oxygen from the underside. The disparities between FB1/FB2 and FB3 might be attributed to a longer drying time, resulting in potentially reduced moisture in the FB3 crib, and therefore a greater mass loss rate.

5.3 Thermogravimetric analysis

The TGA experiments were conducted at the lab of Western Norway University of Applied Sciences. The TGA apparatus was new and expensive, and it was necessary to undergo a lengthy course with the manufacturer to operate the apparatus. The university's resources were very limited, and for that reason, only one experiment was conducted. This is a weakness in terms of the reliability of the results as one cannot prove the validity of the experiments. The results can only be seen as indications and not exact results.

Normally, the test sample is ground into dust/smaller particles, but the roofing membrane was too tough for this. Therefore, the roofing membrane was cut into smaller pieces and placed in a crucible. The impact of this on the results is uncertain, but it is a potential source of error.

The test started at 30°C and was carried out at a heating rate of 10K/min until the test ended at 800°C. Figure 50 illustrates the pyrolysis of Icopal Topsafe, which can be divided into four stages: i) From ambient temperature to 300°C where dW/dT equals 0, an indication of little chemical or physical reactions taking place. ii) From 300-450 °C where dW/dT changes from a steady value to a maximum and then 0. iii) From 510°C dW/dT is once a steady value of approx. 0 until iv) 690°C where dW/dT rapidly decreases to 800°C, where the test ended. It would be of interest to perform more TGAs of the roofing membrane with both different heating rates and a higher ending temperature than 800°C to study what appears to be a new stage in the pyrolysis, even though the highest temperature measured on the roofing membrane in full-scale experiments was just under 800°C, and hence it may not be of interest for this thesis to perform TGA with a higher temperature.

The residue yield from the TGA was 55%, which is considered a high value. It is difficult to estimate how much of the roofing membrane has pyrolyzed in the experiments, but it should be noted that a larger amount of waste from burned roofing membrane was observed after one of the full-scale experiments, shown in Figure 60. Additionally, there was melted roofing membrane on the ground that is not included in this collection of waste. The reason for the high percentage of residue yield could be that the roofing membrane is added a flame retardant. Without access to micro-scale calorimetry, it was not possible to say anything about the chemical formula of the roofing membrane. It was also not possible to obtain this information from the manufacturer either; email correspondence with Snorre Semmingsen, Product Approvals and Development Manager at BMI Norway (manufacturer of Icopal Topsafe), suggests that bitumen makes up approximately 60% of the composition of Icopal Topsafe [68].

It was desirable to perform cone calorimeter tests of the roofing in the HVL lab, but the person responsible for the lab did not want the roofing to be tested in the cone calorimeter apparatus as she was unsure and nervous that potentially sticky melted mass could potentially splatter in the test chamber and in the worst-case damage the machine. Testing the roofing membrane in the cone calorimeter was of interest as one could have used data from HRR to create a simple pyrolysis model in FDS. This was then not done.



Figure 60: Amount of scraped-off waste from burned roofing membrane after one of the full-scale experiments. Additionally, there was melted roofing membrane on the ground that is not included in this waste

5.4 Computational Fluid Dynamics Modelling

FDS is a sensitive tool that requires high accuracy of input for the output to be reliable.

To recreate the small-scale experiment (T4) by Stølen et al. [3], FDS was used as a simulation tool. The roof construction in the small-scale experiment had a similar setup and PV module as for the medium- and full-scale experiments, but the distance between the PV module and the roof surface was 6 cm, the initial fire was an EN-wood crib, and a fan provided a constant 2m/s wind at the eaves. Less computing power was required to simulate a complete test setup of this size compared to the medium- and full-scale experiments.

The use of wood cribs versus a gas burner in the small-scale experiment made it difficult to accurately reconstruct the initial fire in FDS. Lack of data on the material properties of the roofing membrane and the effect of the initial fire necessitated experiments in the HVL lab, where among other things cone calorimeter and TGA apparatus were used. The implementation and results from these experiments are described in earlier sub-chapters.

The geometry of the model follows the setup of the small-scale experiment conducted by Stølen et al. [3], with some minor but necessary adjustments to ensure that the dimensions of the materials align with the mesh grid size and its associated calculations performed in the domain. An overview of the adjustments between the small-scale experiment and FDS model geometry is shown in Table 8. With the available computing power and a mesh size of 5mm, the total computation time amounted to 9 days. Reducing the mesh size by a factor of 2 would result in approximately 16 times more computation time

[55], which would not have been feasible for this thesis. An adjustment worth mentioning is the simplification of the wood crib in FDS. As seen in Figure 33, method 3 has been selected, where a burner is applied to a vent and placed on top of the surface of an inert obstruction. When a wood crib is modelled in this manner, the burning time remains consistent, and it experience uniform combustion across its entire surface area post-ignition. If there's insufficient oxygen, the fire will decrease or even extinguish in real life, this is not the case for method 3 as the cribs burning time will still adhere to the pre-determined HRR. The inert obstruction will impede airflow through the object, which may affect the fire propagation upwards the roof construction. In addition, the inert object will impede conductive heat transfer from the fire to the roof construction. As a final result, the device for measuring temperature in the roof construction positioned closest to the fire will also be affected by the mentioned impediment.

For simplicity, it has been decided to limit the number of materials undergoing pyrolysis to wood and roofing membrane. In order to facilitate multiple reactions in a single simulation, complex stoichiometry must be specified. As a result, the oxidation interaction between fuel and air needs to be clearly defined. The combustion process was modelled as a single-step reaction of $C_6H_{10}O_5$ (spruce) and $C_{50}H_{48}O_4$ (bitumen) [73] p. 5 figure 2. The molecular formula for bitumen was used in lack of micro-scale calorimetry to assess to correct formula for Icopal Topsafe.

Choosing the single-reaction scheme for pyrolysis modelling of wood brings with it uncertainties due to the model's simplifications and assumptions. By reducing the pyrolysis process to a single reaction, the scheme might not adequately represent the intricate reactions involved in decomposition of wood components like hemicellulose, cellulose, and lignin. The chipboards used in the roof construction also contain components beyond just wood [67]; water, glue, paraffin wax, ammonia, ammonium nitrate, and urea.

It was decided to take a closer look at the uncertainties of the parameters reference temperature and pyrolysis range associated with the setup of the pyrolysis model for the roofing membrane. Reference temperature is what FDS designates as the temperature at which the mass fraction of the material decreases at its maximum rate. Pyrolysis range is used to fine tune the shape of the reaction curve, estimating over what temperature range the reaction takes place [55]. To assess the influence of these uncertainties on the accuracy of the simulation, a sensitivity analysis focusing on the various parameters was performed. A total of 5 simulations were conducted, all with a mesh cell size of 0,01m. The starting point for the parameters was a reference temperature of 450°C and a pyrolysis range of 200°C. The setup for the parameter sensitivity analysis can be seen in Table 18. Figure 58 provides an illustrative overview of the temperature measurements from the parameter sensitivity analysis. The results are compared with measurements made in the small-scale experiment. Adjusting these two selected parameters is only estimated to affect the peak temperature in this specific setup. In particular, a change in reference temperature appears to have the greatest impact on peak temperature. An expected effect of lowering the reference temperature was an extension of the pyrolysis zone in the roofing membrane and the duration of the fire. This expectation cannot be said to be reflected in the temperature measurements.

Comparison of temperatures measured in the different layers of the construction and on top of the PV module between FDS and small-scale experiment is shown in Figure 53 and Figure 54. From the modelling of the initial fire, there has been observed a rapid increase in total HRR from 0-1,5 minutes, after which there is a relatively steep decrease until 3 minutes where the curve flattens out. This is also somewhat reflected in the curves of FDS, where temperatures early in the fire development (approx. 0-2 min) show a tendency to follow the temperature curves of the small-scale experiment, but quickly enter the decay phase. It is speculated whether the roofing membrane does not pyrolyze enough in FDS for the fire development to become more similar to the experiment. Most results seem to indicate that the contribution from the roofing membrane was greater in the experiment than in FDS.

6. Conclusion

Based on the findings in this thesis, it has been chosen to answer the research questions in the following way:

Research Question 1: *How is a typical $B_{Roof}(t_2)$ [4] roof construction affected by a realistic firebrand when the roof construction has parallel-mounted mock-up BAPVs?*

- *Sub-question 1-1: What size must the initial fire (realistic firebrand) be for the fire to develop and propagate in the cavity between the PV module(s) and the roof construction?*
- *Sub-question 1-2: What temperatures are measured in the different layers of the roof construction and on the PV modules?*
- *Sub-question 1-3: What is the extent of damage in the different layers of the roof construction?*

In the medium and full-scale experiments, it has been shown that the size of the initial fire must be at least as large as a UL B-crib when the distance between the PV module and the roof surface is 12cm, for a fire to develop along the roof surface. The highest temperature along the roof surface in the full-scale experiment was measured to just under 800°C, but temperatures measured inward in the construction indicate that there would not be a risk of further fire spread where the highest temperature was measured to just under 120°C under the chipboard. The extent of damage in the full-scale experiments was primarily observed in the center of the roof construction where the initial fire was also located, in addition to the damaged area spreading outwards on the right side from about the middle of the construction towards the ridge. No damage was observed deeper into the roof construction than the chipboards.

In conclusion, it can be stated that there is a correlation between the height of the gap between the PV module and the roof surface set against the size of the initial fire.

Research Question 2: *Can the results of Stølen et al. [3] small-scale experiment T4 be recreated using CFD?*

- *Sub-question 2-1: To what degree of accuracy can the initial fire used in small-scale experiments be recreated using cone calorimetry, to then use these data as one of several parameters in the CFD model?*
- *Sub-question 2-2: To what degree of accuracy can the pyrolysis of the roofing membrane used in small-scale experiments be recreated in the CFD model using TGA, as one of several parameters?*
- *Sub-question 2-3: What is the CFD model's level of accuracy to small-scale experimental data?*

In the comparison between the results from CFD and the small-scale experiment, one can see an indication of a correlation between data from cone calorimetry tests and the initial fire in the experiment.

Too many sources of error and uncertain parameters resulted in the attempt to recreate the small-scale experiment using CFD not yielding satisfactory results. Particularly significant uncertainty is associated with the pyrolysis model of the roofing membrane.

7. Further work

This chapter will provide suggestions on further research:

- The fire department occasionally conducts fire drills on existing buildings. In collaboration with the fire department, one can mount mock-up PV modules on the roof construction and conduct similar full-scale experiments as this thesis in collaboration with RISE Fire Research, where one refrains from extinguishing any fire in the roof's edge, to closely observe the fire development in this part of the construction. In such a setup, there would also be a realistic wind profile, unlike the experiments at RISE Fire Research where the roof construction was placed on the ground.
- Further research on the inherent fire energy in a PV module.
- Work on implementing pre-accepted solutions for roof constructions with PV modules in Norwegian building codes.
- Work on developing a European/international standard that describes the test setup for roof construction with PV modules.
- Use micro-scale calorimetry for further research on the material properties of the roofing membrane, to further improve/detail the pyrolysis model used in FDS.
- Using a gas burner with known heat flux instead of wood cribs will make it easier to recreate the experiments, especially when modelling in FDS.
- Conduct further parameter sensitivity analysis in the FDS model to identify errors in the setup.
- Conduct cone calorimeter tests of the roofing membrane and use HRR data from these tests to create a simple pyrolysis model in FDS.

8. References

- [1] International Energy Agency (IEA), 'Renewables 2020 - Analysis and forecast to 2025', Paris, 2020. [Online]. Available: https://iea.blob.core.windows.net/assets/1a24f1fe-c971-4c25-964a-57d0f31eb97b/Renewables_2020-PDF.pdf
- [2] R. Stølen, R. F. Mikalsen, and J. P. Stensaas, 'Solcelleteknologi og brannsikkerhet', 2018. doi: 10.13140/RG.2.2.14533.50401.
- [3] R. Stølen, J. S. Fjærstad, and R. F. Mikalsen, 'EBOB – Solcelleinstallasjoner på bygg. Eksperimentell studie av brannspreiing i holrom bak solcellemodular på skrå takflater', 2022. doi: 10.13140/RG.2.2.34287.92326.
- [4] 'Test methods for external fire exposure to roofs', *SN-CEN/TS 1187:2012*. European Committee for Standardization, 2012.
- [5] Direktoratet for byggkvalitet (DiBK), 'Veiledning om tekniske krav til byggverk (VTEK17)'. 2017. [Online]. Available: <https://www.dibk.no/regelverk/byggteknisk-forskrift-tek17>
- [6] 'Standard Test Methods for Fire Tests of Roof Coverings', *UL790*. Underwriters Laboratories, Apr. 22, 2004.
- [7] N. A. F. Mohd Nizam Ong, M. A. Sadiq, M. S. Md Said, G. Jomaas, M. Z. Mohd Tohir, and J. S. Kristensen, 'Fault tree analysis of fires on rooftops with photovoltaic systems', *Journal of Building Engineering*, vol. 46, Apr. 2022, doi: 10.1016/j.jobbe.2021.103752.
- [8] 'External fire exposure to roofs in combination with photovoltaic (PV) arrays - Test method(s)', *NEK CLC/TR 50670:2016*. Norsk Elektroteknisk Komité (NEK), Jan. 02, 2017.
- [9] Standard Norge, 'Teknisk Rapport (Technical Report/TR)'. Accessed: Dec. 16, 2023. [Online]. Available: <https://standard.no/standardisering/leveranser/teknisk-rapport/>
- [10] R. F. Mikalsen, J. S. Fjærstad, S. Fjaerestad, R. Stølen, and O. A. Holmvaag, 'EBOB – Solcelleinstallasjoner på bygg. Brannspredning og sikkerhet for brannvesen', Trondheim, 2022. doi: 10.13140/RG.2.2.32610.20165.
- [11] BMI Group, 'Icopal TopSafe', *Teknisk datablad*. 2022. Accessed: Jan. 09, 2023. [Online]. Available: <https://bmipimngprodftfe.azureedge.net/sys-master-hybris-media/h4c/h85/9064310210590/TDS-Icopal-TopSafepdf>
- [12] V. Masson-Delmotte and Intergovernmental Panel on Climate Change (IPCC). Working Group I, *Climate change 2021: the physical science basis: Working Group I contribution to the Sixth Assessment Report of the Intergovernmental Panel on Climate Change*, 1st ed. Cambridge: Cambridge University Press, 2023. Accessed: Apr. 17, 2023. [Online]. Available: https://report.ipcc.ch/ar6/wg1/IPCC_AR6_WGI_FullReport.pdf
- [13] United Nations Department of Economics and Social Affairs (UN DESA), 'Growing at a slower pace, world population is expected to reach 9.7 billion in 2050 and could peak at nearly 11 billion around 2100'. Accessed: Nov. 15, 2021. [Online]. Available:

<https://www.un.org/development/desa/en/news/population/world-population-prospects-2019.html>

- [14] L. Fernández, 'Cumulative installed solar PV capacity worldwide from 2000 to 2022', Statista. Accessed: Nov. 19, 2023. [Online]. Available: <https://www.statista.com/statistics/280220/global-cumulative-installed-solar-pv-capacity/>
- [15] J. Toothman and S. Aldous, 'How Solar Cells Work', How Stuff Works. Accessed: Nov. 28, 2021. [Online]. Available: <https://science.howstuffworks.com/environmental/energy/solar-cell.htm>
- [16] U.S. Department of Energy (DOE), 'Solar Photovoltaic Cell Basics'. Accessed: Nov. 28, 2021. [Online]. Available: <https://www.energy.gov/eere/solar/solar-photovoltaic-cell-basics>
- [17] G. Masson and I. Kaizuka, *Trends in Photovoltaic Applications 2020*. International Energy Agency (IEA), 2020. [Online]. Available: https://iea-pvps.org/wp-content/uploads/2020/11/IEA_PVPS_Trends_Report_2020-1.pdf
- [18] N. K. Rossing, P.-T. Storli, S. Völler, and T. Fagerli, 'Fornybar energi', Trondheim, Mar. 2020. [Online]. Available: <https://www.ntnu.no/documents/2004699/12108297/Fornybar+energi.pdf/14a619fe-9791-484a-a65c-20448b15bbd8?t=1574251361765>
- [19] U.S Energy Information Administration (EIA), 'Solar explained - Photovoltaics and electricity'. Accessed: Nov. 28, 2021. [Online]. Available: <https://www.eia.gov/energyexplained/solar/photovoltaics-and-electricity.php>
- [20] D. De Rooij, 'How do TPT, PVF and PET compare to each other?', Sinovoltaics Group Limited. Accessed: Dec. 18, 2021. [Online]. Available: <https://sinovoltaics.com/learning-center/materials/tpt-pvf-and-pet/>
- [21] H.-Y. Yang, X.-D. Zhou, L.-Z. Yang, and T.-L. Zhang, 'Experimental studies on the flammability and fire hazards of photovoltaic modules', *Materials*, vol. 8, no. 7, pp. 4210–4225, Jul. 2015, doi: 10.3390/ma8074210.
- [22] K. Sander *et al.*, 'Studie zur entwicklung eines rücknahme- und verwertungssystem für photovoltaische produkte', Hamburg, Nov. 2007. [Online]. Available: https://epub.sub.uni-hamburg.de/epub/volltexte/2012/12655/pdf/Gesamtbericht_PVCycle_de.pdf
- [23] N. W. van Veen, M. G. Mennen, P. M. J. Bos, T. W. J. A. Engering, A. Gressen, and J. J. P. Lasaroms, 'Schadelijke stoffen bij branden met zonnepanelen', Bilthoven, 2022. doi: 10.21945/RIVM-2022-0103.
- [24] J. S. Kristensen, B. Merci, and G. Jomaas, 'Fire-induced re-radiation underneath photovoltaic arrays on flat roofs', *Fire Mater*, vol. 42, no. 9, pp. 34–43, 2017, doi: 10.1002/fam.2494.
- [25] J. S. Kristensen, F. B. M. Faudzi, and G. Jomaas, 'Experimental study of flame spread underneath photovoltaic (PV) modules', *Fire Saf J*, vol. 120, no. 9, 2021, doi: 10.1016/j.firesaf.2020.103027.

- [26] X. Ju, X. Zhou, K. Zhao, F. Peng, and L. Yang, 'Experimental study on fire behaviors of flexible photovoltaic panels using a cone calorimeter', *J Fire Sci*, vol. 36, no. 1, pp. 63–77, Jan. 2018, doi: 10.1177/0734904117740855.
- [27] L. Yin, Y. Jiang, and R. Qiu, 'Combustion Behaviors of CIGS Thin-Film Solar Modules from Cone Calorimeter Tests', *Materials*, vol. 11, no. 8, p. 1353, Aug. 2018, doi: 10.3390/ma11081353.
- [28] J. S. Kristensen, 'Fire risk assessment of solar cell array installations on large buildings. How to protect the building in case of fire?' Kongens Lyngby, 2015.
- [29] B. C. Hagen, *Grunnleggende brannteknikk*, 2nd ed. Haugesund: B.C. Hagen, 2018.
- [30] G. Jomaas, 'Fundamentals of Premixed Flames', in *SFPE Handbook of Fire Protection Engineering*, 5th ed., vol. 1, M. J. Hurley, Ed., New York: Springer, 2016, pp. 373–395. doi: 10.1007/978-1-4939-2565-0.
- [31] F. A. Williams, 'Mechanisms of fire spread', *Symposium (International) on Combustion*, vol. 16, no. 1, pp. 1281–1294, 1977, doi: 10.1016/S0082-0784(77)80415-3.
- [32] S. R. Ray, A. C. Fernandez-Pello, and I. Glassmann, 'A Study of the Heat Transfer Mechanisms in Horizontal Flame Propagation', *ASME Journal of Heat and Mass Transfer*, vol. 102, no. 2, pp. 357–363, May 1980, doi: 10.1115/1.3244288.
- [33] R. Friedman, 'Ignition and Burning of Solids', *Symposia Paper*, pp. 91–111, Jan. 1976, doi: 10.1520/STP37204S.
- [34] J. S. Kristensen and G. Jomaas, 'Experimental Study of the Fire Behaviour on Flat Roof Constructions with Multiple Photovoltaic (PV) Panels', *Fire Technol*, vol. 54, no. 2, pp. 1807–1828, 2018, doi: 10.1007/s10694-018-0772-5.
- [35] J. S. Kristensen, B. Jacobs, and G. Jomaas, 'Experimental Study of the Fire Dynamics in a Semi-enclosure Formed by Photovoltaic (PV) Installations on Flat Roof Constructions', *Fire Technol*, vol. 58, pp. 2017–2054, Mar. 2022, doi: 10.1007/s10694-022-01228-z.
- [36] F. Tang *et al.*, 'Experimental study and analysis of radiation heat fluxes received by a floor beneath an inclined ceiling', *Fire Mater*, vol. 45, no. 2, pp. 205–214, Oct. 2021, doi: 10.1002/fam.2925.
- [37] Y. Hasemi, 'Surface Flame Spread', in *SFPE Handbook of Fire Protection*, 5th ed., vol. 1, M. J. Hurley, Ed., New York: Springer, 2016, pp. 705–723. doi: 10.1007/978-1-4939-2565-0.
- [38] F. Morandini, P. A. Santoni, and J. H. Balbi, 'Fire Front Width Effects on Fire Spread Across a Laboratory Scale Sloping Fuel Bed', *Combustion Science and Technology*, vol. 166, no. 1, pp. 67–90, Mar. 2001, doi: 10.1080/00102200108907820.
- [39] P. J. Woodburn and D. D. Drysdale, 'Fires in inclined trenches: the dependence of the critical angle on the trench and burner geometry', *Fire Saf J*, vol. 31, no. 2, pp. 143–164, Dec. 1998, doi: 10.1016/S0379-7112(98)00004-6.

- [40] L. Orloff, J. De Ris, and G. H. Markstein, 'Upward turbulent fire spread and burning of fuel surface', *Symposium (International) on Combustion*, vol. 15, no. 1, pp. 183–192, Jan. 1975, doi: 10.1016/S0082-0784(75)80296-7.
- [41] D. D. Drysdale and A. J. R. Macmillan, 'Flame spread on inclined surfaces', *Fire Saf J*, vol. 18, no. 3, pp. 245–254, Jan. 1992, doi: 10.1016/0379-7112(92)90018-8.
- [42] R. L. Alpert, 'Ceiling Jet Flows', in *SFPE Handbook of Fire Protection Engineering*, 5th ed., vol. 1, M. J. Hurley, Ed., New York: Springer, 2016, pp. 429–454. doi: 10.1007/978-1-4939-2565-0.
- [43] J. G. Quintiere, 'The Application of Flame Spread Theory to Predict Material Performance', *J Res Natl Bur Stand (1934)*, vol. 93, no. 1, pp. 61–70, 1988, doi: 10.6028/jres.093.007.
- [44] D. D. Drysdale, 'Thermochemistry', in *SFPE Handbook of Fire Protection Engineering*, 5th ed., vol. 1, M. J. Hurley, Ed., New York: Springer, 2016, pp. 138–150. doi: 10.1007/978-1-4939-2565-0.
- [45] P. H. Thomas, 'Factors affecting ignition of combustible materials and their behavior in fire', *International Symposium on Fire Safety of Combustible Materials*, pp. 84–99, 1975.
- [46] S. Loganathan, R. B. Valapa, R. K. Mishra, G. Pugazhenth, and S. Thomas, 'Thermogravimetric Analysis for Characterization of Nanomaterials', *Thermal and Rheological Measurement Techniques for Nanomaterials Characterization*, vol. 3, pp. 67–108, Jan. 2017, doi: 10.1016/B978-0-323-46139-9.00004-9.
- [47] A. Witkowski, A. A. Stec, and T. Ri. Hull, 'Thermal Decomposition of Polymeric Materials', in *SFPE Handbook of Fire Protection Engineering*, 5th ed., vol. 1, M. J. Hurley, Ed., New York: Springer, 2016, pp. 167–254. doi: 10.1007/978-1-4939-2565-0.
- [48] J.-S. Gong, F. Wei-Biao, and Z. Bei-Jing, 'A study on the pyrolysis of asphalt', *Fuel*, vol. 82, no. 1, pp. 49–52, Jan. 2003, doi: 10.1016/S0016-2361(02)00136-9.
- [49] NETZSCH-Gerätebau GmbH, 'Model-Based (Model Fitting) Analysis Method'. Accessed: Nov. 13, 2023. [Online]. Available: <https://kinetics.netzsch.com/en/features/model-based-analysis>
- [50] 'Standard Test Method for Heat and Visible Smoke Release Rates for Materials and Products Using an Oxygen Consumption Calorimeter', *ASTM E1354:23*. American Society for Testing and Materials (ASTM), 2023. [Online]. Available: <https://www.astm.org/e1354-23.html>
- [51] 'Reaction to fire tests- Heat release, smoke production and mass loss rate - Part 1: Heat release rate (cone calorimeter method) and smoke production rate (dynamic measurement)', *ISO 5660-1*. Standard Norge, 2015. [Online]. Available: <https://online.standard.no/iso-5660-1-2015-3>
- [52] M. Janssens, 'Calorimetry', in *SFPE Handbook of Fire Protection Engineering*, 5th ed., vol. 1, M. J. Hurley, Ed., New York: Springer, 2016, pp. 905–951.
- [53] 'Reaction-to-fire tests — Heat release, smoke production and mass loss rate — Part 2: Smoke production rate (dynamic measurement)', *ISO 5660-2:2002*. Standard Norge, 2002. [Online]. Available: <https://online.standard.no/iso-5660-2-2002>

- [54] K. McGrattan and S. Miles, 'Modeling Fires Using Computational Fluid Dynamics (CFD)', in *SFPE Handbook of Fire Protection Engineering*, 5th ed., vol. 1, M. J. Hurley, Ed., New York: Springer, 2016, pp. 1034–1065.
- [55] K. McGrattan, R. MvDermott, M. Vanella, S. Hostikka, and J. Floyd, 'Fire dynamics simulator User's Guide'. [Online]. Available: <https://nvlpubs.nist.gov/nistpubs/Legacy/SP/nistspecialpublication1019.pdf>
- [56] K. McGrattan, R. McDermott, C. Weinschenk, K. Overholt, S. Hostikka, and J. Floyd, 'Fire Dynamics Simulator Technical Reference Guide Volume 1: Mathematical Model'. Accessed: Apr. 09, 2023. [Online]. Available: <https://nvlpubs.nist.gov/nistpubs/SpecialPublications/NIST.SP.1018e6.pdf>
- [57] J. S. Kristensen, 'Photovoltaic installations on warehouse buildings – an experimental study of the propagation of fire', Master of Science in Engineering, Technical University of Denmark, Kongens Lyngby, 2016.
- [58] 'Fire classification of construction products and building elements. Part 5: Classification using data from external fire exposure to roof tests', *NS-EN 13501-5:2016*. European Committee for Standardization, 2016.
- [59] A.-J. Enstad, 'SINTEF Produktsertifikat Nr. 1738 - Icopal TopSafe', 2023. [Online]. Available: <https://www.sintefcertification.no/product/index/2634>
- [60] H. B. Skogstad, 'SINTEF Teknisk Godkjenning TG 2280 - Forestia Gulv og Taktro sponplater', 2021. [Online]. Available: <https://www.sintefcertification.no/product/index/272>
- [61] B. Backstrom and D. Sloan, 'Characterization of Photovoltaic Materials – Critical Flux for Ignition/Propagation - Phase 3', Northbrook, 2012.
- [62] B. Backstrom, D. Sloan, and P. Gandhi, 'Effect of Rack Mounted Photovoltaic Modules on the Fire Classification Rating of Roofing Assemblies Phase 2', Northbrook, 2012.
- [63] D. Gross, 'Experiments on the Burning of Cross Piles of Wood', *JOURNAL OF RESEARCH of the National Bureau of Standards-C. Engineering and Instrumentation*, vol. 66C, no. 2, pp. 99–105, Jan. 1962.
- [64] 'Thermal analysis (TA) - Thermogravimetry (TG) - Principles', *DIN 51006:2005-07*. Deutsches Institut für Normung e. V. (DIN), 2005. doi: 10.31030/9636904.
- [65] NETZSCH-Gerätebau GmbH, 'Simultaneous Thermal Analyzer – STA 449 F3 Jupiter'. Accessed: May 04, 2023. [Online]. Available: https://analyzing-testing.netzsch.com/_Resources/Persistent/6/b/7/4/6b74b138b6dc4aee6d104a4f385a1ba8638e124f/STA_449_F3_Jupiter_en_web.pdf
- [66] A. Rinta-Paavola and S. Hostikka, 'A model for the pyrolysis of two Nordic structural timbers', *Fire Mater*, vol. 46, no. 1, pp. 55–68, Jan. 2022, doi: 10.1002/fam.2947.
- [67] The Norwegian EPD Foundation, 'Environmental Productin Declaration - Forestia Sponplater Standard', Oslo, 2020. [Online]. Available: https://pro.forestia.com/media/6031/nepd-2001-885_forestia-sponplater-standard_en.pdf

- [68] S. Semmingsen, 'Personal communication'. Dec. 13, 2022.
- [69] D. Drysdale, *An Introduction to Fire Dynamics*, 3rd ed. John Wiley & Sons, Ltd, 2011. doi: 10.1002/9781119975465.
- [70] B. Fredlund, 'A model for heat and mass transfer in timber structures during fire: a theoretical, numerical and experimental study', Doctoral Thesis, Lund University, Lund, 1988.
- [71] M. D. Granum, 'Computational modelling of enclosure fires with exposed timber surfaces', Master Thesis in Fire Safety Engineering, Western Norway University of Applied Sciences, Haugesund, 2023.
- [72] H. Y. Zhao, Y. Cao, S. P. Sit, Q. Lineberry, and W. P. Pan, 'Thermal characteristics of bitumen pyrolysis', *J Therm Anal Calorim*, vol. 107, no. 2, pp. 541–547, May 2012, doi: 10.1007/s10973-011-1590-x.
- [73] Z. Zhang, N. Kang, J. Zhou, X. Li, L. He, and H. Sui, 'Novel synthesis of choline-based amino acid ionic liquids and their applications for separating asphalt from carbonate rocks', *Nanomaterials*, vol. 9, no. 4, Apr. 2019, doi: 10.3390/nano9040504.
- [74] D. T. Gottuk and B. Y. Lattimer, 'Effect of Combustion Condition on Species Production', in *SFPE Handbook of Fire Protection Engineering*, 5th ed., vol. 1, M. J. Hurley, Ed., New York: Springer, 2016, pp. 486–528.
- [75] V. Kurian, 'Asphaltene Gasification: Soot Formation and Metal Distribution', Doctor of Philosophy in Chemical Engineering, University of Alberta, 2016.
- [76] V. Babrauskas, 'Ignition of wood: A review of the state of the art', *Journal of Fire Protection Engineering*, vol. 12, no. 3, pp. 163–189, 2002, doi: 10.1177/10423910260620482.
- [77] F. Nystedt and H. Frantzich, 'Kvalitetsmanual för brandtekniska analyser vid svenska kärntekniska anläggningar', Lund, Jan. 2011.
- [78] R. Stølen, 'Personal communication'. Nov. 06, 2023.

9. Appendix

Appendix A – FDS mesh calculations

This appendix provides hand calculations for determining the mesh cell size in the FDS model.

Fire diameter, D

The area of the burner/source of fire is set to $0,01\text{m}^2$. By assuming the fire has a circular geometry, the diameter of the fire is calculated as follow:

$$A_{fire} = \pi r^2 = \left(\frac{\pi}{4}\right) \cdot D^2$$

$$D = \sqrt{\frac{4 \cdot A}{\pi}} = \sqrt{\frac{4 \cdot 0,01 \text{ m}^2}{\pi}} \approx 0,11 \text{ m}$$

Characteristic HRR, Q^*

Data from cone calorimeter tests of EN-cribs gives HRR $\dot{Q} = 5,6038076\text{kW}$. The characteristic HRR Q^* is calculated as follow:

$$Q^* = \frac{\dot{Q}}{\rho_{\infty} C_p T_{\infty} \sqrt{g} \cdot D \cdot D^2}$$

$$Q^* = \frac{5,6038076 \text{ kW}}{1,2 \frac{\text{kg}}{\text{m}^3} \cdot 1,0 \text{ kJ/kgK} \cdot 293 \text{ K} \cdot \sqrt{9,81 \frac{\text{m}}{\text{s}^2}} \cdot 0,11 \text{ m} \cdot (0,11 \text{ m})^2} \approx 1,27$$

Nystedt and Frantzich [77] states that Q^* should be in the range of 0,3 to 2,5. Calculated value of 1,27 is ok.

Characteristic fire diameter, D^*

$$D^* = \left(\frac{\dot{Q}}{\rho_{\infty} C_p T_{\infty} \sqrt{g}} \right)^{\frac{2}{5}}$$

$$D^* = \left(\frac{5,6038076 \text{ kW}}{1,2 \frac{\text{kg}}{\text{m}^3} \cdot 1,0 \text{ kJ/kgK} \cdot 293 \text{ K} \cdot \sqrt{9,81 \frac{\text{m}}{\text{s}^2}}} \right)^{\frac{2}{5}} \approx 0,12$$

The number of computational cells spanning the characteristic fire diameter, $D^*/\delta x$

Cell size, δx [m]	$D^*/\delta x$	Number of cells
0,02	6	9840
0,01	12	51 120
0,005	24	382 080

Nystedt and Frantzich [77] states that $D^*/\delta x$ should be in the range of 10-20 in the near area of the fire.

Appendix B – FDS script

This appendix provides the FDS script used for simulating the results presented in chapter 4.4.2

```
&HEAD CHID='Flat'/
&TIME T_END=1200.0/
&DUMP DT_RESTART=60.0, DT_SL3D=0.25/
&MISC GVEC=-4.905,0.0,-8.495709/
&WIND SPEED=2.0/

&MESH ID='MESH-01-01', IJK=36,20,24, XB=0.0,0.18,1.9,2.0,5.0E-3,0.125/
&MESH ID='MESH-01-02-01-01', IJK=18,20,20, XB=0.0,0.09,2.0,2.1,5.0E-3,0.105/
&MESH ID='MESH-01-02-01-02', IJK=18,20,20, XB=0.09,0.18,2.0,2.1,5.0E-3,0.105/
&MESH ID='MESH-02-01-01-01', IJK=18,20,20, XB=0.0,0.09,2.1,2.2,5.0E-3,0.105/
&MESH ID='MESH-02-01-01-02', IJK=18,20,20, XB=0.09,0.18,2.1,2.2,5.0E-3,0.105/
&MESH ID='MESH-02-02', IJK=36,20,24, XB=0.0,0.18,2.2,2.3,5.0E-3,0.125/
&MESH ID='MESH-03', IJK=32,40,24, XB=0.18,0.34,1.9,2.1,5.0E-3,0.125/
&MESH ID='MESH-04', IJK=32,40,24, XB=0.18,0.34,2.1,2.3,5.0E-3,0.125/
&MESH ID='MESH-13-merged-merged', IJK=8,40,12, XB=1.0,1.08,1.9,2.3,5.0E-3,0.125/
&MESH ID='MESH-05-merged-merged-merged-01', IJK=44,40,24, XB=0.34,0.56,1.9,2.1,5.0E-3,0.125/
&MESH ID='MESH-05-merged-merged-merged-02', IJK=44,40,24, XB=0.34,0.56,2.1,2.3,5.0E-3,0.125/
&MESH ID='MESH-05-merged-merged-merged-03', IJK=44,40,24, XB=0.56,0.78,1.9,2.1,5.0E-3,0.125/
&MESH ID='MESH-05-merged-merged-merged-04', IJK=44,40,24, XB=0.56,0.78,2.1,2.3,5.0E-3,0.125/
&MESH ID='MESH-05-merged-merged-merged-05', IJK=44,40,24, XB=0.78,1.0,1.9,2.1,5.0E-3,0.125/
&MESH ID='MESH-05-merged-merged-merged-06', IJK=44,40,24, XB=0.78,1.0,2.1,2.3,5.0E-3,0.125/

&SPEC ID='WATER VAPOR'/
&SPEC ID='SPRUCE_PYROLYZATE', FORMULA='C6H10O5'/
&SPEC ID='BITUMEN_PYROLYZATE', FORMULA='C50H48O4'/
```

&SPEC ID='CARBON MONOXIDE', FORMULA='CO'/

&SPEC ID='SOOT', FORMULA='C'/

&SPEC ID='SPRUCE_PRODUCTS',

SPEC_ID(1)='CARBON DIOXIDE',

SPEC_ID(2)='CARBON MONOXIDE',

SPEC_ID(3)='NITROGEN',

SPEC_ID(4)='SOOT',

SPEC_ID(5)='WATER VAPOR',

VOLUME_FRACTION(1)=0.17482907047014,

VOLUME_FRACTION(2)=0.000699742487043609,

VOLUME_FRACTION(3)=0.659261428591368,

VOLUME_FRACTION(4)=0.00611949877078569,

VOLUME_FRACTION(5)=0.159090259680663/

&SPEC ID='BITUMEN_PRODUCTS',

SPEC_ID(1)='CARBON DIOXIDE',

SPEC_ID(2)='CARBON MONOXIDE',

SPEC_ID(3)='NITROGEN',

SPEC_ID(4)='SOOT',

SPEC_ID(5)='WATER VAPOR',

VOLUME_FRACTION(1)=1.444265E-01,

VOLUME_FRACTION(2)=2.710544E-02,

VOLUME_FRACTION(3)=7.281274E-01,

VOLUME_FRACTION(4)=6.321249E-03,

VOLUME_FRACTION(5)=9.401933E-02/

&REAC ID='BITUMEN_PYROLYZATE', HEAT_OF_COMBUSTION=3.333E+4, FUEL='BITUMEN_PYROLYZATE',
SPEC_ID_NU='BITUMEN_PRODUCTS','AIR','BITUMEN_PYROLYZATE', NU=2.817001E+02,-2.621016E+02,-
1.0/

&REAC ID='SPRUCE_PYROLYZATE', HEAT_OF_COMBUSTION=1.375E+4, FUEL='SPRUCE_PYROLYZATE',
SPEC_ID_NU='SPRUCE_PRODUCTS','AIR','SPRUCE_PYROLYZATE', NU=33.0901597290989,-
27.8760872419788,-1.0/

&DEVC ID='BWT C 150 PV', QUANTITY='BACK WALL TEMPERATURE', XYZ=0.15,2.1,0.085, IOR=-3/

&DEVC ID='BWT C 300 PV', QUANTITY='BACK WALL TEMPERATURE', XYZ=0.3,2.1,0.085, IOR=-3/

&DEVC ID='BWT C 450 PV', QUANTITY='BACK WALL TEMPERATURE', XYZ=0.45,2.1,0.085, IOR=-3/

&DEVC ID='BWT C 600 PV', QUANTITY='BACK WALL TEMPERATURE', XYZ=0.6,2.1,0.085, IOR=-3/

&DEVC ID='BWT C 750 PV', QUANTITY='BACK WALL TEMPERATURE', XYZ=0.75,2.1,0.085, IOR=-3/

&DEVC ID='BWT C 900 PV', QUANTITY='BACK WALL TEMPERATURE', XYZ=0.9,2.1,0.085, IOR=-3/

&DEVC ID='WT C 150 PV', QUANTITY='WALL TEMPERATURE', XYZ=0.15,2.1,0.085, IOR=-3/

&DEVC ID='WT C 300 PV', QUANTITY='WALL TEMPERATURE', XYZ=0.3,2.1,0.085, IOR=-3/

&DEVC ID='WT C 450 PV', QUANTITY='WALL TEMPERATURE', XYZ=0.45,2.1,0.085, IOR=-3/

&DEVC ID='WT C 600 PV', QUANTITY='WALL TEMPERATURE', XYZ=0.6,2.1,0.085, IOR=-3/

&DEVC ID='WT C 750 PV', QUANTITY='WALL TEMPERATURE', XYZ=0.75,2.1,0.085, IOR=-3/

&DEVC ID='WT C 900 PV', QUANTITY='WALL TEMPERATURE', XYZ=0.9,2.1,0.085, IOR=-3/

&DEVC ID='THCP C 150 PV', QUANTITY='THERMOCOUPLE', XYZ=0.15,2.1,0.084/

&DEVC ID='THCP C 300 PV', QUANTITY='THERMOCOUPLE', XYZ=0.3,2.1,0.084/

&DEVC ID='THCP C 450 PV', QUANTITY='THERMOCOUPLE', XYZ=0.45,2.1,0.084/

&DEVC ID='THCP C 600 PV', QUANTITY='THERMOCOUPLE', XYZ=0.6,2.1,0.084/

&DEVC ID='THCP C 750 PV', QUANTITY='THERMOCOUPLE', XYZ=0.75,2.1,0.084/

&DEVC ID='THCP C 900 PV', QUANTITY='THERMOCOUPLE', XYZ=0.9,2.1,0.084/

&DEVC ID='T Z+ C 150 R WALL', QUANTITY='WALL TEMPERATURE', XYZ=0.15,2.1,0.025, IOR=3/

&DEVC ID='T Z+ C 150 R d=0.001', DEPTH=1.0E-3, QUANTITY='INSIDE WALL TEMPERATURE',
XYZ=0.15,2.1,0.025, IOR=3/

&DEVC ID='T Z+ C 150 R d=0.002', DEPTH=2.0E-3, QUANTITY='INSIDE WALL TEMPERATURE',
XYZ=0.15,2.1,0.025, IOR=3/

&DEVC ID='T Z+ C 150 R d=0.003', DEPTH=3.0E-3, QUANTITY='INSIDE WALL TEMPERATURE',
XYZ=0.15,2.1,0.025, IOR=3/

&DEVC ID='T Z+ C 150 R d=0.004', DEPTH=4.0E-3, QUANTITY='INSIDE WALL TEMPERATURE',
XYZ=0.15,2.1,0.025, IOR=3/

&DEVC ID='T Z+ C 150 R d=0.005', DEPTH=5.0E-3, QUANTITY='INSIDE WALL TEMPERATURE',
XYZ=0.15,2.1,0.025, IOR=3/

&DEVC ID='T Z+ C 150 R d=0.006', DEPTH=6.0E-3, QUANTITY='INSIDE WALL TEMPERATURE',
XYZ=0.15,2.1,0.025, IOR=3/

&DEVC ID='T Z+ C 150 R d=0.007', DEPTH=7.0E-3, QUANTITY='INSIDE WALL TEMPERATURE',
XYZ=0.15,2.1,0.025, IOR=3/

&DEVC ID='T Z+ C 150 R d=0.008', DEPTH=8.0E-3, QUANTITY='INSIDE WALL TEMPERATURE',
XYZ=0.15,2.1,0.025, IOR=3/

&DEVC ID='T Z+ C 150 R d=0.009', DEPTH=9.0E-3, QUANTITY='INSIDE WALL TEMPERATURE',
XYZ=0.15,2.1,0.025, IOR=3/

&DEVC ID='T Z+ C 150 R d=0.010', DEPTH=0.01, QUANTITY='INSIDE WALL TEMPERATURE',
XYZ=0.15,2.1,0.025, IOR=3/

&DEVC ID='T Z+ C 150 R d=0.011', DEPTH=0.011, QUANTITY='INSIDE WALL TEMPERATURE',
XYZ=0.15,2.1,0.025, IOR=3/

&DEVC ID='T Z+ C 150 R d=0.012', DEPTH=0.012, QUANTITY='INSIDE WALL TEMPERATURE',
XYZ=0.15,2.1,0.025, IOR=3/

&DEVC ID='T Z+ C 150 R d=0.013', DEPTH=0.013, QUANTITY='INSIDE WALL TEMPERATURE',
XYZ=0.15,2.1,0.025, IOR=3/

&DEVC ID='T Z+ C 150 R d=0.014', DEPTH=0.014, QUANTITY='INSIDE WALL TEMPERATURE',
XYZ=0.15,2.1,0.025, IOR=3/

&DEVC ID='T Z+ C 150 R d=0.015', DEPTH=0.015, QUANTITY='INSIDE WALL TEMPERATURE',
XYZ=0.15,2.1,0.025, IOR=3/

&DEVC ID='T Z+ C 150 R d=0.016', DEPTH=0.016, QUANTITY='INSIDE WALL TEMPERATURE',
XYZ=0.15,2.1,0.025, IOR=3/

&DEVC ID='T Z+ C 150 R d=0.017', DEPTH=0.017, QUANTITY='INSIDE WALL TEMPERATURE',
XYZ=0.15,2.1,0.025, IOR=3/

&DEVC ID='T Z+ C 150 R d=0.018', DEPTH=0.018, QUANTITY='INSIDE WALL TEMPERATURE',
XYZ=0.15,2.1,0.025, IOR=3/

&DEVC ID='T Z+ C 150 R d=0.019', DEPTH=0.019, QUANTITY='INSIDE WALL TEMPERATURE',
XYZ=0.15,2.1,0.025, IOR=3/

&DEVC ID='T Z+ C 150 R d=0.020', DEPTH=0.02, QUANTITY='INSIDE WALL TEMPERATURE',
XYZ=0.15,2.1,0.025, IOR=3/

&DEVC ID='T Z+ C 150 R d=0.021', DEPTH=0.021, QUANTITY='INSIDE WALL TEMPERATURE',
XYZ=0.15,2.1,0.025, IOR=3/
&DEVC ID='T Z+ C 150 R d=0.022', DEPTH=0.022, QUANTITY='INSIDE WALL TEMPERATURE',
XYZ=0.15,2.1,0.025, IOR=3/
&DEVC ID='T Z+ C 150 R d=0.023', DEPTH=0.023, QUANTITY='INSIDE WALL TEMPERATURE',
XYZ=0.15,2.1,0.025, IOR=3/
&DEVC ID='T Z+ C 150 R d=0.024', DEPTH=0.024, QUANTITY='INSIDE WALL TEMPERATURE',
XYZ=0.15,2.1,0.025, IOR=3/
&DEVC ID='T Z+ C 150 R d=0.025', DEPTH=0.025, QUANTITY='INSIDE WALL TEMPERATURE',
XYZ=0.15,2.1,0.025, IOR=3/
&DEVC ID='T Z+ C 150 R BACK', QUANTITY='BACK WALL TEMPERATURE', XYZ=0.15,2.1,0.025, IOR=3/
&DEVC ID='QRAD Z+ C 150 R', QUANTITY='RADIATIVE HEAT FLUX', XYZ=0.15,2.1,0.025, IOR=3/
&DEVC ID='QCONV Z+ C 150 R', QUANTITY='CONVECTIVE HEAT FLUX', XYZ=0.15,2.1,0.025, IOR=3/
&DEVC ID='INCIDENT HEAT FLUX Z+ C 150 R', QUANTITY='INCIDENT HEAT FLUX', XYZ=0.15,2.1,0.025,
IOR=3/
&DEVC ID='HEAT FLUX Z+ C 150 R', QUANTITY='NET HEAT FLUX', XYZ=0.15,2.1,0.025, IOR=3/
&DEVC ID='HEAT TRANS COEFFICIENT Z+ C 150 R', QUANTITY='HEAT TRANSFER COEFFICIENT',
XYZ=0.15,2.1,0.025, IOR=3/
&DEVC ID='TGAS Z+ C 150 R', QUANTITY='TEMPERATURE', XYZ=0.15,2.1,0.026,
ORIENTATION=0.0,0.0,1.0/
&DEVC ID='T Z+ C 300 R WALL', QUANTITY='WALL TEMPERATURE', XYZ=0.3,2.1,0.025, IOR=3/
&DEVC ID='T Z+ C 300 R d=0.001', DEPTH=1.0E-3, QUANTITY='INSIDE WALL TEMPERATURE',
XYZ=0.3,2.1,0.025, IOR=3/
&DEVC ID='T Z+ C 300 R d=0.002', DEPTH=2.0E-3, QUANTITY='INSIDE WALL TEMPERATURE',
XYZ=0.3,2.1,0.025, IOR=3/
&DEVC ID='T Z+ C 300 R d=0.003', DEPTH=3.0E-3, QUANTITY='INSIDE WALL TEMPERATURE',
XYZ=0.3,2.1,0.025, IOR=3/
&DEVC ID='T Z+ C 300 R d=0.004', DEPTH=4.0E-3, QUANTITY='INSIDE WALL TEMPERATURE',
XYZ=0.3,2.1,0.025, IOR=3/
&DEVC ID='T Z+ C 300 R d=0.005', DEPTH=5.0E-3, QUANTITY='INSIDE WALL TEMPERATURE',
XYZ=0.3,2.1,0.025, IOR=3/
&DEVC ID='T Z+ C 300 R d=0.006', DEPTH=6.0E-3, QUANTITY='INSIDE WALL TEMPERATURE',
XYZ=0.3,2.1,0.025, IOR=3/

&DEVC ID='T Z+ C 300 R d=0.007', DEPTH=7.0E-3, QUANTITY='INSIDE WALL TEMPERATURE',
XYZ=0.3,2.1,0.025, IOR=3/

&DEVC ID='T Z+ C 300 R d=0.008', DEPTH=8.0E-3, QUANTITY='INSIDE WALL TEMPERATURE',
XYZ=0.3,2.1,0.025, IOR=3/

&DEVC ID='T Z+ C 300 R d=0.009', DEPTH=9.0E-3, QUANTITY='INSIDE WALL TEMPERATURE',
XYZ=0.3,2.1,0.025, IOR=3/

&DEVC ID='T Z+ C 300 R d=0.010', DEPTH=0.01, QUANTITY='INSIDE WALL TEMPERATURE',
XYZ=0.3,2.1,0.025, IOR=3/

&DEVC ID='T Z+ C 300 R d=0.011', DEPTH=0.011, QUANTITY='INSIDE WALL TEMPERATURE',
XYZ=0.3,2.1,0.025, IOR=3/

&DEVC ID='T Z+ C 300 R d=0.012', DEPTH=0.012, QUANTITY='INSIDE WALL TEMPERATURE',
XYZ=0.3,2.1,0.025, IOR=3/

&DEVC ID='T Z+ C 300 R d=0.013', DEPTH=0.013, QUANTITY='INSIDE WALL TEMPERATURE',
XYZ=0.3,2.1,0.025, IOR=3/

&DEVC ID='T Z+ C 300 R d=0.014', DEPTH=0.014, QUANTITY='INSIDE WALL TEMPERATURE',
XYZ=0.3,2.1,0.025, IOR=3/

&DEVC ID='T Z+ C 300 R d=0.015', DEPTH=0.015, QUANTITY='INSIDE WALL TEMPERATURE',
XYZ=0.3,2.1,0.025, IOR=3/

&DEVC ID='T Z+ C 300 R d=0.016', DEPTH=0.016, QUANTITY='INSIDE WALL TEMPERATURE',
XYZ=0.3,2.1,0.025, IOR=3/

&DEVC ID='T Z+ C 300 R d=0.017', DEPTH=0.017, QUANTITY='INSIDE WALL TEMPERATURE',
XYZ=0.3,2.1,0.025, IOR=3/

&DEVC ID='T Z+ C 300 R d=0.018', DEPTH=0.018, QUANTITY='INSIDE WALL TEMPERATURE',
XYZ=0.3,2.1,0.025, IOR=3/

&DEVC ID='T Z+ C 300 R d=0.019', DEPTH=0.019, QUANTITY='INSIDE WALL TEMPERATURE',
XYZ=0.3,2.1,0.025, IOR=3/

&DEVC ID='T Z+ C 300 R d=0.020', DEPTH=0.02, QUANTITY='INSIDE WALL TEMPERATURE',
XYZ=0.3,2.1,0.025, IOR=3/

&DEVC ID='T Z+ C 300 R d=0.021', DEPTH=0.021, QUANTITY='INSIDE WALL TEMPERATURE',
XYZ=0.3,2.1,0.025, IOR=3/

&DEVC ID='T Z+ C 300 R d=0.022', DEPTH=0.022, QUANTITY='INSIDE WALL TEMPERATURE',
XYZ=0.3,2.1,0.025, IOR=3/

&DEVC ID='T Z+ C 300 R d=0.023', DEPTH=0.023, QUANTITY='INSIDE WALL TEMPERATURE',
XYZ=0.3,2.1,0.025, IOR=3/

&DEVC ID='T Z+ C 300 R d=0.024', DEPTH=0.024, QUANTITY='INSIDE WALL TEMPERATURE', XYZ=0.3,2.1,0.025, IOR=3/
&DEVC ID='T Z+ C 300 R d=0.025', DEPTH=0.025, QUANTITY='INSIDE WALL TEMPERATURE', XYZ=0.3,2.1,0.025, IOR=3/
&DEVC ID='T Z+ C 300 R BACK', QUANTITY='BACK WALL TEMPERATURE', XYZ=0.3,2.1,0.025, IOR=3/
&DEVC ID='QRAD Z+ C 300 R', QUANTITY='RADIATIVE HEAT FLUX', XYZ=0.3,2.1,0.025, IOR=3/
&DEVC ID='QCONV Z+ C 300 R', QUANTITY='CONVECTIVE HEAT FLUX', XYZ=0.3,2.1,0.025, IOR=3/
&DEVC ID='INCIDENT HEAT FLUX Z+ C 300 R', QUANTITY='INCIDENT HEAT FLUX', XYZ=0.3,2.1,0.025, IOR=3/
&DEVC ID='HEAT FLUX Z+ C 300 R', QUANTITY='NET HEAT FLUX', XYZ=0.3,2.1,0.025, IOR=3/
&DEVC ID='HEAT TRANS COEFFICIENT Z+ C 300 R', QUANTITY='HEAT TRANSFER COEFFICIENT', XYZ=0.3,2.1,0.025, IOR=3/
&DEVC ID='TGAS Z+ C 300 R', QUANTITY='TEMPERATURE', XYZ=0.3,2.1,0.026, ORIENTATION=0.0,0.0,1.0/
&DEVC ID='T Z+ C 450 R WALL', QUANTITY='WALL TEMPERATURE', XYZ=0.45,2.1,0.025, IOR=3/
&DEVC ID='T Z+ C 450 R d=0.001', DEPTH=1.0E-3, QUANTITY='INSIDE WALL TEMPERATURE', XYZ=0.45,2.1,0.025, IOR=3/
&DEVC ID='T Z+ C 450 R d=0.002', DEPTH=2.0E-3, QUANTITY='INSIDE WALL TEMPERATURE', XYZ=0.45,2.1,0.025, IOR=3/
&DEVC ID='T Z+ C 450 R d=0.003', DEPTH=3.0E-3, QUANTITY='INSIDE WALL TEMPERATURE', XYZ=0.45,2.1,0.025, IOR=3/
&DEVC ID='T Z+ C 450 R d=0.004', DEPTH=4.0E-3, QUANTITY='INSIDE WALL TEMPERATURE', XYZ=0.45,2.1,0.025, IOR=3/
&DEVC ID='T Z+ C 450 R d=0.005', DEPTH=5.0E-3, QUANTITY='INSIDE WALL TEMPERATURE', XYZ=0.45,2.1,0.025, IOR=3/
&DEVC ID='T Z+ C 450 R d=0.006', DEPTH=6.0E-3, QUANTITY='INSIDE WALL TEMPERATURE', XYZ=0.45,2.1,0.025, IOR=3/
&DEVC ID='T Z+ C 450 R d=0.007', DEPTH=7.0E-3, QUANTITY='INSIDE WALL TEMPERATURE', XYZ=0.45,2.1,0.025, IOR=3/
&DEVC ID='T Z+ C 450 R d=0.008', DEPTH=8.0E-3, QUANTITY='INSIDE WALL TEMPERATURE', XYZ=0.45,2.1,0.025, IOR=3/
&DEVC ID='T Z+ C 450 R d=0.009', DEPTH=9.0E-3, QUANTITY='INSIDE WALL TEMPERATURE', XYZ=0.45,2.1,0.025, IOR=3/
&DEVC ID='T Z+ C 450 R d=0.010', DEPTH=0.01, QUANTITY='INSIDE WALL TEMPERATURE', XYZ=0.45,2.1,0.025, IOR=3/

&DEVC ID='T Z+ C 450 R d=0.011', DEPTH=0.011, QUANTITY='INSIDE WALL TEMPERATURE',
XYZ=0.45,2.1,0.025, IOR=3/

&DEVC ID='T Z+ C 450 R d=0.012', DEPTH=0.012, QUANTITY='INSIDE WALL TEMPERATURE',
XYZ=0.45,2.1,0.025, IOR=3/

&DEVC ID='T Z+ C 450 R d=0.013', DEPTH=0.013, QUANTITY='INSIDE WALL TEMPERATURE',
XYZ=0.45,2.1,0.025, IOR=3/

&DEVC ID='T Z+ C 450 R d=0.014', DEPTH=0.014, QUANTITY='INSIDE WALL TEMPERATURE',
XYZ=0.45,2.1,0.025, IOR=3/

&DEVC ID='T Z+ C 450 R d=0.015', DEPTH=0.015, QUANTITY='INSIDE WALL TEMPERATURE',
XYZ=0.45,2.1,0.025, IOR=3/

&DEVC ID='T Z+ C 450 R d=0.016', DEPTH=0.016, QUANTITY='INSIDE WALL TEMPERATURE',
XYZ=0.45,2.1,0.025, IOR=3/

&DEVC ID='T Z+ C 450 R d=0.017', DEPTH=0.017, QUANTITY='INSIDE WALL TEMPERATURE',
XYZ=0.45,2.1,0.025, IOR=3/

&DEVC ID='T Z+ C 450 R d=0.018', DEPTH=0.018, QUANTITY='INSIDE WALL TEMPERATURE',
XYZ=0.45,2.1,0.025, IOR=3/

&DEVC ID='T Z+ C 450 R d=0.019', DEPTH=0.019, QUANTITY='INSIDE WALL TEMPERATURE',
XYZ=0.45,2.1,0.025, IOR=3/

&DEVC ID='T Z+ C 450 R d=0.020', DEPTH=0.02, QUANTITY='INSIDE WALL TEMPERATURE',
XYZ=0.45,2.1,0.025, IOR=3/

&DEVC ID='T Z+ C 450 R d=0.021', DEPTH=0.021, QUANTITY='INSIDE WALL TEMPERATURE',
XYZ=0.45,2.1,0.025, IOR=3/

&DEVC ID='T Z+ C 450 R d=0.022', DEPTH=0.022, QUANTITY='INSIDE WALL TEMPERATURE',
XYZ=0.45,2.1,0.025, IOR=3/

&DEVC ID='T Z+ C 450 R d=0.023', DEPTH=0.023, QUANTITY='INSIDE WALL TEMPERATURE',
XYZ=0.45,2.1,0.025, IOR=3/

&DEVC ID='T Z+ C 450 R d=0.024', DEPTH=0.024, QUANTITY='INSIDE WALL TEMPERATURE',
XYZ=0.45,2.1,0.025, IOR=3/

&DEVC ID='T Z+ C 450 R d=0.025', DEPTH=0.025, QUANTITY='INSIDE WALL TEMPERATURE',
XYZ=0.45,2.1,0.025, IOR=3/

&DEVC ID='T Z+ C 450 R BACK', QUANTITY='BACK WALL TEMPERATURE', XYZ=0.45,2.1,0.025, IOR=3/

&DEVC ID='QRAD Z+ C 450 R', QUANTITY='RADIATIVE HEAT FLUX', XYZ=0.45,2.1,0.025, IOR=3/

&DEVC ID='QCONV Z+ C 450 R', QUANTITY='CONVECTIVE HEAT FLUX', XYZ=0.45,2.1,0.025, IOR=3/

&DEVC ID='INCIDENT HEAT FLUX Z+ C 450 R', QUANTITY='INCIDENT HEAT FLUX', XYZ=0.45,2.1,0.025,
IOR=3/

&DEVC ID='HEAT FLUX Z+ C 450 R', QUANTITY='NET HEAT FLUX', XYZ=0.45,2.1,0.025, IOR=3/

&DEVC ID='HEAT TRANS COEFFICIENT Z+ C 450 R', QUANTITY='HEAT TRANSFER COEFFICIENT', XYZ=0.45,2.1,0.025, IOR=3/

&DEVC ID='TGAS Z+ C 450 R', QUANTITY='TEMPERATURE', XYZ=0.45,2.1,0.026, ORIENTATION=0.0,0.0,1.0/

&DEVC ID='T Z+ C 600 R WALL', QUANTITY='WALL TEMPERATURE', XYZ=0.6,2.1,0.025, IOR=3/

&DEVC ID='T Z+ C 600 R d=0.001', DEPTH=1.0E-3, QUANTITY='INSIDE WALL TEMPERATURE', XYZ=0.6,2.1,0.025, IOR=3/

&DEVC ID='T Z+ C 600 R d=0.002', DEPTH=2.0E-3, QUANTITY='INSIDE WALL TEMPERATURE', XYZ=0.6,2.1,0.025, IOR=3/

&DEVC ID='T Z+ C 600 R d=0.003', DEPTH=3.0E-3, QUANTITY='INSIDE WALL TEMPERATURE', XYZ=0.6,2.1,0.025, IOR=3/

&DEVC ID='T Z+ C 600 R d=0.004', DEPTH=4.0E-3, QUANTITY='INSIDE WALL TEMPERATURE', XYZ=0.6,2.1,0.025, IOR=3/

&DEVC ID='T Z+ C 600 R d=0.005', DEPTH=5.0E-3, QUANTITY='INSIDE WALL TEMPERATURE', XYZ=0.6,2.1,0.025, IOR=3/

&DEVC ID='T Z+ C 600 R d=0.006', DEPTH=6.0E-3, QUANTITY='INSIDE WALL TEMPERATURE', XYZ=0.6,2.1,0.025, IOR=3/

&DEVC ID='T Z+ C 600 R d=0.007', DEPTH=7.0E-3, QUANTITY='INSIDE WALL TEMPERATURE', XYZ=0.6,2.1,0.025, IOR=3/

&DEVC ID='T Z+ C 600 R d=0.008', DEPTH=8.0E-3, QUANTITY='INSIDE WALL TEMPERATURE', XYZ=0.6,2.1,0.025, IOR=3/

&DEVC ID='T Z+ C 600 R d=0.009', DEPTH=9.0E-3, QUANTITY='INSIDE WALL TEMPERATURE', XYZ=0.6,2.1,0.025, IOR=3/

&DEVC ID='T Z+ C 600 R d=0.010', DEPTH=0.01, QUANTITY='INSIDE WALL TEMPERATURE', XYZ=0.6,2.1,0.025, IOR=3/

&DEVC ID='T Z+ C 600 R d=0.011', DEPTH=0.011, QUANTITY='INSIDE WALL TEMPERATURE', XYZ=0.6,2.1,0.025, IOR=3/

&DEVC ID='T Z+ C 600 R d=0.012', DEPTH=0.012, QUANTITY='INSIDE WALL TEMPERATURE', XYZ=0.6,2.1,0.025, IOR=3/

&DEVC ID='T Z+ C 600 R d=0.013', DEPTH=0.013, QUANTITY='INSIDE WALL TEMPERATURE', XYZ=0.6,2.1,0.025, IOR=3/

&DEVC ID='T Z+ C 600 R d=0.014', DEPTH=0.014, QUANTITY='INSIDE WALL TEMPERATURE', XYZ=0.6,2.1,0.025, IOR=3/

&DEVC ID='T Z+ C 600 R d=0.015', DEPTH=0.015, QUANTITY='INSIDE WALL TEMPERATURE',
XYZ=0.6,2.1,0.025, IOR=3/

&DEVC ID='T Z+ C 600 R d=0.016', DEPTH=0.016, QUANTITY='INSIDE WALL TEMPERATURE',
XYZ=0.6,2.1,0.025, IOR=3/

&DEVC ID='T Z+ C 600 R d=0.017', DEPTH=0.017, QUANTITY='INSIDE WALL TEMPERATURE',
XYZ=0.6,2.1,0.025, IOR=3/

&DEVC ID='T Z+ C 600 R d=0.018', DEPTH=0.018, QUANTITY='INSIDE WALL TEMPERATURE',
XYZ=0.6,2.1,0.025, IOR=3/

&DEVC ID='T Z+ C 600 R d=0.019', DEPTH=0.019, QUANTITY='INSIDE WALL TEMPERATURE',
XYZ=0.6,2.1,0.025, IOR=3/

&DEVC ID='T Z+ C 600 R d=0.020', DEPTH=0.02, QUANTITY='INSIDE WALL TEMPERATURE',
XYZ=0.6,2.1,0.025, IOR=3/

&DEVC ID='T Z+ C 600 R d=0.021', DEPTH=0.021, QUANTITY='INSIDE WALL TEMPERATURE',
XYZ=0.6,2.1,0.025, IOR=3/

&DEVC ID='T Z+ C 600 R d=0.022', DEPTH=0.022, QUANTITY='INSIDE WALL TEMPERATURE',
XYZ=0.6,2.1,0.025, IOR=3/

&DEVC ID='T Z+ C 600 R d=0.023', DEPTH=0.023, QUANTITY='INSIDE WALL TEMPERATURE',
XYZ=0.6,2.1,0.025, IOR=3/

&DEVC ID='T Z+ C 600 R d=0.024', DEPTH=0.024, QUANTITY='INSIDE WALL TEMPERATURE',
XYZ=0.6,2.1,0.025, IOR=3/

&DEVC ID='T Z+ C 600 R d=0.025', DEPTH=0.025, QUANTITY='INSIDE WALL TEMPERATURE',
XYZ=0.6,2.1,0.025, IOR=3/

&DEVC ID='T Z+ C 600 R BACK', QUANTITY='BACK WALL TEMPERATURE', XYZ=0.6,2.1,0.025, IOR=3/

&DEVC ID='QRAD Z+ C 600 R', QUANTITY='RADIATIVE HEAT FLUX', XYZ=0.6,2.1,0.025, IOR=3/

&DEVC ID='QCONV Z+ C 600 R', QUANTITY='CONVECTIVE HEAT FLUX', XYZ=0.6,2.1,0.025, IOR=3/

&DEVC ID='INCIDENT HEAT FLUX Z+ C 600 R', QUANTITY='INCIDENT HEAT FLUX', XYZ=0.6,2.1,0.025,
IOR=3/

&DEVC ID='HEAT FLUX Z+ C 600 R', QUANTITY='NET HEAT FLUX', XYZ=0.6,2.1,0.025, IOR=3/

&DEVC ID='HEAT TRANS COEFFICIENT Z+ C 600 R', QUANTITY='HEAT TRANSFER COEFFICIENT',
XYZ=0.6,2.1,0.025, IOR=3/

&DEVC ID='TGAS Z+ C 600 R', QUANTITY='TEMPERATURE', XYZ=0.6,2.1,0.026, ORIENTATION=0.0,0.0,1.0/

&DEVC ID='T Z+ C 750 R WALL', QUANTITY='WALL TEMPERATURE', XYZ=0.75,2.1,0.025, IOR=3/

&DEVC ID='T Z+ C 750 R d=0.001', DEPTH=1.0E-3, QUANTITY='INSIDE WALL TEMPERATURE',
XYZ=0.75,2.1,0.025, IOR=3/

&DEVC ID='T Z+ C 750 R d=0.002', DEPTH=2.0E-3, QUANTITY='INSIDE WALL TEMPERATURE',
XYZ=0.75,2.1,0.025, IOR=3/

&DEVC ID='T Z+ C 750 R d=0.003', DEPTH=3.0E-3, QUANTITY='INSIDE WALL TEMPERATURE',
XYZ=0.75,2.1,0.025, IOR=3/

&DEVC ID='T Z+ C 750 R d=0.004', DEPTH=4.0E-3, QUANTITY='INSIDE WALL TEMPERATURE',
XYZ=0.75,2.1,0.025, IOR=3/

&DEVC ID='T Z+ C 750 R d=0.005', DEPTH=5.0E-3, QUANTITY='INSIDE WALL TEMPERATURE',
XYZ=0.75,2.1,0.025, IOR=3/

&DEVC ID='T Z+ C 750 R d=0.006', DEPTH=6.0E-3, QUANTITY='INSIDE WALL TEMPERATURE',
XYZ=0.75,2.1,0.025, IOR=3/

&DEVC ID='T Z+ C 750 R d=0.007', DEPTH=7.0E-3, QUANTITY='INSIDE WALL TEMPERATURE',
XYZ=0.75,2.1,0.025, IOR=3/

&DEVC ID='T Z+ C 750 R d=0.008', DEPTH=8.0E-3, QUANTITY='INSIDE WALL TEMPERATURE',
XYZ=0.75,2.1,0.025, IOR=3/

&DEVC ID='T Z+ C 750 R d=0.009', DEPTH=9.0E-3, QUANTITY='INSIDE WALL TEMPERATURE',
XYZ=0.75,2.1,0.025, IOR=3/

&DEVC ID='T Z+ C 750 R d=0.010', DEPTH=0.01, QUANTITY='INSIDE WALL TEMPERATURE',
XYZ=0.75,2.1,0.025, IOR=3/

&DEVC ID='T Z+ C 750 R d=0.011', DEPTH=0.011, QUANTITY='INSIDE WALL TEMPERATURE',
XYZ=0.75,2.1,0.025, IOR=3/

&DEVC ID='T Z+ C 750 R d=0.012', DEPTH=0.012, QUANTITY='INSIDE WALL TEMPERATURE',
XYZ=0.75,2.1,0.025, IOR=3/

&DEVC ID='T Z+ C 750 R d=0.013', DEPTH=0.013, QUANTITY='INSIDE WALL TEMPERATURE',
XYZ=0.75,2.1,0.025, IOR=3/

&DEVC ID='T Z+ C 750 R d=0.014', DEPTH=0.014, QUANTITY='INSIDE WALL TEMPERATURE',
XYZ=0.75,2.1,0.025, IOR=3/

&DEVC ID='T Z+ C 750 R d=0.015', DEPTH=0.015, QUANTITY='INSIDE WALL TEMPERATURE',
XYZ=0.75,2.1,0.025, IOR=3/

&DEVC ID='T Z+ C 750 R d=0.016', DEPTH=0.016, QUANTITY='INSIDE WALL TEMPERATURE',
XYZ=0.75,2.1,0.025, IOR=3/

&DEVC ID='T Z+ C 750 R d=0.017', DEPTH=0.017, QUANTITY='INSIDE WALL TEMPERATURE',
XYZ=0.75,2.1,0.025, IOR=3/

&DEVC ID='T Z+ C 750 R d=0.018', DEPTH=0.018, QUANTITY='INSIDE WALL TEMPERATURE',
XYZ=0.75,2.1,0.025, IOR=3/

&DEVC ID='T Z+ C 750 R d=0.019', DEPTH=0.019, QUANTITY='INSIDE WALL TEMPERATURE',
XYZ=0.75,2.1,0.025, IOR=3/

&DEVC ID='T Z+ C 750 R d=0.020', DEPTH=0.02, QUANTITY='INSIDE WALL TEMPERATURE',
XYZ=0.75,2.1,0.025, IOR=3/

&DEVC ID='T Z+ C 750 R d=0.021', DEPTH=0.021, QUANTITY='INSIDE WALL TEMPERATURE',
XYZ=0.75,2.1,0.025, IOR=3/

&DEVC ID='T Z+ C 750 R d=0.022', DEPTH=0.022, QUANTITY='INSIDE WALL TEMPERATURE',
XYZ=0.75,2.1,0.025, IOR=3/

&DEVC ID='T Z+ C 750 R d=0.023', DEPTH=0.023, QUANTITY='INSIDE WALL TEMPERATURE',
XYZ=0.75,2.1,0.025, IOR=3/

&DEVC ID='T Z+ C 750 R d=0.024', DEPTH=0.024, QUANTITY='INSIDE WALL TEMPERATURE',
XYZ=0.75,2.1,0.025, IOR=3/

&DEVC ID='T Z+ C 750 R d=0.025', DEPTH=0.025, QUANTITY='INSIDE WALL TEMPERATURE',
XYZ=0.75,2.1,0.025, IOR=3/

&DEVC ID='T Z+ C 750 R BACK', QUANTITY='BACK WALL TEMPERATURE', XYZ=0.75,2.1,0.025, IOR=3/

&DEVC ID='QRAD Z+ C 750 R', QUANTITY='RADIATIVE HEAT FLUX', XYZ=0.75,2.1,0.025, IOR=3/

&DEVC ID='QCONV Z+ C 750 R', QUANTITY='CONVECTIVE HEAT FLUX', XYZ=0.75,2.1,0.025, IOR=3/

&DEVC ID='INCIDENT HEAT FLUX Z+ C 750 R', QUANTITY='INCIDENT HEAT FLUX', XYZ=0.75,2.1,0.025,
IOR=3/

&DEVC ID='HEAT FLUX Z+ C 750 R', QUANTITY='NET HEAT FLUX', XYZ=0.75,2.1,0.025, IOR=3/

&DEVC ID='HEAT TRANS COEFFICIENT Z+ C 750 R', QUANTITY='HEAT TRANSFER COEFFICIENT',
XYZ=0.75,2.1,0.025, IOR=3/

&DEVC ID='TGAS Z+ C 750 R', QUANTITY='TEMPERATURE', XYZ=0.75,2.1,0.026,
ORIENTATION=0.0,0.0,1.0/

&DEVC ID='T Z+ C 900 R WALL', QUANTITY='WALL TEMPERATURE', XYZ=0.9,2.1,0.025, IOR=3/

&DEVC ID='T Z+ C 900 R d=0.001', DEPTH=1.0E-3, QUANTITY='INSIDE WALL TEMPERATURE',
XYZ=0.9,2.1,0.025, IOR=3/

&DEVC ID='T Z+ C 900 R d=0.002', DEPTH=2.0E-3, QUANTITY='INSIDE WALL TEMPERATURE',
XYZ=0.9,2.1,0.025, IOR=3/

&DEVC ID='T Z+ C 900 R d=0.003', DEPTH=3.0E-3, QUANTITY='INSIDE WALL TEMPERATURE',
XYZ=0.9,2.1,0.025, IOR=3/

&DEVC ID='T Z+ C 900 R d=0.004', DEPTH=4.0E-3, QUANTITY='INSIDE WALL TEMPERATURE',
XYZ=0.9,2.1,0.025, IOR=3/

&DEVC ID='T Z+ C 900 R d=0.005', DEPTH=5.0E-3, QUANTITY='INSIDE WALL TEMPERATURE',
XYZ=0.9,2.1,0.025, IOR=3/

&DEVC ID='T Z+ C 900 R d=0.006', DEPTH=6.0E-3, QUANTITY='INSIDE WALL TEMPERATURE',
XYZ=0.9,2.1,0.025, IOR=3/

&DEVC ID='T Z+ C 900 R d=0.007', DEPTH=7.0E-3, QUANTITY='INSIDE WALL TEMPERATURE',
XYZ=0.9,2.1,0.025, IOR=3/

&DEVC ID='T Z+ C 900 R d=0.008', DEPTH=8.0E-3, QUANTITY='INSIDE WALL TEMPERATURE',
XYZ=0.9,2.1,0.025, IOR=3/

&DEVC ID='T Z+ C 900 R d=0.009', DEPTH=9.0E-3, QUANTITY='INSIDE WALL TEMPERATURE',
XYZ=0.9,2.1,0.025, IOR=3/

&DEVC ID='T Z+ C 900 R d=0.010', DEPTH=0.01, QUANTITY='INSIDE WALL TEMPERATURE',
XYZ=0.9,2.1,0.025, IOR=3/

&DEVC ID='T Z+ C 900 R d=0.011', DEPTH=0.011, QUANTITY='INSIDE WALL TEMPERATURE',
XYZ=0.9,2.1,0.025, IOR=3/

&DEVC ID='T Z+ C 900 R d=0.012', DEPTH=0.012, QUANTITY='INSIDE WALL TEMPERATURE',
XYZ=0.9,2.1,0.025, IOR=3/

&DEVC ID='T Z+ C 900 R d=0.013', DEPTH=0.013, QUANTITY='INSIDE WALL TEMPERATURE',
XYZ=0.9,2.1,0.025, IOR=3/

&DEVC ID='T Z+ C 900 R d=0.014', DEPTH=0.014, QUANTITY='INSIDE WALL TEMPERATURE',
XYZ=0.9,2.1,0.025, IOR=3/

&DEVC ID='T Z+ C 900 R d=0.015', DEPTH=0.015, QUANTITY='INSIDE WALL TEMPERATURE',
XYZ=0.9,2.1,0.025, IOR=3/

&DEVC ID='T Z+ C 900 R d=0.016', DEPTH=0.016, QUANTITY='INSIDE WALL TEMPERATURE',
XYZ=0.9,2.1,0.025, IOR=3/

&DEVC ID='T Z+ C 900 R d=0.017', DEPTH=0.017, QUANTITY='INSIDE WALL TEMPERATURE',
XYZ=0.9,2.1,0.025, IOR=3/

&DEVC ID='T Z+ C 900 R d=0.018', DEPTH=0.018, QUANTITY='INSIDE WALL TEMPERATURE',
XYZ=0.9,2.1,0.025, IOR=3/

&DEVC ID='T Z+ C 900 R d=0.019', DEPTH=0.019, QUANTITY='INSIDE WALL TEMPERATURE',
XYZ=0.9,2.1,0.025, IOR=3/

&DEVC ID='T Z+ C 900 R d=0.020', DEPTH=0.02, QUANTITY='INSIDE WALL TEMPERATURE',
XYZ=0.9,2.1,0.025, IOR=3/

&DEVC ID='T Z+ C 900 R d=0.021', DEPTH=0.021, QUANTITY='INSIDE WALL TEMPERATURE',
XYZ=0.9,2.1,0.025, IOR=3/

&DEVC ID='T Z+ C 900 R d=0.022', DEPTH=0.022, QUANTITY='INSIDE WALL TEMPERATURE',
XYZ=0.9,2.1,0.025, IOR=3/
&DEVC ID='T Z+ C 900 R d=0.023', DEPTH=0.023, QUANTITY='INSIDE WALL TEMPERATURE',
XYZ=0.9,2.1,0.025, IOR=3/
&DEVC ID='T Z+ C 900 R d=0.024', DEPTH=0.024, QUANTITY='INSIDE WALL TEMPERATURE',
XYZ=0.9,2.1,0.025, IOR=3/
&DEVC ID='T Z+ C 900 R d=0.025', DEPTH=0.025, QUANTITY='INSIDE WALL TEMPERATURE',
XYZ=0.9,2.1,0.025, IOR=3/
&DEVC ID='T Z+ C 900 R BACK', QUANTITY='BACK WALL TEMPERATURE', XYZ=0.9,2.1,0.025, IOR=3/
&DEVC ID='QRAD Z+ C 900 R', QUANTITY='RADIATIVE HEAT FLUX', XYZ=0.9,2.1,0.025, IOR=3/
&DEVC ID='QCONV Z+ C 900 R', QUANTITY='CONVECTIVE HEAT FLUX', XYZ=0.9,2.1,0.025, IOR=3/
&DEVC ID='INCIDENT HEAT FLUX Z+ C 900 R', QUANTITY='INCIDENT HEAT FLUX', XYZ=0.9,2.1,0.025,
IOR=3/
&DEVC ID='HEAT FLUX Z+ C 900 R', QUANTITY='NET HEAT FLUX', XYZ=0.9,2.1,0.025, IOR=3/
&DEVC ID='HEAT TRANS COEFFICIENT Z+ C 900 R', QUANTITY='HEAT TRANSFER COEFFICIENT',
XYZ=0.9,2.1,0.025, IOR=3/
&DEVC ID='TGAS Z+ C 900 R', QUANTITY='TEMPERATURE', XYZ=0.9,2.1,0.026, ORIENTATION=0.0,0.0,1.0/

&MATL ID='STEEL',
FYI='Drysdale, Intro to Fire Dynamics - ATF NIST Multi-Floor Validation',
SPECIFIC_HEAT=0.46,
CONDUCTIVITY=45.8,
DENSITY=7850.0,
EMISSIVITY=0.95/
&MATL ID='ICOPAL_TOPSAFE',
FYI='BMI Norge AS',
SPECIFIC_HEAT=1.47,
CONDUCTIVITY=0.2,
DENSITY=1143.0,
N_REACTIONS=1,
HEAT_OF_REACTION=83.0,

MATL_ID(1,1)='CHAR_ICOPAL_ROOFING',

NU_MATL(1,1)=0.55,

SPEC_ID(1,1)='BITUMEN_PYROLYZATE',

NU_SPEC(1,1)=0.45,

REFERENCE_TEMPERATURE=450.0,

HEATING_RATE=10.0,

PYROLYSIS_RANGE=200.0/

&MATL ID='CHAR_ICOPAL_ROOFING',

SPECIFIC_HEAT_RAMP='CHAR_ICOPAL_ROOFING_SPECIFIC_HEAT_RAMP',

CONDUCTIVITY_RAMP='CHAR_ICOPAL_ROOFING_CONDUCTIVITY_RAMP',

DENSITY=150.0,

EMISSIVITY=0.85/

&RAMP ID='CHAR_ICOPAL_ROOFING_SPECIFIC_HEAT_RAMP', T=0.0, F=1.275016/

&RAMP ID='CHAR_ICOPAL_ROOFING_SPECIFIC_HEAT_RAMP', T=50.0, F=1.361219/

&RAMP ID='CHAR_ICOPAL_ROOFING_SPECIFIC_HEAT_RAMP', T=100.0, F=1.441628/

&RAMP ID='CHAR_ICOPAL_ROOFING_SPECIFIC_HEAT_RAMP', T=150.0, F=1.515966/

&RAMP ID='CHAR_ICOPAL_ROOFING_SPECIFIC_HEAT_RAMP', T=200.0, F=1.583956/

&RAMP ID='CHAR_ICOPAL_ROOFING_SPECIFIC_HEAT_RAMP', T=250.0, F=1.64532/

&RAMP ID='CHAR_ICOPAL_ROOFING_SPECIFIC_HEAT_RAMP', T=300.0, F=1.699781/

&RAMP ID='CHAR_ICOPAL_ROOFING_SPECIFIC_HEAT_RAMP', T=350.0, F=1.74706/

&RAMP ID='CHAR_ICOPAL_ROOFING_SPECIFIC_HEAT_RAMP', T=400.0, F=1.786881/

&RAMP ID='CHAR_ICOPAL_ROOFING_SPECIFIC_HEAT_RAMP', T=450.0, F=1.818966/

&RAMP ID='CHAR_ICOPAL_ROOFING_SPECIFIC_HEAT_RAMP', T=500.0, F=1.843037/

&RAMP ID='CHAR_ICOPAL_ROOFING_SPECIFIC_HEAT_RAMP', T=550.0, F=1.858818/

&RAMP ID='CHAR_ICOPAL_ROOFING_SPECIFIC_HEAT_RAMP', T=600.0, F=1.86603/

&RAMP ID='CHAR_ICOPAL_ROOFING_SPECIFIC_HEAT_RAMP', T=650.0, F=1.864396/

&RAMP ID='CHAR_ICOPAL_ROOFING_SPECIFIC_HEAT_RAMP', T=700.0, F=1.853639/

&RAMP ID='CHAR_ICOPAL_ROOFING_SPECIFIC_HEAT_RAMP', T=750.0, F=1.83348/

&RAMP ID='CHAR_ICOPAL_ROOFING_SPECIFIC_HEAT_RAMP', T=800.0, F=1.803643/

&RAMP ID='CHAR_ICOPAL_ROOFING_SPECIFIC_HEAT_RAMP', T=850.0, F=1.763851/
&RAMP ID='CHAR_ICOPAL_ROOFING_SPECIFIC_HEAT_RAMP', T=900.0, F=1.713824/
&RAMP ID='CHAR_ICOPAL_ROOFING_SPECIFIC_HEAT_RAMP', T=950.0, F=1.653287/
&RAMP ID='CHAR_ICOPAL_ROOFING_SPECIFIC_HEAT_RAMP', T=1000.0, F=1.581961/
&RAMP ID='CHAR_ICOPAL_ROOFING_SPECIFIC_HEAT_RAMP', T=1050.0, F=1.499569/
&RAMP ID='CHAR_ICOPAL_ROOFING_SPECIFIC_HEAT_RAMP', T=1100.0, F=1.405834/
&RAMP ID='CHAR_ICOPAL_ROOFING_SPECIFIC_HEAT_RAMP', T=1150.0, F=1.300478/
&RAMP ID='CHAR_ICOPAL_ROOFING_SPECIFIC_HEAT_RAMP', T=1200.0, F=1.183223/
&RAMP ID='CHAR_ICOPAL_ROOFING_CONDUCTIVITY_RAMP', T=0.0, F=0.084726/
&RAMP ID='CHAR_ICOPAL_ROOFING_CONDUCTIVITY_RAMP', T=50.0, F=0.092126/
&RAMP ID='CHAR_ICOPAL_ROOFING_CONDUCTIVITY_RAMP', T=100.0, F=0.099526/
&RAMP ID='CHAR_ICOPAL_ROOFING_CONDUCTIVITY_RAMP', T=150.0, F=0.106926/
&RAMP ID='CHAR_ICOPAL_ROOFING_CONDUCTIVITY_RAMP', T=200.0, F=0.114326/
&RAMP ID='CHAR_ICOPAL_ROOFING_CONDUCTIVITY_RAMP', T=250.0, F=0.121726/
&RAMP ID='CHAR_ICOPAL_ROOFING_CONDUCTIVITY_RAMP', T=300.0, F=0.129126/
&RAMP ID='CHAR_ICOPAL_ROOFING_CONDUCTIVITY_RAMP', T=350.0, F=0.136526/
&RAMP ID='CHAR_ICOPAL_ROOFING_CONDUCTIVITY_RAMP', T=400.0, F=0.143926/
&RAMP ID='CHAR_ICOPAL_ROOFING_CONDUCTIVITY_RAMP', T=450.0, F=0.151326/
&RAMP ID='CHAR_ICOPAL_ROOFING_CONDUCTIVITY_RAMP', T=500.0, F=0.158726/
&RAMP ID='CHAR_ICOPAL_ROOFING_CONDUCTIVITY_RAMP', T=550.0, F=0.166126/
&RAMP ID='CHAR_ICOPAL_ROOFING_CONDUCTIVITY_RAMP', T=600.0, F=0.173526/
&RAMP ID='CHAR_ICOPAL_ROOFING_CONDUCTIVITY_RAMP', T=650.0, F=0.180926/
&RAMP ID='CHAR_ICOPAL_ROOFING_CONDUCTIVITY_RAMP', T=700.0, F=0.188326/
&RAMP ID='CHAR_ICOPAL_ROOFING_CONDUCTIVITY_RAMP', T=750.0, F=0.195726/
&RAMP ID='CHAR_ICOPAL_ROOFING_CONDUCTIVITY_RAMP', T=800.0, F=0.203126/
&RAMP ID='CHAR_ICOPAL_ROOFING_CONDUCTIVITY_RAMP', T=850.0, F=0.210526/
&RAMP ID='CHAR_ICOPAL_ROOFING_CONDUCTIVITY_RAMP', T=900.0, F=0.217926/
&RAMP ID='CHAR_ICOPAL_ROOFING_CONDUCTIVITY_RAMP', T=950.0, F=0.225326/
&RAMP ID='CHAR_ICOPAL_ROOFING_CONDUCTIVITY_RAMP', T=1000.0, F=0.232726/

&RAMP ID='CHAR_ICOPAL_ROOFING_CONDUCTIVITY_RAMP', T=1050.0, F=0.240126/
&RAMP ID='CHAR_ICOPAL_ROOFING_CONDUCTIVITY_RAMP', T=1100.0, F=0.247526/
&RAMP ID='CHAR_ICOPAL_ROOFING_CONDUCTIVITY_RAMP', T=1150.0, F=0.254926/
&RAMP ID='CHAR_ICOPAL_ROOFING_CONDUCTIVITY_RAMP', T=1200.0, F=0.262326/
&MATL ID='SPRUCE',
FYI='Rinta-Paavola & Hostikka 2020 - A model for the pyrolysis of two Nordic structural timbers',
SPECIFIC_HEAT_RAMP='SPRUCE_SPECIFIC_HEAT_RAMP',
CONDUCTIVITY=0.09,
DENSITY=408.0,
N_REACTIONS=1,
HEAT_OF_REACTION=19.0,
MATL_ID(1,1)='CHAR_SPRUCE',
NU_MATL(1,1)=0.16,
SPEC_ID(1,1)='SPRUCE_PYROLYZATE',
NU_SPEC(1,1)=0.84,
N_S=1.89,
A=2.19311E+11,
E=1.905E+5/
&RAMP ID='SPRUCE_SPECIFIC_HEAT_RAMP', T=30.0, F=0.92/
&RAMP ID='SPRUCE_SPECIFIC_HEAT_RAMP', T=50.0, F=1.008/
&RAMP ID='SPRUCE_SPECIFIC_HEAT_RAMP', T=70.0, F=1.096/
&RAMP ID='SPRUCE_SPECIFIC_HEAT_RAMP', T=90.0, F=1.184/
&RAMP ID='SPRUCE_SPECIFIC_HEAT_RAMP', T=110.0, F=1.272/
&RAMP ID='SPRUCE_SPECIFIC_HEAT_RAMP', T=130.0, F=1.36/
&RAMP ID='SPRUCE_SPECIFIC_HEAT_RAMP', T=150.0, F=1.448/
&RAMP ID='SPRUCE_SPECIFIC_HEAT_RAMP', T=170.0, F=1.536/
&RAMP ID='SPRUCE_SPECIFIC_HEAT_RAMP', T=190.0, F=1.624/
&RAMP ID='SPRUCE_SPECIFIC_HEAT_RAMP', T=210.0, F=1.712/
&RAMP ID='SPRUCE_SPECIFIC_HEAT_RAMP', T=230.0, F=1.8/

&RAMP ID='SPRUCE_SPECIFIC_HEAT_RAMP', T=250.0, F=1.888/
&RAMP ID='SPRUCE_SPECIFIC_HEAT_RAMP', T=270.0, F=1.976/
&RAMP ID='SPRUCE_SPECIFIC_HEAT_RAMP', T=290.0, F=2.064/
&RAMP ID='SPRUCE_SPECIFIC_HEAT_RAMP', T=310.0, F=2.152/
&RAMP ID='SPRUCE_SPECIFIC_HEAT_RAMP', T=330.0, F=2.24/
&RAMP ID='SPRUCE_SPECIFIC_HEAT_RAMP', T=350.0, F=2.328/
&RAMP ID='SPRUCE_SPECIFIC_HEAT_RAMP', T=370.0, F=2.416/
&RAMP ID='SPRUCE_SPECIFIC_HEAT_RAMP', T=390.0, F=2.504/
&RAMP ID='SPRUCE_SPECIFIC_HEAT_RAMP', T=410.0, F=2.592/
&RAMP ID='SPRUCE_SPECIFIC_HEAT_RAMP', T=430.0, F=2.68/
&RAMP ID='SPRUCE_SPECIFIC_HEAT_RAMP', T=450.0, F=2.768/
&RAMP ID='SPRUCE_SPECIFIC_HEAT_RAMP', T=470.0, F=2.856/
&RAMP ID='SPRUCE_SPECIFIC_HEAT_RAMP', T=490.0, F=2.944/
&RAMP ID='SPRUCE_SPECIFIC_HEAT_RAMP', T=510.0, F=3.032/
&RAMP ID='SPRUCE_SPECIFIC_HEAT_RAMP', T=530.0, F=3.12/
&RAMP ID='SPRUCE_SPECIFIC_HEAT_RAMP', T=550.0, F=3.208/
&RAMP ID='SPRUCE_SPECIFIC_HEAT_RAMP', T=570.0, F=3.296/
&RAMP ID='SPRUCE_SPECIFIC_HEAT_RAMP', T=590.0, F=3.384/
&RAMP ID='SPRUCE_SPECIFIC_HEAT_RAMP', T=610.0, F=3.472/
&RAMP ID='SPRUCE_SPECIFIC_HEAT_RAMP', T=630.0, F=3.56/
&RAMP ID='SPRUCE_SPECIFIC_HEAT_RAMP', T=650.0, F=3.648/
&RAMP ID='SPRUCE_SPECIFIC_HEAT_RAMP', T=670.0, F=3.736/
&RAMP ID='SPRUCE_SPECIFIC_HEAT_RAMP', T=690.0, F=3.824/
&RAMP ID='SPRUCE_SPECIFIC_HEAT_RAMP', T=710.0, F=3.912/
&RAMP ID='SPRUCE_SPECIFIC_HEAT_RAMP', T=730.0, F=4.0/
&RAMP ID='SPRUCE_SPECIFIC_HEAT_RAMP', T=750.0, F=4.088/
&RAMP ID='SPRUCE_SPECIFIC_HEAT_RAMP', T=770.0, F=4.176/
&RAMP ID='SPRUCE_SPECIFIC_HEAT_RAMP', T=790.0, F=4.264/
&RAMP ID='SPRUCE_SPECIFIC_HEAT_RAMP', T=810.0, F=4.352/

&MATL ID='CHAR_SPRUCE',

FYI='Rinta-Paavola & Hostikka 2020 - A model for the pyrolysis of two Nordic structural timbers',

SPECIFIC_HEAT_RAMP='CHAR_SPRUCE_SPECIFIC_HEAT_RAMP',

CONDUCTIVITY=0.22,

DENSITY=0.59,

EMISSIVITY=0.85/

&RAMP ID='CHAR_SPRUCE_SPECIFIC_HEAT_RAMP', T=0.0, F=0.545879/

&RAMP ID='CHAR_SPRUCE_SPECIFIC_HEAT_RAMP', T=50.0, F=0.843743/

&RAMP ID='CHAR_SPRUCE_SPECIFIC_HEAT_RAMP', T=100.0, F=1.036761/

&RAMP ID='CHAR_SPRUCE_SPECIFIC_HEAT_RAMP', T=150.0, F=1.171407/

&RAMP ID='CHAR_SPRUCE_SPECIFIC_HEAT_RAMP', T=200.0, F=1.270994/

&RAMP ID='CHAR_SPRUCE_SPECIFIC_HEAT_RAMP', T=250.0, F=1.348258/

&RAMP ID='CHAR_SPRUCE_SPECIFIC_HEAT_RAMP', T=300.0, F=1.410638/

&RAMP ID='CHAR_SPRUCE_SPECIFIC_HEAT_RAMP', T=350.0, F=1.462712/

&RAMP ID='CHAR_SPRUCE_SPECIFIC_HEAT_RAMP', T=400.0, F=1.507426/

&RAMP ID='CHAR_SPRUCE_SPECIFIC_HEAT_RAMP', T=450.0, F=1.546742/

&RAMP ID='CHAR_SPRUCE_SPECIFIC_HEAT_RAMP', T=500.0, F=1.582011/

&RAMP ID='CHAR_SPRUCE_SPECIFIC_HEAT_RAMP', T=550.0, F=1.614186/

&RAMP ID='CHAR_SPRUCE_SPECIFIC_HEAT_RAMP', T=600.0, F=1.643955/

&RAMP ID='CHAR_SPRUCE_SPECIFIC_HEAT_RAMP', T=650.0, F=1.671824/

&RAMP ID='CHAR_SPRUCE_SPECIFIC_HEAT_RAMP', T=700.0, F=1.698173/

&RAMP ID='CHAR_SPRUCE_SPECIFIC_HEAT_RAMP', T=750.0, F=1.723293/

&RAMP ID='CHAR_SPRUCE_SPECIFIC_HEAT_RAMP', T=800.0, F=1.747407/

&RAMP ID='CHAR_SPRUCE_SPECIFIC_HEAT_RAMP', T=850.0, F=1.770691/

&RAMP ID='CHAR_SPRUCE_SPECIFIC_HEAT_RAMP', T=900.0, F=1.793281/

&RAMP ID='CHAR_SPRUCE_SPECIFIC_HEAT_RAMP', T=950.0, F=1.815291/

&RAMP ID='CHAR_SPRUCE_SPECIFIC_HEAT_RAMP', T=1000.0, F=1.836808/

&RAMP ID='CHAR_SPRUCE_SPECIFIC_HEAT_RAMP', T=1050.0, F=1.857907/

&RAMP ID='CHAR_SPRUCE_SPECIFIC_HEAT_RAMP', T=1100.0, F=1.878646/

&RAMP ID='CHAR_SPRUCE_SPECIFIC_HEAT_RAMP', T=1150.0, F=1.899076/

&RAMP ID='CHAR_SPRUCE_SPECIFIC_HEAT_RAMP', T=1200.0, F=1.919238/

&MATL ID='WATER',

FYI='Rinta-Paavola & Hostikka 2020 - A model for the pyrolysis of two Nordic structural timbers',

SPECIFIC_HEAT_RAMP='WATER_SPECIFIC_HEAT_RAMP',

CONDUCTIVITY=0.6,

DENSITY=1000.0,

N_REACTIONS=1,

HEAT_OF_REACTION=2500.0,

SPEC_ID(1,1)='WATER VAPOR',

NU_SPEC(1,1)=1.0,

N_S=3.31,

A=8.725E+16,

E=1.36E+5/

&RAMP ID='WATER_SPECIFIC_HEAT_RAMP', T=20.0, F=4.7/

&RAMP ID='WATER_SPECIFIC_HEAT_RAMP', T=100.0, F=6.7/

&SURF ID='FIRE',

COLOR='RED',

TEXTURE_MAP='psm_fire.jpg',

TMP_FRONT=0.0,

MASS_FLUX=0.040755,

SPEC_ID='SPRUCE_PYROLYZATE',

RAMP_MF='FIRE_RAMP_MF'/

&RAMP ID='FIRE_RAMP_MF', T=1.0, F=0.0/

&RAMP ID='FIRE_RAMP_MF', T=2.0, F=0.076763/

&RAMP ID='FIRE_RAMP_MF', T=3.0, F=0.192907/

&RAMP ID='FIRE_RAMP_MF', T=4.0, F=0.191789/

&RAMP ID='FIRE_RAMP_MF', T=5.0, F=0.344528/

T

&RAMP ID='FIRE_RAMP_MF', T=6.0, F=0.414095/
&RAMP ID='FIRE_RAMP_MF', T=7.0, F=0.412766/
&RAMP ID='FIRE_RAMP_MF', T=8.0, F=0.503215/
&RAMP ID='FIRE_RAMP_MF', T=9.0, F=0.542661/
&RAMP ID='FIRE_RAMP_MF', T=10.0, F=0.538398/
&RAMP ID='FIRE_RAMP_MF', T=11.0, F=0.589181/
&RAMP ID='FIRE_RAMP_MF', T=12.0, F=0.595172/
&RAMP ID='FIRE_RAMP_MF', T=13.0, F=0.587565/
&RAMP ID='FIRE_RAMP_MF', T=14.0, F=0.605009/
&RAMP ID='FIRE_RAMP_MF', T=15.0, F=0.600666/
&RAMP ID='FIRE_RAMP_MF', T=16.0, F=0.609562/
&RAMP ID='FIRE_RAMP_MF', T=17.0, F=0.612804/
&RAMP ID='FIRE_RAMP_MF', T=18.0, F=0.608259/
&RAMP ID='FIRE_RAMP_MF', T=19.0, F=0.6178/
&RAMP ID='FIRE_RAMP_MF', T=20.0, F=0.629197/
&RAMP ID='FIRE_RAMP_MF', T=21.0, F=0.616527/
&RAMP ID='FIRE_RAMP_MF', T=22.0, F=0.615725/
&RAMP ID='FIRE_RAMP_MF', T=23.0, F=0.612425/
&RAMP ID='FIRE_RAMP_MF', T=24.0, F=0.626394/
&RAMP ID='FIRE_RAMP_MF', T=25.0, F=0.623314/
&RAMP ID='FIRE_RAMP_MF', T=26.0, F=0.616728/
&RAMP ID='FIRE_RAMP_MF', T=27.0, F=0.622871/
&RAMP ID='FIRE_RAMP_MF', T=28.0, F=0.635061/
&RAMP ID='FIRE_RAMP_MF', T=29.0, F=0.669051/
&RAMP ID='FIRE_RAMP_MF', T=30.0, F=0.667184/
&RAMP ID='FIRE_RAMP_MF', T=31.0, F=0.670037/
&RAMP ID='FIRE_RAMP_MF', T=32.0, F=0.697826/
&RAMP ID='FIRE_RAMP_MF', T=33.0, F=0.699424/
&RAMP ID='FIRE_RAMP_MF', T=34.0, F=0.699382/

&RAMP ID='FIRE_RAMP_MF', T=35.0, F=0.722983/
&RAMP ID='FIRE_RAMP_MF', T=36.0, F=0.730807/
&RAMP ID='FIRE_RAMP_MF', T=37.0, F=0.739588/
&RAMP ID='FIRE_RAMP_MF', T=38.0, F=0.744807/
&RAMP ID='FIRE_RAMP_MF', T=39.0, F=0.744992/
&RAMP ID='FIRE_RAMP_MF', T=40.0, F=0.73842/
&RAMP ID='FIRE_RAMP_MF', T=41.0, F=0.754416/
&RAMP ID='FIRE_RAMP_MF', T=42.0, F=0.763355/
&RAMP ID='FIRE_RAMP_MF', T=43.0, F=0.766666/
&RAMP ID='FIRE_RAMP_MF', T=44.0, F=0.781464/
&RAMP ID='FIRE_RAMP_MF', T=45.0, F=0.786982/
&RAMP ID='FIRE_RAMP_MF', T=46.0, F=0.782583/
&RAMP ID='FIRE_RAMP_MF', T=47.0, F=0.779262/
&RAMP ID='FIRE_RAMP_MF', T=48.0, F=0.782604/
&RAMP ID='FIRE_RAMP_MF', T=49.0, F=0.78796/
&RAMP ID='FIRE_RAMP_MF', T=50.0, F=0.788046/
&RAMP ID='FIRE_RAMP_MF', T=51.0, F=0.807321/
&RAMP ID='FIRE_RAMP_MF', T=52.0, F=0.800329/
&RAMP ID='FIRE_RAMP_MF', T=53.0, F=0.799866/
&RAMP ID='FIRE_RAMP_MF', T=54.0, F=0.833061/
&RAMP ID='FIRE_RAMP_MF', T=55.0, F=0.828022/
&RAMP ID='FIRE_RAMP_MF', T=56.0, F=0.816089/
&RAMP ID='FIRE_RAMP_MF', T=57.0, F=0.826945/
&RAMP ID='FIRE_RAMP_MF', T=58.0, F=0.830253/
&RAMP ID='FIRE_RAMP_MF', T=59.0, F=0.822877/
&RAMP ID='FIRE_RAMP_MF', T=60.0, F=0.824395/
&RAMP ID='FIRE_RAMP_MF', T=61.0, F=0.810548/
&RAMP ID='FIRE_RAMP_MF', T=62.0, F=0.842438/
&RAMP ID='FIRE_RAMP_MF', T=63.0, F=0.855442/

&RAMP ID='FIRE_RAMP_MF', T=64.0, F=0.847681/
&RAMP ID='FIRE_RAMP_MF', T=65.0, F=0.877448/
&RAMP ID='FIRE_RAMP_MF', T=66.0, F=0.868345/
&RAMP ID='FIRE_RAMP_MF', T=67.0, F=0.864123/
&RAMP ID='FIRE_RAMP_MF', T=68.0, F=0.905976/
&RAMP ID='FIRE_RAMP_MF', T=69.0, F=0.920538/
&RAMP ID='FIRE_RAMP_MF', T=70.0, F=0.901053/
&RAMP ID='FIRE_RAMP_MF', T=71.0, F=0.923913/
&RAMP ID='FIRE_RAMP_MF', T=72.0, F=0.939493/
&RAMP ID='FIRE_RAMP_MF', T=73.0, F=0.956328/
&RAMP ID='FIRE_RAMP_MF', T=74.0, F=0.967687/
&RAMP ID='FIRE_RAMP_MF', T=75.0, F=0.970519/
&RAMP ID='FIRE_RAMP_MF', T=76.0, F=0.982906/
&RAMP ID='FIRE_RAMP_MF', T=77.0, F=0.973826/
&RAMP ID='FIRE_RAMP_MF', T=78.0, F=0.986101/
&RAMP ID='FIRE_RAMP_MF', T=79.0, F=0.992127/
&RAMP ID='FIRE_RAMP_MF', T=80.0, F=0.97485/
&RAMP ID='FIRE_RAMP_MF', T=81.0, F=0.998267/
&RAMP ID='FIRE_RAMP_MF', T=82.0, F=0.987411/
&RAMP ID='FIRE_RAMP_MF', T=83.0, F=0.99867/
&RAMP ID='FIRE_RAMP_MF', T=84.0, F=1.0/
&RAMP ID='FIRE_RAMP_MF', T=85.0, F=1.0/
&RAMP ID='FIRE_RAMP_MF', T=86.0, F=0.963166/
&RAMP ID='FIRE_RAMP_MF', T=87.0, F=0.949784/
&RAMP ID='FIRE_RAMP_MF', T=88.0, F=0.949784/
&RAMP ID='FIRE_RAMP_MF', T=89.0, F=0.914733/
&RAMP ID='FIRE_RAMP_MF', T=90.0, F=0.893423/
&RAMP ID='FIRE_RAMP_MF', T=91.0, F=0.893423/
&RAMP ID='FIRE_RAMP_MF', T=92.0, F=0.856231/

&RAMP ID='FIRE_RAMP_MF', T=93.0, F=0.828296/
&RAMP ID='FIRE_RAMP_MF', T=94.0, F=0.828296/
&RAMP ID='FIRE_RAMP_MF', T=95.0, F=0.813186/
&RAMP ID='FIRE_RAMP_MF', T=96.0, F=0.784859/
&RAMP ID='FIRE_RAMP_MF', T=97.0, F=0.784859/
&RAMP ID='FIRE_RAMP_MF', T=98.0, F=0.755805/
&RAMP ID='FIRE_RAMP_MF', T=99.0, F=0.74831/
&RAMP ID='FIRE_RAMP_MF', T=100.0, F=0.74831/
&RAMP ID='FIRE_RAMP_MF', T=101.0, F=0.722385/
&RAMP ID='FIRE_RAMP_MF', T=102.0, F=0.711668/
&RAMP ID='FIRE_RAMP_MF', T=103.0, F=0.711668/
&RAMP ID='FIRE_RAMP_MF', T=104.0, F=0.676205/
&RAMP ID='FIRE_RAMP_MF', T=105.0, F=0.678151/
&RAMP ID='FIRE_RAMP_MF', T=106.0, F=0.674448/
&RAMP ID='FIRE_RAMP_MF', T=107.0, F=0.647682/
&RAMP ID='FIRE_RAMP_MF', T=108.0, F=0.633344/
&RAMP ID='FIRE_RAMP_MF', T=109.0, F=0.631847/
&RAMP ID='FIRE_RAMP_MF', T=110.0, F=0.603554/
&RAMP ID='FIRE_RAMP_MF', T=111.0, F=0.599688/
&RAMP ID='FIRE_RAMP_MF', T=112.0, F=0.604746/
&RAMP ID='FIRE_RAMP_MF', T=113.0, F=0.576521/
&RAMP ID='FIRE_RAMP_MF', T=114.0, F=0.56913/
&RAMP ID='FIRE_RAMP_MF', T=115.0, F=0.565239/
&RAMP ID='FIRE_RAMP_MF', T=116.0, F=0.550049/
&RAMP ID='FIRE_RAMP_MF', T=117.0, F=0.537788/
&RAMP ID='FIRE_RAMP_MF', T=118.0, F=0.53386/
&RAMP ID='FIRE_RAMP_MF', T=119.0, F=0.520458/
&RAMP ID='FIRE_RAMP_MF', T=120.0, F=0.513795/
&RAMP ID='FIRE_RAMP_MF', T=121.0, F=0.517626/

&RAMP ID='FIRE_RAMP_MF', T=122.0, F=0.505778/
&RAMP ID='FIRE_RAMP_MF', T=123.0, F=0.497198/
&RAMP ID='FIRE_RAMP_MF', T=124.0, F=0.498406/
&RAMP ID='FIRE_RAMP_MF', T=125.0, F=0.483366/
&RAMP ID='FIRE_RAMP_MF', T=126.0, F=0.48257/
&RAMP ID='FIRE_RAMP_MF', T=127.0, F=0.482155/
&RAMP ID='FIRE_RAMP_MF', T=128.0, F=0.483083/
&RAMP ID='FIRE_RAMP_MF', T=129.0, F=0.476341/
&RAMP ID='FIRE_RAMP_MF', T=130.0, F=0.475744/
&RAMP ID='FIRE_RAMP_MF', T=131.0, F=0.462413/
&RAMP ID='FIRE_RAMP_MF', T=132.0, F=0.453487/
&RAMP ID='FIRE_RAMP_MF', T=133.0, F=0.458962/
&RAMP ID='FIRE_RAMP_MF', T=134.0, F=0.43513/
&RAMP ID='FIRE_RAMP_MF', T=135.0, F=0.440974/
&RAMP ID='FIRE_RAMP_MF', T=136.0, F=0.442941/
&RAMP ID='FIRE_RAMP_MF', T=137.0, F=0.432085/
&RAMP ID='FIRE_RAMP_MF', T=138.0, F=0.420421/
&RAMP ID='FIRE_RAMP_MF', T=139.0, F=0.420476/
&RAMP ID='FIRE_RAMP_MF', T=140.0, F=0.405721/
&RAMP ID='FIRE_RAMP_MF', T=141.0, F=0.399597/
&RAMP ID='FIRE_RAMP_MF', T=142.0, F=0.397668/
&RAMP ID='FIRE_RAMP_MF', T=143.0, F=0.38185/
&RAMP ID='FIRE_RAMP_MF', T=144.0, F=0.370062/
&RAMP ID='FIRE_RAMP_MF', T=145.0, F=0.371065/
&RAMP ID='FIRE_RAMP_MF', T=146.0, F=0.35523/
&RAMP ID='FIRE_RAMP_MF', T=147.0, F=0.338103/
&RAMP ID='FIRE_RAMP_MF', T=148.0, F=0.344356/
&RAMP ID='FIRE_RAMP_MF', T=149.0, F=0.328913/
&RAMP ID='FIRE_RAMP_MF', T=150.0, F=0.322864/

&RAMP ID='FIRE_RAMP_MF', T=151.0, F=0.321257/
&RAMP ID='FIRE_RAMP_MF', T=152.0, F=0.312501/
&RAMP ID='FIRE_RAMP_MF', T=153.0, F=0.309897/
&RAMP ID='FIRE_RAMP_MF', T=154.0, F=0.305333/
&RAMP ID='FIRE_RAMP_MF', T=155.0, F=0.304348/
&RAMP ID='FIRE_RAMP_MF', T=156.0, F=0.297747/
&RAMP ID='FIRE_RAMP_MF', T=157.0, F=0.300906/
&RAMP ID='FIRE_RAMP_MF', T=158.0, F=0.290503/
&RAMP ID='FIRE_RAMP_MF', T=159.0, F=0.279984/
&RAMP ID='FIRE_RAMP_MF', T=160.0, F=0.281144/
&RAMP ID='FIRE_RAMP_MF', T=161.0, F=0.26787/
&RAMP ID='FIRE_RAMP_MF', T=162.0, F=0.25867/
&RAMP ID='FIRE_RAMP_MF', T=163.0, F=0.257966/
&RAMP ID='FIRE_RAMP_MF', T=164.0, F=0.239399/
&RAMP ID='FIRE_RAMP_MF', T=165.0, F=0.231022/
&RAMP ID='FIRE_RAMP_MF', T=166.0, F=0.228784/
&RAMP ID='FIRE_RAMP_MF', T=167.0, F=0.211589/
&RAMP ID='FIRE_RAMP_MF', T=168.0, F=0.2043/
&RAMP ID='FIRE_RAMP_MF', T=169.0, F=0.205274/
&RAMP ID='FIRE_RAMP_MF', T=170.0, F=0.195742/
&RAMP ID='FIRE_RAMP_MF', T=171.0, F=0.195952/
&RAMP ID='FIRE_RAMP_MF', T=172.0, F=0.189876/
&RAMP ID='FIRE_RAMP_MF', T=173.0, F=0.189717/
&RAMP ID='FIRE_RAMP_MF', T=174.0, F=0.19064/
&RAMP ID='FIRE_RAMP_MF', T=175.0, F=0.192859/
&RAMP ID='FIRE_RAMP_MF', T=176.0, F=0.184471/
&RAMP ID='FIRE_RAMP_MF', T=177.0, F=0.181485/
&RAMP ID='FIRE_RAMP_MF', T=178.0, F=0.179515/
&RAMP ID='FIRE_RAMP_MF', T=179.0, F=0.177195/

&RAMP ID='FIRE_RAMP_MF', T=180.0, F=0.173479/
&RAMP ID='FIRE_RAMP_MF', T=181.0, F=0.174712/
&RAMP ID='FIRE_RAMP_MF', T=182.0, F=0.169966/
&RAMP ID='FIRE_RAMP_MF', T=183.0, F=0.167981/
&RAMP ID='FIRE_RAMP_MF', T=184.0, F=0.16603/
&RAMP ID='FIRE_RAMP_MF', T=185.0, F=0.163805/
&RAMP ID='FIRE_RAMP_MF', T=186.0, F=0.162563/
&RAMP ID='FIRE_RAMP_MF', T=187.0, F=0.162563/
&RAMP ID='FIRE_RAMP_MF', T=188.0, F=0.161748/
&RAMP ID='FIRE_RAMP_MF', T=189.0, F=0.158873/
&RAMP ID='FIRE_RAMP_MF', T=190.0, F=0.158873/
&RAMP ID='FIRE_RAMP_MF', T=191.0, F=0.158456/
&RAMP ID='FIRE_RAMP_MF', T=192.0, F=0.157259/
&RAMP ID='FIRE_RAMP_MF', T=193.0, F=0.157259/
&RAMP ID='FIRE_RAMP_MF', T=194.0, F=0.156805/
&RAMP ID='FIRE_RAMP_MF', T=195.0, F=0.15722/
&RAMP ID='FIRE_RAMP_MF', T=196.0, F=0.15722/
&RAMP ID='FIRE_RAMP_MF', T=197.0, F=0.154866/
&RAMP ID='FIRE_RAMP_MF', T=198.0, F=0.155472/
&RAMP ID='FIRE_RAMP_MF', T=199.0, F=0.155472/
&RAMP ID='FIRE_RAMP_MF', T=200.0, F=0.148909/
&RAMP ID='FIRE_RAMP_MF', T=201.0, F=0.14725/
&RAMP ID='FIRE_RAMP_MF', T=202.0, F=0.14725/
&RAMP ID='FIRE_RAMP_MF', T=203.0, F=0.149935/
&RAMP ID='FIRE_RAMP_MF', T=204.0, F=0.151804/
&RAMP ID='FIRE_RAMP_MF', T=205.0, F=0.151804/
&RAMP ID='FIRE_RAMP_MF', T=206.0, F=0.148811/
&RAMP ID='FIRE_RAMP_MF', T=207.0, F=0.146026/
&RAMP ID='FIRE_RAMP_MF', T=208.0, F=0.147673/

&RAMP ID='FIRE_RAMP_MF', T=209.0, F=0.138999/
&RAMP ID='FIRE_RAMP_MF', T=210.0, F=0.14072/
&RAMP ID='FIRE_RAMP_MF', T=211.0, F=0.141885/
&RAMP ID='FIRE_RAMP_MF', T=212.0, F=0.143247/
&RAMP ID='FIRE_RAMP_MF', T=213.0, F=0.140454/
&RAMP ID='FIRE_RAMP_MF', T=214.0, F=0.1396/
&RAMP ID='FIRE_RAMP_MF', T=215.0, F=0.141249/
&RAMP ID='FIRE_RAMP_MF', T=216.0, F=0.140399/
&RAMP ID='FIRE_RAMP_MF', T=217.0, F=0.141028/
&RAMP ID='FIRE_RAMP_MF', T=218.0, F=0.140318/
&RAMP ID='FIRE_RAMP_MF', T=219.0, F=0.141528/
&RAMP ID='FIRE_RAMP_MF', T=220.0, F=0.14178/
&RAMP ID='FIRE_RAMP_MF', T=221.0, F=0.140381/
&RAMP ID='FIRE_RAMP_MF', T=222.0, F=0.138647/
&RAMP ID='FIRE_RAMP_MF', T=223.0, F=0.140342/
&RAMP ID='FIRE_RAMP_MF', T=224.0, F=0.135996/
&RAMP ID='FIRE_RAMP_MF', T=225.0, F=0.129941/
&RAMP ID='FIRE_RAMP_MF', T=226.0, F=0.131641/
&RAMP ID='FIRE_RAMP_MF', T=227.0, F=0.129807/
&RAMP ID='FIRE_RAMP_MF', T=228.0, F=0.130629/
&RAMP ID='FIRE_RAMP_MF', T=229.0, F=0.128423/
&RAMP ID='FIRE_RAMP_MF', T=230.0, F=0.130002/
&RAMP ID='FIRE_RAMP_MF', T=231.0, F=0.131255/
&RAMP ID='FIRE_RAMP_MF', T=232.0, F=0.13034/
&RAMP ID='FIRE_RAMP_MF', T=233.0, F=0.130697/
&RAMP ID='FIRE_RAMP_MF', T=234.0, F=0.127809/
&RAMP ID='FIRE_RAMP_MF', T=235.0, F=0.125505/
&RAMP ID='FIRE_RAMP_MF', T=236.0, F=0.125721/
&RAMP ID='FIRE_RAMP_MF', T=237.0, F=0.123731/

∅

&RAMP ID='FIRE_RAMP_MF', T=238.0, F=0.12331/
&RAMP ID='FIRE_RAMP_MF', T=239.0, F=0.123515/
&RAMP ID='FIRE_RAMP_MF', T=240.0, F=0.123908/
&RAMP ID='FIRE_RAMP_MF', T=241.0, F=0.12461/
&RAMP ID='FIRE_RAMP_MF', T=242.0, F=0.124277/
&RAMP ID='FIRE_RAMP_MF', T=243.0, F=0.124208/
&RAMP ID='FIRE_RAMP_MF', T=244.0, F=0.123862/
&RAMP ID='FIRE_RAMP_MF', T=245.0, F=0.123263/
&RAMP ID='FIRE_RAMP_MF', T=246.0, F=0.120229/
&RAMP ID='FIRE_RAMP_MF', T=247.0, F=0.120412/
&RAMP ID='FIRE_RAMP_MF', T=248.0, F=0.118702/
&RAMP ID='FIRE_RAMP_MF', T=249.0, F=0.120536/
&RAMP ID='FIRE_RAMP_MF', T=250.0, F=0.120251/
&RAMP ID='FIRE_RAMP_MF', T=251.0, F=0.117116/
&RAMP ID='FIRE_RAMP_MF', T=252.0, F=0.115916/
&RAMP ID='FIRE_RAMP_MF', T=253.0, F=0.115612/
&RAMP ID='FIRE_RAMP_MF', T=254.0, F=0.11576/
&RAMP ID='FIRE_RAMP_MF', T=255.0, F=0.116434/
&RAMP ID='FIRE_RAMP_MF', T=256.0, F=0.116302/
&RAMP ID='FIRE_RAMP_MF', T=257.0, F=0.119531/
&RAMP ID='FIRE_RAMP_MF', T=258.0, F=0.119783/
&RAMP ID='FIRE_RAMP_MF', T=259.0, F=0.121878/
&RAMP ID='FIRE_RAMP_MF', T=260.0, F=0.118905/
&RAMP ID='FIRE_RAMP_MF', T=261.0, F=0.116878/
&RAMP ID='FIRE_RAMP_MF', T=262.0, F=0.120407/
&RAMP ID='FIRE_RAMP_MF', T=263.0, F=0.118378/
&RAMP ID='FIRE_RAMP_MF', T=264.0, F=0.117229/
&RAMP ID='FIRE_RAMP_MF', T=265.0, F=0.116229/
&RAMP ID='FIRE_RAMP_MF', T=266.0, F=0.117433/

&RAMP ID='FIRE_RAMP_MF', T=267.0, F=0.115036/
&RAMP ID='FIRE_RAMP_MF', T=268.0, F=0.114583/
&RAMP ID='FIRE_RAMP_MF', T=269.0, F=0.113026/
&RAMP ID='FIRE_RAMP_MF', T=270.0, F=0.111633/
&RAMP ID='FIRE_RAMP_MF', T=271.0, F=0.113209/
&RAMP ID='FIRE_RAMP_MF', T=272.0, F=0.110599/
&RAMP ID='FIRE_RAMP_MF', T=273.0, F=0.107202/
&RAMP ID='FIRE_RAMP_MF', T=274.0, F=0.106849/
&RAMP ID='FIRE_RAMP_MF', T=275.0, F=0.109788/
&RAMP ID='FIRE_RAMP_MF', T=276.0, F=0.111362/
&RAMP ID='FIRE_RAMP_MF', T=277.0, F=0.111239/
&RAMP ID='FIRE_RAMP_MF', T=278.0, F=0.107761/
&RAMP ID='FIRE_RAMP_MF', T=279.0, F=0.107813/
&RAMP ID='FIRE_RAMP_MF', T=280.0, F=0.106948/
&RAMP ID='FIRE_RAMP_MF', T=281.0, F=0.106933/
&RAMP ID='FIRE_RAMP_MF', T=282.0, F=0.109405/
&RAMP ID='FIRE_RAMP_MF', T=283.0, F=0.109065/
&RAMP ID='FIRE_RAMP_MF', T=284.0, F=0.107286/
&RAMP ID='FIRE_RAMP_MF', T=285.0, F=0.107311/
&RAMP ID='FIRE_RAMP_MF', T=286.0, F=0.106643/
&RAMP ID='FIRE_RAMP_MF', T=287.0, F=0.105447/
&RAMP ID='FIRE_RAMP_MF', T=288.0, F=0.106298/
&RAMP ID='FIRE_RAMP_MF', T=289.0, F=0.106298/
&RAMP ID='FIRE_RAMP_MF', T=290.0, F=0.101763/
&RAMP ID='FIRE_RAMP_MF', T=291.0, F=0.100536/
&RAMP ID='FIRE_RAMP_MF', T=292.0, F=0.100536/
&RAMP ID='FIRE_RAMP_MF', T=293.0, F=0.10275/
&RAMP ID='FIRE_RAMP_MF', T=294.0, F=0.104118/
&RAMP ID='FIRE_RAMP_MF', T=295.0, F=0.104118/

&RAMP ID='FIRE_RAMP_MF', T=296.0, F=0.102847/
&RAMP ID='FIRE_RAMP_MF', T=297.0, F=0.102406/
&RAMP ID='FIRE_RAMP_MF', T=298.0, F=0.102406/
&RAMP ID='FIRE_RAMP_MF', T=299.0, F=0.101879/
&RAMP ID='FIRE_RAMP_MF', T=300.0, F=0.10273/
&RAMP ID='FIRE_RAMP_MF', T=301.0, F=0.10273/
&RAMP ID='FIRE_RAMP_MF', T=302.0, F=0.101269/
&RAMP ID='FIRE_RAMP_MF', T=303.0, F=0.099884/
&RAMP ID='FIRE_RAMP_MF', T=304.0, F=0.099884/
&RAMP ID='FIRE_RAMP_MF', T=305.0, F=0.102925/
&RAMP ID='FIRE_RAMP_MF', T=306.0, F=0.102582/
&RAMP ID='FIRE_RAMP_MF', T=307.0, F=0.102582/
&RAMP ID='FIRE_RAMP_MF', T=308.0, F=0.100497/
&RAMP ID='FIRE_RAMP_MF', T=309.0, F=0.098354/
&RAMP ID='FIRE_RAMP_MF', T=310.0, F=0.099278/
&RAMP ID='FIRE_RAMP_MF', T=311.0, F=0.097263/
&RAMP ID='FIRE_RAMP_MF', T=312.0, F=0.095798/
&RAMP ID='FIRE_RAMP_MF', T=313.0, F=0.095896/
&RAMP ID='FIRE_RAMP_MF', T=314.0, F=0.095899/
&RAMP ID='FIRE_RAMP_MF', T=315.0, F=0.095517/
&RAMP ID='FIRE_RAMP_MF', T=316.0, F=0.095389/
&RAMP ID='FIRE_RAMP_MF', T=317.0, F=0.095063/
&RAMP ID='FIRE_RAMP_MF', T=318.0, F=0.0938/
&RAMP ID='FIRE_RAMP_MF', T=319.0, F=0.09305/
&RAMP ID='FIRE_RAMP_MF', T=320.0, F=0.092045/
&RAMP ID='FIRE_RAMP_MF', T=321.0, F=0.0921/
&RAMP ID='FIRE_RAMP_MF', T=322.0, F=0.093119/
&RAMP ID='FIRE_RAMP_MF', T=323.0, F=0.091416/
&RAMP ID='FIRE_RAMP_MF', T=324.0, F=0.09068/

&RAMP ID='FIRE_RAMP_MF', T=325.0, F=0.091841/
&RAMP ID='FIRE_RAMP_MF', T=326.0, F=0.088816/
&RAMP ID='FIRE_RAMP_MF', T=327.0, F=0.087545/
&RAMP ID='FIRE_RAMP_MF', T=328.0, F=0.087589/
&RAMP ID='FIRE_RAMP_MF', T=329.0, F=0.089399/
&RAMP ID='FIRE_RAMP_MF', T=330.0, F=0.08972/
&RAMP ID='FIRE_RAMP_MF', T=331.0, F=0.089/
&RAMP ID='FIRE_RAMP_MF', T=332.0, F=0.086785/
&RAMP ID='FIRE_RAMP_MF', T=333.0, F=0.084524/
&RAMP ID='FIRE_RAMP_MF', T=334.0, F=0.083331/
&RAMP ID='FIRE_RAMP_MF', T=335.0, F=0.082816/
&RAMP ID='FIRE_RAMP_MF', T=336.0, F=0.082592/
&RAMP ID='FIRE_RAMP_MF', T=337.0, F=0.081493/
&RAMP ID='FIRE_RAMP_MF', T=338.0, F=0.08408/
&RAMP ID='FIRE_RAMP_MF', T=339.0, F=0.084297/
&RAMP ID='FIRE_RAMP_MF', T=340.0, F=0.084519/
&RAMP ID='FIRE_RAMP_MF', T=341.0, F=0.083509/
&RAMP ID='FIRE_RAMP_MF', T=342.0, F=0.082459/
&RAMP ID='FIRE_RAMP_MF', T=343.0, F=0.082817/
&RAMP ID='FIRE_RAMP_MF', T=344.0, F=0.080376/
&RAMP ID='FIRE_RAMP_MF', T=345.0, F=0.082662/
&RAMP ID='FIRE_RAMP_MF', T=346.0, F=0.082135/
&RAMP ID='FIRE_RAMP_MF', T=347.0, F=0.082611/
&RAMP ID='FIRE_RAMP_MF', T=348.0, F=0.081279/
&RAMP ID='FIRE_RAMP_MF', T=349.0, F=0.081534/
&RAMP ID='FIRE_RAMP_MF', T=350.0, F=0.081255/
&RAMP ID='FIRE_RAMP_MF', T=351.0, F=0.081224/
&RAMP ID='FIRE_RAMP_MF', T=352.0, F=0.081054/
&RAMP ID='FIRE_RAMP_MF', T=353.0, F=0.079605/

&RAMP ID='FIRE_RAMP_MF', T=354.0, F=0.077655/
&RAMP ID='FIRE_RAMP_MF', T=355.0, F=0.07779/
&RAMP ID='FIRE_RAMP_MF', T=356.0, F=0.071873/
&RAMP ID='FIRE_RAMP_MF', T=357.0, F=0.071514/
&RAMP ID='FIRE_RAMP_MF', T=358.0, F=0.071267/
&RAMP ID='FIRE_RAMP_MF', T=359.0, F=0.070679/
&RAMP ID='FIRE_RAMP_MF', T=360.0, F=0.069639/
&RAMP ID='FIRE_RAMP_MF', T=361.0, F=0.069973/
&RAMP ID='FIRE_RAMP_MF', T=362.0, F=0.069331/
&RAMP ID='FIRE_RAMP_MF', T=363.0, F=0.069022/
&RAMP ID='FIRE_RAMP_MF', T=364.0, F=0.068546/
&RAMP ID='FIRE_RAMP_MF', T=365.0, F=0.068673/
&RAMP ID='FIRE_RAMP_MF', T=366.0, F=0.069834/
&RAMP ID='FIRE_RAMP_MF', T=367.0, F=0.069602/
&RAMP ID='FIRE_RAMP_MF', T=368.0, F=0.066948/
&RAMP ID='FIRE_RAMP_MF', T=369.0, F=0.066621/
&RAMP ID='FIRE_RAMP_MF', T=370.0, F=0.067722/
&RAMP ID='FIRE_RAMP_MF', T=371.0, F=0.065427/
&RAMP ID='FIRE_RAMP_MF', T=372.0, F=0.065833/
&RAMP ID='FIRE_RAMP_MF', T=373.0, F=0.065567/
&RAMP ID='FIRE_RAMP_MF', T=374.0, F=0.065544/
&RAMP ID='FIRE_RAMP_MF', T=375.0, F=0.062596/
&RAMP ID='FIRE_RAMP_MF', T=376.0, F=0.061681/
&RAMP ID='FIRE_RAMP_MF', T=377.0, F=0.063413/
&RAMP ID='FIRE_RAMP_MF', T=378.0, F=0.063429/
&RAMP ID='FIRE_RAMP_MF', T=379.0, F=0.063949/
&RAMP ID='FIRE_RAMP_MF', T=380.0, F=0.064236/
&RAMP ID='FIRE_RAMP_MF', T=381.0, F=0.062518/
&RAMP ID='FIRE_RAMP_MF', T=382.0, F=0.062489/

&RAMP ID='FIRE_RAMP_MF', T=383.0, F=0.06234/
&RAMP ID='FIRE_RAMP_MF', T=384.0, F=0.059457/
&RAMP ID='FIRE_RAMP_MF', T=385.0, F=0.059753/
&RAMP ID='FIRE_RAMP_MF', T=386.0, F=0.057009/
&RAMP ID='FIRE_RAMP_MF', T=387.0, F=0.058434/
&RAMP ID='FIRE_RAMP_MF', T=388.0, F=0.057055/
&RAMP ID='FIRE_RAMP_MF', T=389.0, F=0.055497/
&RAMP ID='FIRE_RAMP_MF', T=390.0, F=0.055846/
&RAMP ID='FIRE_RAMP_MF', T=391.0, F=0.055846/
&RAMP ID='FIRE_RAMP_MF', T=392.0, F=0.055172/
&RAMP ID='FIRE_RAMP_MF', T=393.0, F=0.055922/
&RAMP ID='FIRE_RAMP_MF', T=394.0, F=0.055922/
&RAMP ID='FIRE_RAMP_MF', T=395.0, F=0.056441/
&RAMP ID='FIRE_RAMP_MF', T=396.0, F=0.055886/
&RAMP ID='FIRE_RAMP_MF', T=397.0, F=0.055886/
&RAMP ID='FIRE_RAMP_MF', T=398.0, F=0.053829/
&RAMP ID='FIRE_RAMP_MF', T=399.0, F=0.053002/
&RAMP ID='FIRE_RAMP_MF', T=400.0, F=0.053002/
&RAMP ID='FIRE_RAMP_MF', T=401.0, F=0.051712/
&RAMP ID='FIRE_RAMP_MF', T=402.0, F=0.054054/
&RAMP ID='FIRE_RAMP_MF', T=403.0, F=0.054054/
&RAMP ID='FIRE_RAMP_MF', T=404.0, F=0.054287/
&RAMP ID='FIRE_RAMP_MF', T=405.0, F=0.053129/
&RAMP ID='FIRE_RAMP_MF', T=406.0, F=0.053129/
&RAMP ID='FIRE_RAMP_MF', T=407.0, F=0.052447/
&RAMP ID='FIRE_RAMP_MF', T=408.0, F=0.050208/
&RAMP ID='FIRE_RAMP_MF', T=409.0, F=0.050208/
&RAMP ID='FIRE_RAMP_MF', T=410.0, F=0.048479/
&RAMP ID='FIRE_RAMP_MF', T=411.0, F=0.048653/

&RAMP ID='FIRE_RAMP_MF', T=412.0, F=0.049319/
&RAMP ID='FIRE_RAMP_MF', T=413.0, F=0.047323/
&RAMP ID='FIRE_RAMP_MF', T=414.0, F=0.047237/
&RAMP ID='FIRE_RAMP_MF', T=415.0, F=0.047648/
&RAMP ID='FIRE_RAMP_MF', T=416.0, F=0.045429/
&RAMP ID='FIRE_RAMP_MF', T=417.0, F=0.045809/
&RAMP ID='FIRE_RAMP_MF', T=418.0, F=0.045811/
&RAMP ID='FIRE_RAMP_MF', T=419.0, F=0.046934/
&RAMP ID='FIRE_RAMP_MF', T=420.0, F=0.046679/
&RAMP ID='FIRE_RAMP_MF', T=421.0, F=0.046755/
&RAMP ID='FIRE_RAMP_MF', T=422.0, F=0.045613/
&RAMP ID='FIRE_RAMP_MF', T=423.0, F=0.045138/
&RAMP ID='FIRE_RAMP_MF', T=424.0, F=0.045161/
&RAMP ID='FIRE_RAMP_MF', T=425.0, F=0.043589/
&RAMP ID='FIRE_RAMP_MF', T=426.0, F=0.041703/
&RAMP ID='FIRE_RAMP_MF', T=427.0, F=0.042579/
&RAMP ID='FIRE_RAMP_MF', T=428.0, F=0.041312/
&RAMP ID='FIRE_RAMP_MF', T=429.0, F=0.039676/
&RAMP ID='FIRE_RAMP_MF', T=430.0, F=0.039613/
&RAMP ID='FIRE_RAMP_MF', T=431.0, F=0.040912/
&RAMP ID='FIRE_RAMP_MF', T=432.0, F=0.039729/
&RAMP ID='FIRE_RAMP_MF', T=433.0, F=0.039965/
&RAMP ID='FIRE_RAMP_MF', T=434.0, F=0.038594/
&RAMP ID='FIRE_RAMP_MF', T=435.0, F=0.040356/
&RAMP ID='FIRE_RAMP_MF', T=436.0, F=0.040772/
&RAMP ID='FIRE_RAMP_MF', T=437.0, F=0.041002/
&RAMP ID='FIRE_RAMP_MF', T=438.0, F=0.042159/
&RAMP ID='FIRE_RAMP_MF', T=439.0, F=0.041713/
&RAMP ID='FIRE_RAMP_MF', T=440.0, F=0.038248/

&RAMP ID='FIRE_RAMP_MF', T=441.0, F=0.03937/
&RAMP ID='FIRE_RAMP_MF', T=442.0, F=0.039443/
&RAMP ID='FIRE_RAMP_MF', T=443.0, F=0.037595/
&RAMP ID='FIRE_RAMP_MF', T=444.0, F=0.036353/
&RAMP ID='FIRE_RAMP_MF', T=445.0, F=0.036624/
&RAMP ID='FIRE_RAMP_MF', T=446.0, F=0.036668/
&RAMP ID='FIRE_RAMP_MF', T=447.0, F=0.036619/
&RAMP ID='FIRE_RAMP_MF', T=448.0, F=0.036462/
&RAMP ID='FIRE_RAMP_MF', T=449.0, F=0.036338/
&RAMP ID='FIRE_RAMP_MF', T=450.0, F=0.036723/
&RAMP ID='FIRE_RAMP_MF', T=451.0, F=0.036908/
&RAMP ID='FIRE_RAMP_MF', T=452.0, F=0.037231/
&RAMP ID='FIRE_RAMP_MF', T=453.0, F=0.036142/
&RAMP ID='FIRE_RAMP_MF', T=454.0, F=0.035975/
&RAMP ID='FIRE_RAMP_MF', T=455.0, F=0.034906/
&RAMP ID='FIRE_RAMP_MF', T=456.0, F=0.035463/
&RAMP ID='FIRE_RAMP_MF', T=457.0, F=0.034924/
&RAMP ID='FIRE_RAMP_MF', T=458.0, F=0.036285/
&RAMP ID='FIRE_RAMP_MF', T=459.0, F=0.036094/
&RAMP ID='FIRE_RAMP_MF', T=460.0, F=0.035842/
&RAMP ID='FIRE_RAMP_MF', T=461.0, F=0.035337/
&RAMP ID='FIRE_RAMP_MF', T=462.0, F=0.035281/
&RAMP ID='FIRE_RAMP_MF', T=463.0, F=0.035291/
&RAMP ID='FIRE_RAMP_MF', T=464.0, F=0.034237/
&RAMP ID='FIRE_RAMP_MF', T=465.0, F=0.033867/
&RAMP ID='FIRE_RAMP_MF', T=466.0, F=0.033988/
&RAMP ID='FIRE_RAMP_MF', T=467.0, F=0.034237/
&RAMP ID='FIRE_RAMP_MF', T=468.0, F=0.032875/
&RAMP ID='FIRE_RAMP_MF', T=469.0, F=0.032876/

&RAMP ID='FIRE_RAMP_MF', T=470.0, F=0.032094/
&RAMP ID='FIRE_RAMP_MF', T=471.0, F=0.030303/
&RAMP ID='FIRE_RAMP_MF', T=472.0, F=0.030224/
&RAMP ID='FIRE_RAMP_MF', T=473.0, F=0.032331/
&RAMP ID='FIRE_RAMP_MF', T=474.0, F=0.02947/
&RAMP ID='FIRE_RAMP_MF', T=475.0, F=0.029653/
&RAMP ID='FIRE_RAMP_MF', T=476.0, F=0.031343/
&RAMP ID='FIRE_RAMP_MF', T=477.0, F=0.030668/
&RAMP ID='FIRE_RAMP_MF', T=478.0, F=0.030231/
&RAMP ID='FIRE_RAMP_MF', T=479.0, F=0.031004/
&RAMP ID='FIRE_RAMP_MF', T=480.0, F=0.031192/
&RAMP ID='FIRE_RAMP_MF', T=481.0, F=0.031277/
&RAMP ID='FIRE_RAMP_MF', T=482.0, F=0.031543/
&RAMP ID='FIRE_RAMP_MF', T=483.0, F=0.028913/
&RAMP ID='FIRE_RAMP_MF', T=484.0, F=0.028991/
&RAMP ID='FIRE_RAMP_MF', T=485.0, F=0.029256/
&RAMP ID='FIRE_RAMP_MF', T=486.0, F=0.026905/
&RAMP ID='FIRE_RAMP_MF', T=487.0, F=0.027306/
&RAMP ID='FIRE_RAMP_MF', T=488.0, F=0.027276/
&RAMP ID='FIRE_RAMP_MF', T=489.0, F=0.027309/
&RAMP ID='FIRE_RAMP_MF', T=490.0, F=0.027539/
&RAMP ID='FIRE_RAMP_MF', T=491.0, F=0.028432/
&RAMP ID='FIRE_RAMP_MF', T=492.0, F=0.028543/
&RAMP ID='FIRE_RAMP_MF', T=493.0, F=0.028543/
&RAMP ID='FIRE_RAMP_MF', T=494.0, F=0.026758/
&RAMP ID='FIRE_RAMP_MF', T=495.0, F=0.026609/
&RAMP ID='FIRE_RAMP_MF', T=496.0, F=0.026609/
&RAMP ID='FIRE_RAMP_MF', T=497.0, F=0.026211/
&RAMP ID='FIRE_RAMP_MF', T=498.0, F=0.025051/

HH

```
&RAMP ID='FIRE_RAMP_MF', T=499.0, F=0.025051/  
&RAMP ID='FIRE_RAMP_MF', T=500.0, F=0.026205/  
&SURF ID='PV MODULE',  
  COLOR='GRAY 60',  
  TEXTURE_MAP='psm_metal.jpg',  
  TEXTURE_WIDTH=3.0,  
  TEXTURE_HEIGHT=2.0,  
  BACKING='VOID',  
  MATL_ID(1,1)='STEEL',  
  MATL_MASS_FRACTION(1,1)=1.0,  
  THICKNESS(1)=2.0E-3/  
&SURF ID='SPRUCE+ICOPAL_TOPSAFE',  
  RGB=146,202,166,  
  BACKING='VOID',  
  MATL_ID(1,1)='ICOPAL_TOPSAFE',  
  MATL_ID(2,1:2)='SPRUCE','WATER',  
  MATL_MASS_FRACTION(1,1)=1.0,  
  MATL_MASS_FRACTION(2,1:2)=0.91,0.09,  
  THICKNESS(1:2)=3.0E-3,0.022,  
  stretch_factor=1,  
  cell_size_factor=0.8/  
  
&OBST ID='FIRE', XB=0.04,0.14,2.05,2.15,0.025,0.045, SURF_ID='INERT'/  
&OBST ID='PARTICLE_BOARD+ROOFING', XB=0.0,0.18,1.9,2.0,5.0E-3,0.025,  
SURF_ID='SPRUCE+ICOPAL_TOPSAFE'/  
&OBST ID='PARTICLE_BOARD+ROOFING', XB=0.0,0.09,2.0,2.1,5.0E-3,0.025,  
SURF_ID='SPRUCE+ICOPAL_TOPSAFE'/  
&OBST ID='PARTICLE_BOARD+ROOFING', XB=0.09,0.18,2.0,2.1,5.0E-3,0.025,  
SURF_ID='SPRUCE+ICOPAL_TOPSAFE'/
```

&OBST ID='PARTICLE_BOARD+ROOFING', XB=0.0,0.09,2.1,2.2,5.0E-3,0.025,
SURF_ID='SPRUCE+ICOPAL_TOPSAFE'/

&OBST ID='PARTICLE_BOARD+ROOFING', XB=0.09,0.18,2.1,2.2,5.0E-3,0.025,
SURF_ID='SPRUCE+ICOPAL_TOPSAFE'/

&OBST ID='PARTICLE_BOARD+ROOFING', XB=0.0,0.18,2.2,2.3,5.0E-3,0.025,
SURF_ID='SPRUCE+ICOPAL_TOPSAFE'/

&OBST ID='PARTICLE_BOARD+ROOFING', XB=0.18,0.34,1.9,2.1,5.0E-3,0.025,
SURF_ID='SPRUCE+ICOPAL_TOPSAFE'/

&OBST ID='PARTICLE_BOARD+ROOFING', XB=0.18,0.34,2.1,2.3,5.0E-3,0.025,
SURF_ID='SPRUCE+ICOPAL_TOPSAFE'/

&OBST ID='PARTICLE_BOARD+ROOFING', XB=0.34,0.56,1.9,2.1,5.0E-3,0.025,
SURF_ID='SPRUCE+ICOPAL_TOPSAFE'/

&OBST ID='PARTICLE_BOARD+ROOFING', XB=0.34,0.56,2.1,2.3,5.0E-3,0.025,
SURF_ID='SPRUCE+ICOPAL_TOPSAFE'/

&OBST ID='PARTICLE_BOARD+ROOFING', XB=0.56,0.78,1.9,2.1,5.0E-3,0.025,
SURF_ID='SPRUCE+ICOPAL_TOPSAFE'/

&OBST ID='PARTICLE_BOARD+ROOFING', XB=0.56,0.78,2.1,2.3,5.0E-3,0.025,
SURF_ID='SPRUCE+ICOPAL_TOPSAFE'/

&OBST ID='PARTICLE_BOARD+ROOFING', XB=0.78,1.0,1.9,2.1,5.0E-3,0.025,
SURF_ID='SPRUCE+ICOPAL_TOPSAFE'/

&OBST ID='PARTICLE_BOARD+ROOFING', XB=0.78,1.0,2.1,2.3,5.0E-3,0.025,
SURF_ID='SPRUCE+ICOPAL_TOPSAFE'/

&OBST ID='PV MODULE', XB=0.15,0.18,1.92,2.0,0.085,0.095, SURF_ID='PV MODULE'/

&OBST ID='PV MODULE', XB=0.15,0.18,2.0,2.1,0.085,0.095, SURF_ID='PV MODULE'/

&OBST ID='PV MODULE', XB=0.15,0.18,2.1,2.2,0.085,0.095, SURF_ID='PV MODULE'/

&OBST ID='PV MODULE', XB=0.15,0.18,2.2,2.27,0.085,0.095, SURF_ID='PV MODULE'/

&OBST ID='PV MODULE', XB=0.18,0.34,1.92,2.1,0.085,0.095, SURF_ID='PV MODULE'/

&OBST ID='PV MODULE', XB=0.18,0.34,2.1,2.27,0.085,0.095, SURF_ID='PV MODULE'/

&OBST ID='PV MODULE', XB=0.34,0.56,1.92,2.1,0.085,0.095, SURF_ID='PV MODULE'/

&OBST ID='PV MODULE', XB=0.34,0.56,2.1,2.27,0.085,0.095, SURF_ID='PV MODULE'/

&OBST ID='PV MODULE', XB=0.56,0.78,1.92,2.1,0.085,0.095, SURF_ID='PV MODULE'/

&OBST ID='PV MODULE', XB=0.56,0.78,2.1,2.27,0.085,0.095, SURF_ID='PV MODULE'/

&OBST ID='PV MODULE', XB=0.78,1.0,1.92,2.1,0.085,0.095, SURF_ID='PV MODULE'/

&OBST ID='PV MODULE', XB=0.78,1.0,2.1,2.27,0.085,0.095, SURF_ID='PV MODULE'/

&VENT ID='Mesh Vent: MESH [XMAX]', SURF_ID='OPEN', XB=1.08,1.08,1.9,2.3,5.0E-3,0.125/

&VENT ID='Mesh Vent: MESH [XMIN]', SURF_ID='OPEN', XB=0.0,0.0,1.9,2.3,5.0E-3,0.125/

&VENT ID='Mesh Vent: MESH [YMAX]', SURF_ID='OPEN', XB=0.0,1.08,2.3,2.3,5.0E-3,0.125/

&VENT ID='Mesh Vent: MESH [YMIN]', SURF_ID='OPEN', XB=0.0,1.08,1.9,1.9,5.0E-3,0.125/

&VENT ID='Mesh Vent: MESH [ZMAX]', SURF_ID='OPEN', XB=0.0,1.08,1.9,2.3,0.125,0.125/

&VENT ID='Mesh Vent: MESH [ZMIN]', SURF_ID='OPEN', XB=0.0,1.08,1.9,2.3,5.0E-3,5.0E-3/

&VENT ID='FIRE', SURF_ID='FIRE', XB=0.04,0.14,2.05,2.15,0.045,0.045/

&SLCF QUANTITY='TEMPERATURE', ID='Slice05', PBY=2.1/

&SLCF QUANTITY='TEMPERATURE', ID='Slice08', PBZ=0.025/

&SLCF QUANTITY='TEMPERATURE', ID='Slice09', PBZ=0.087/

&SLCF QUANTITY='TEMPERATURE', ID='Slice11', PBZ=0.022/

&SLCF QUANTITY='TEMPERATURE', ID='Slice10', PBZ=5.0E-3/

&TAIL /